Many-body quantum teleportation via operator spreading in the traversable wormhole protocol

Thomas Schuster,[1,*] Bryce Kobrin,[1,2,*] Ping Gao,[3] Iris Cong,[4] Emil T. Khabiboulline,[4] Norbert M. Linke,[5] Mikhail D. Lukin,[4] Christopher Monroe,[5] Beni Yoshida,[6] and Norman Y. Yao[1,2]

[1] *Department of Physics, University of California, Berkeley, California 94720 USA*
[2] *Materials Sciences Division, Lawrence Berkeley National Laboratory, Berkeley, CA 94720, USA*
[3] *Center for Theoretical Physics, Massachusetts Institute of Technology, Cambridge, MA 02139, USA*
[4] *Department of Physics, Harvard University, Cambridge, Massachusetts 02138, USA*
[5] *Joint Quantum Institute and Department of Physics, University of Maryland, College Park, MD 20742 USA*
[6] *Perimeter Institute for Theoretical Physics, Waterloo, Ontario N2L 2Y5, Canada*

(Dated: February 2, 2021)

By leveraging shared entanglement between a pair of qubits, one can teleport a quantum state from one particle to another. Recent advances have uncovered an intrinsically *many-body* generalization of quantum teleportation, with an elegant and surprising connection to gravity. In particular, the teleportation of quantum information relies on many-body dynamics, which originate from strongly-interacting systems that are holographically dual to gravity; from the gravitational perspective, such quantum teleportation can be understood as the transmission of information through a traversable wormhole. Here, we propose and analyze a new mechanism for many-body quantum teleportation—dubbed peaked-size teleportation. Intriguingly, peaked-size teleportation utilizes precisely the same type of quantum circuit as traversable wormhole teleportation, yet has a completely distinct microscopic origin: it relies upon the spreading of local operators under generic thermalizing dynamics and not gravitational physics. We demonstrate the ubiquity of peaked-size teleportation, both analytically and numerically, across a diverse landscape of physical systems, including random unitary circuits, the Sachdev-Ye-Kitaev model (at high temperatures), one-dimensional spin chains and a bulk theory of gravity with stringy corrections. Our results pave the way towards using many-body quantum teleportation as a powerful experimental tool for: (*i*) characterizing the size distributions of operators in strongly-correlated systems and (*ii*) distinguishing between generic and intrinsically gravitational scrambling dynamics. To this end, we provide a detailed experimental blueprint for realizing many-body quantum teleportation in both trapped ions and Rydberg atom arrays; effects of decoherence and experimental imperfections are analyzed.

Quantum teleportation leverages entanglement to transmit quantum information between distant locations [2–6]. Typically, one thinks about teleportation in the context of a few, well-controlled degrees of freedom. For example, two distant observers might share a pair of maximally entangled qubits (i.e. an EPR pair), enabling a measurement by one observer to teleport an unknown quantum state to the other.

Recently, a confluence of seminal results has unveiled several novel instances of teleportation in strongly-interacting, *many-body* systems [1, 7–16]. Similar to conventional quantum teleportation, these protocols utilize shared entanglement as well as measurement and classical communication. However, they differ from conventional quantum teleportation in a few key aspects. Most notably, prior to teleportation, the initial quantum state is *scrambled* by the application of a many-body unitary. At first glance, this coexistence of scrambling—broadly speaking, the increasing complexity of initially simple quantum information under many-body time dynamics [17–21]—and teleportation might seem counter-intuitive. Indeed, one often thinks of teleportation as a directed quantum channel moving information between two specific locations; in contrast, scrambling disperses quantum information across all of the degrees of freedom in a system. The most natural way to reconcile these two perspectives is through the language of quantum error correction [22]: by encoding, via scrambling, one observer's local information into non-local correlations across a many-body system, one can in fact teleport this information with access only to any few of the system's qubits.

The most notable example of many-body teleportation is the so-called traversable wormhole (TW) protocol, discovered in the context of quantum gravity [1, 7, 8, 14–16]. From the bulk gravitational perspective, this protocol consists of a particle traveling from one side of a wormhole geometry to the other; the wormhole is rendered traversable by the application of a two-sided boundary coupling. In the boundary theory, the wormhole geometry corresponds to a highly entangled thermofield double (TFD) state shared between two copies of a many-body system, and the coupling is implemented via measurement and feed-forward operations [Fig. 1(a)]. Crucially, for this bulk-boundary correspondence to hold, the Hamiltonian describing the boundary system must exhibit "coherent", gravitational scrambling dynamics—this is realized, for example, in the Sachdev-Ye-Kitaev (SYK)

* These authors contributed equally to this work.

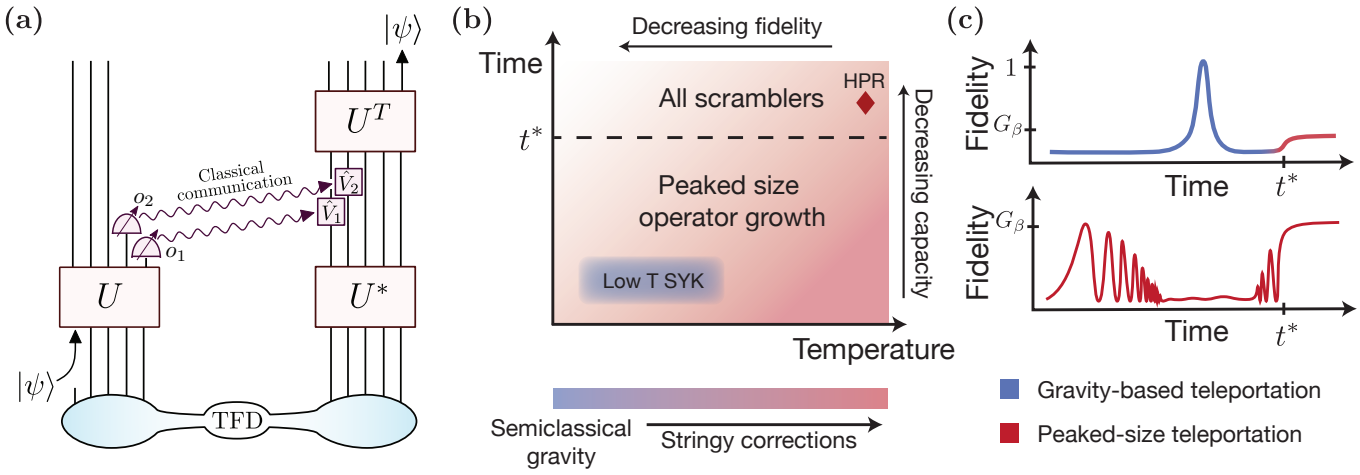

Figure 1. **(a)** Teleportation protocol, proceeding from bottom to top. To teleport, a subset of the left qubits are measured in the $\hat{O}_i$ basis, and operations $\hat{V}_i = e^{igo_i\hat{O}_i/K}$ conditioned on the measurement results o_i are performed on the right (purple). **(b)** The protocol hosts two mechanisms of teleportation: peaked-size (red) and gravitational (blue). The channel capacity of peaked-size teleportation decreases with increasing time, while its fidelity decreases with decreasing temperature. At high temperature and late times, it is equivalent to teleportation in the HPR protocol (red diamond). Gravitational teleportation occurs at low temperatures in systems dual to semiclassical gravity (e.g. the SYK model), and exhibits the same channel capacity but *higher* fidelity compared to peaked-size teleportation. Increasing the strength of stringy corrections to the gravity theory interpolates between gravitational and peaked-size teleportation. **(c)** The two mechanisms display distinct time profiles for the teleportation fidelity. In systems dual to gravity (top), the fidelity features a single $\mathcal{O}(1)$ peak near the scrambling time (gravitational, blue), and a late time revival (peaked-size, red) to a fidelity suppressed by the two-point function G_β [1]. In generic thermalizing systems (bottom), the fidelity oscillates between 0 and G_β with phase proportional to the operator size, may subsequently decay if sizes become not peaked, and revives at late times.

model at low temperatures.

Interestingly, recent work has uncovered a number of instances of many-body teleportation *without* gravitational dynamics. For example, teleportation in the TW protocol was recently demonstrated analytically in the SYK model at *high* temperatures [16], and numerically in chaotic spin chains at late times [14, 15]; in both cases, the microscopic mechanism for teleportation remains an outstanding puzzle. In addition to the TW protocol, an alternate many-body teleportation protocol was introduced in the context of the Hayden-Preskill variant of the black hole information paradox [10, 22]. This so-called Hayden-Preskill recovery (HPR) protocol allows for many-body teleportation via *generic* scrambling dynamics. Although the two protocols bear some structural similarity, the HPR protocol is exponentially less efficient for teleporting multiple qubits. To this end, understanding the precise relationship between these protocols remains an essential open question.

I. SUMMARY OF RESULTS

Here, we provide a framework that unifies all known examples of many-body teleportation outside the gravitational regime. The microscopic mechanism underlying this framework relies upon the growth of operators under scrambling time evolution. For the purposes of teleportation, this growth is naturally characterized by the size distribution of the operators [23–25], which provides a finer-grained measure of quantum information scrambling compared to more conventional quantities such as out-of-time-ordered correlators (OTOCs) [18, 20, 26]. Our teleportation mechanism—dubbed *peaked-size teleportation*—occurs in the TW protocol when the size distributions of operators are tightly peaked, a situation that arises for a wide variety of many-body dynamics.

Our results demonstrate that generic many-body dynamics can function as a powerful encoding procedure for the communication of quantum information. In particular, peaked-size teleportation represents an entanglement-assisted decoding scheme that is both exponentially more efficient than the HPR protocol, and applicable to a vastly broader class of encoding dynamics compared to gravitational teleportation [27, 28]. Furthermore, our work paves the way toward utilizing the TW protocol as a robust experimental tool for characterizing the growth of operators in strongly interacting systems, and as a litmus test for identifying intrinsically gravitational scrambling dynamics.

Analyzing the teleportation circuit (Section II)—To set the scene for peaked-size teleportation, we first determine the conditions for information recovery in the TW protocol [Fig. 1(a)]. In this protocol, locally encoded quantum information is inserted into one side of an entangled thermofield double (TFD) state and teleported to the other side through a combination of (*i*) unitary evolution of each side individually, and (*ii*) a simple two-sided cou-

pling that acts on a large subsystem of each side. The coupling is quite flexible in form, and corresponds to evolution, e^{igV}, under the two-sided interaction

$$V = \frac{1}{K}\sum_{i=1}^{K} O_{i,l}O^*_{i,r} \tag{1}$$

where O_i are *any* generic local operators applied to the left (l) and right (r) side of the system. This coupling can be performed either as a quantum gate, or through local measurements of O_i on the left side, followed by classical communication and feed-forward operations on the right side [Fig. 1(a)].

We begin by rigorously connecting the quantum teleportation fidelity to two-sided correlation functions of the form [1]:

$$C_Q(t) \equiv \langle \mathrm{TFD}|\, Q_r(-t)e^{igV}Q_l(t)\,|\mathrm{TFD}\rangle \tag{2}$$

where $Q(\pm t)$ is a time-evolved operator initially acting on the qubit(s) to be teleported. We isolate two conditions on these correlators that, when combined together, are necessary and sufficient for teleportation to succeed:

1. The magnitudes of the correlators must be maximal for every Q.

2. The phases of the correlators must be the same for every Q.

The first of these conditions is naturally satisfied if the TFD state is at infinite temperature, in which case it reduces to an extensive set of maximally entangled EPR pairs. On the other hand, meeting the second condition requires that the coupling acts non-trivially on the operators Q.

Relation to operator spreading (Section III)—A central theme of our work is relating the correlation functions, by virtue of the coupling V, to the size distribution of the time-evolved operator $Q(t)$. Specifically, writing $Q(t)$ as a sum over Pauli strings, $Q(t) = \sum_R c_R R$, we may define the the size distribution of $Q(t)$ as

$$P(\mathcal{S}) = \sum_{\mathcal{S}[R]=\mathcal{S}} |c_R|^2 \tag{3}$$

where the sum is over Pauli strings, R, of size $\mathcal{S}$. Crucially, the coupling V, by probing correlations between the two sides of the doubled Hilbert space, directly measures the operator size [24].

Peaked-size quantum teleportation (Section IV, V, VI)—The peaked-size teleportation mechanism succeeds whenever the size distributions of time-evolved operators, $Q(t)$, are tightly peaked about their average size. In this case, the exponentiated coupling, e^{igV}, applies approximately the same phase, proportional to the size, to each coefficient c_R, and therefore to the entire operator, $Q(t)$. We show that these applied phases can be used to align the phases of all correlators C_Q, achieving our second requirement for successful teleportation.

Interestingly, we find that peaked-size teleportation is naturally implemented across a broad landscape of interacting, many-body dynamics. To this end, we find it helpful to distinguish two broad regimes of dynamics: those at late times (after the scrambling time) and intermediate times (before the scrambling time). At late times, peaked-size teleportation occurs because operators become fully delocalized across the system, thus their size distribution is peaked about a typical, extensive value. In this regime, as in the HPR protocol, peaked-size teleportation is limited to transmitting only a single qubit. Motivated by this observation, we demonstrate a surprising relation between the HPR and TW protocols—despite their disparate origins, a simple modification of the coupling in the TW protocol renders it *identical* to the HPR protocol in the high temperature limit.

At intermediate times, peaked-size teleportation exhibits substantially richer behavior. We show that generic systems in $\geq$1D naturally satisfy the peaked-size condition due to thermalization within the bulk of a time-evolved operator's light cone. In contrast, the size distributions of operators in 0D, or all-to-all coupled, systems are not intrinsically peaked; however, they can be sufficiently narrowed by encoding the quantum information before insertion into the teleportation circuit. Interestingly, this resolves a previous puzzle, namely, the observation of teleportation in the Sachdev-Ye-Kitaev (SYK) model [29–32] *outside* the gravitational regime [16]. We substantiate these claims through extensive numerical and analytic studies in a variety of physical models: random unitary circuits (RUCs) in dimensions $d = 0, 1$, and 2 [33], the SYK model, and experimentally relevant spin chain Hamiltonians [34]. These studies explicitly demonstrate how the profile of operator size distributions in strongly-interacting systems controls the success and failure of many-body teleportation.

Through these examples, we investigate the capabilities of peaked-size teleportation as a quantum channel. In particular, we focus on two features—the channel capacity and the teleportation fidelity—as a function of evolution time and temperature [Fig. 1(b)]. Before the scrambling time, peaked-size teleportation is capable of sending multiple qubits with no increase in complexity; strikingly, it does so with the *same* asymptotic channel capacity as gravitational teleportation. This represents an exponential improvement in efficiency over previous instances of non-gravitational teleportation, i.e. in the HPR protocol [10]. Nevertheless, the fidelity of peaked-size teleportation is limited at low temperatures compared to gravity. This limit arises from the reduced entanglement of the TFD state (at low temperatures), and is naturally overcome by the unique structure of gravitational scrambling [1, 7, 14, 15].

Experimental implementations and implications (Section VIII)—Following this logic, we demonstrate that many-body quantum teleportation functions as a powerful diagnostic tool for scrambling dynamics in near-term quantum simulators, enabling one to distinguish

	Peaked-size, late times	Peaked-size, intermediate times	Gravitational, intermediate times
Physical setting	all thermalizing systems	generic thermalizing systems, e.g. spin chains, 0D RUCs, high-T SYK	systems with a semiclassical gravity dual (e.g. low-T SYK)
Teleportation time	$t \gtrsim t_s$	$t \lesssim t_s$	$t \lesssim t_s$
Channel capacity	1 qubit	$\sim K$ qubits	$\sim K$ qubits
Fidelity per qubit	$\sim G_\beta$	$\sim G_\beta$	~ 1
Coupling strength	$g \sim \pi \bmod 2\pi$	$g \sim \pi N/\mathcal{S} \bmod 2\pi$	$g \sim e^{-t}/G_N$

Table I. Comparison of peaked-size teleportation at intermediate and late times with gravitational teleportation. The three regimes differ in their teleportation fidelity, channel capacity, and the coupling strength g, which optimizes teleportation. Both peaked-size and gravitational teleportation exhibit a regime before the scrambling time t_s, where multiple qubits can be teleported.

between generic thermalizing systems and gravitational dynamics. To this end, we provide detailed blueprints for realizing the protocol in two complementary experimental platforms—Rydberg atom arrays [34–39] and trapped ions [40–44]. Specifically, the observation of a high teleportation fidelity at low temperatures in an experimental setting would be a tantalizing indicator of gravitational scrambling dynamics. In addition, gravitational dynamics exhibit unique qualitative features as a function of both evolution time and protocol parameters [Fig. 1(c), Table I]. More broadly, our analysis suggests that the TW protocol can also provide insights into many-body dynamics outside the gravitational regime. In particular, we demonstrate that the fidelity of peaked-size teleportation serves as an efficient probe of higher moments of operator size distributions [25].

Quantum gravity interpretation of peaked-size teleportation (Section VII)—Finally, while we have thus far indicated a sharp distinction between models with gravitational duals and generic thermalizing systems, this is not always the case. In particular, our results show that varying the temperature of the SYK model provides a continuous interpolation between gravitational teleportation at low temperature and peaked-size teleportation at high temperature. In the dual picture, perturbing away from the low temperature limit corresponds to adding *stringy* corrections to the gravity theory [31, 45, 46]. Following this intuition, we show that teleportation in a gravity theory with strong stringy corrections [1] bears a remarkable qualitative similarity to peaked-size teleportation, thus providing a first step towards a bulk understanding of this phenomenon.

II. ANALYZING THE TELEPORTATION PROTOCOL

To begin, let us describe the teleportation circuit depicted in Fig. 1(a) and redrawn below in greater detail:

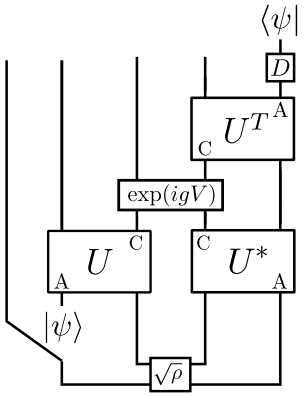

(4)

The protocol begins by preparing two copies of the system in an entangled TFD state. At infinite temperature, the TFD state is simply an extensive set of EPR pairs between the left and right systems:

$$|\mathrm{EPR}\rangle = \frac{1}{\sqrt{d}} \sum_{i=1}^{d} |i\rangle_l |i\rangle_r^* \equiv$$

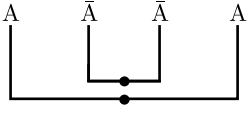

(5)

where we have decomposed each system into two subsystems, A and Ā, for future reference, and each dot represents a normalization factor given by the inverse square root of the subsystem's dimension. The finite temperature TFD state is obtained by applying the square root

of the density matrix to either side of $|\text{EPR}\rangle$:

$$|\text{TFD}\rangle = \rho_l^{1/2}\sqrt{d}\,|\text{EPR}\rangle = \rho_r^{*1/2}\sqrt{d}\,|\text{EPR}\rangle$$

$$\equiv \tag{6}$$

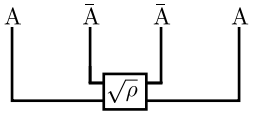

where $\rho^{1/2} \equiv e^{-\beta H/2}/\operatorname{tr}\left(e^{-\beta H}\right)^{1/2}$, and $\beta = 1/T$ is the inverse temperature.

The remainder of the protocol proceeds as described in Section I and depicted in Eq. (4). As shown in the latter, we denote the teleported qubit(s) as subsystem A and the coupled qubits as subsystem C (chosen independently from A). In addition, we include a simple decoding operator, D, applied at the end of the circuit before state recovery.

A. Requirements for successful teleportation

We now introduce heuristic arguments for when teleportation succeeds in this protocol. This will culminate in the two requirements for teleportation listed in Section I. In Section IV, we derive these conditions more formally by providing exact relations between the two-sided correlators in Eq. (2) and the teleportation fidelity.

To begin, let us first recall that a fundamental property of the EPR state is that an operator acting on the left side is equivalent to its transpose acting on the right:

$$O_l\,|\text{EPR}\rangle =$$

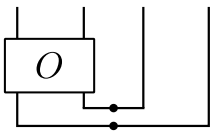

$$= \tag{7}$$

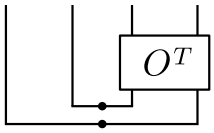

$$= O_r^T\,|\text{EPR}\rangle$$

While this property does not generally apply to the TFD state at finite temperature, it does hold for the unitary $U = e^{-iHt}$ since this commutes with the density matrix. Using this, we can re-express the teleportation circuit as:

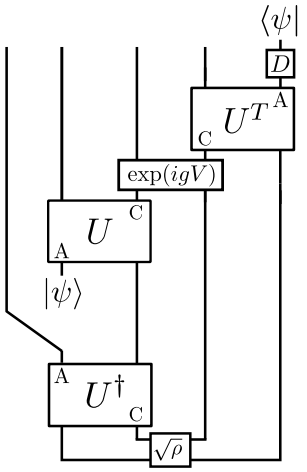

(8)

Next, since teleportation should occur regardless of the state of the swapped out subsystem, we can imagine measuring this leg to be in some state $|\phi\rangle$[1]:

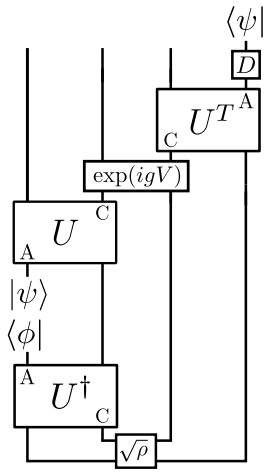

(9)

This reformulation makes it clear that teleportation depends on the action of the coupling on states of the form $Q_{A,l}(t)\,|\text{TFD}\rangle$, where $Q_A = |\psi\rangle\langle\phi|$ and we denote[2] time-evolved operators as $Q_A(t) \equiv UQ_AU^\dagger$.

The following identity, if true for all operators Q_A on

[1] At infinite temperature, using Eq. (7), $|\phi\rangle$ can be understood as the counterpart of $|\psi\rangle$, to be teleported from right to left instead of left to right.

[2] Traditionally, this would be considered reverse time-evolution, and denoted $Q_A(-t)$. For brevity, we have flipped the sign of t throughout the text.

A, would guarantee successful teleportation for all states:

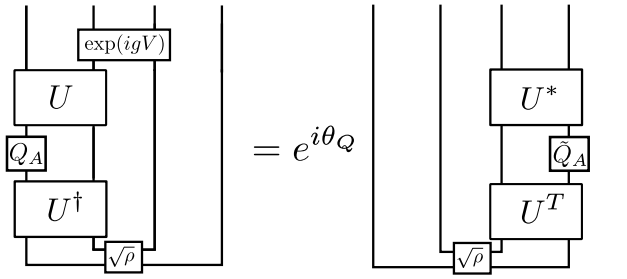

(10)

Here θ_Q is an overall phase and we represent conjugation by the decoding operator as $\tilde{Q}_A \equiv D^\dagger Q_A D$. One can verify this explicitly by plugging the RHS of the above equality into Eq. (9).

To quantify whether this equality holds, we should measure the inner product between the two states. This inner product[3],

$$C_Q = \langle \mathrm{TFD}| \tilde{Q}^\dagger_{A,r}(-t) e^{igV} Q_{A,l}(t) |\mathrm{TFD}\rangle$$

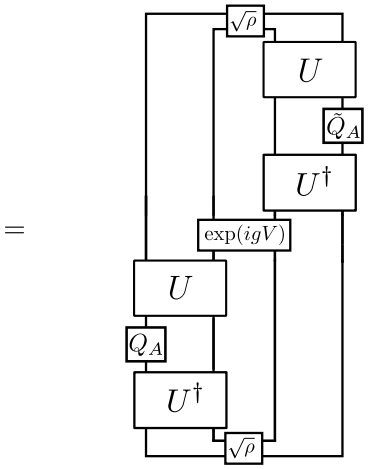

(11)

is precisely the two-sided correlation function introduced in Eq. (2), now modified to include the decoding operator. In particular, if the inner product is maximal for any operator Q_A, then Eq. (10) always holds and teleportation succeeds with perfect fidelity for all initial states.

In practice, it is sufficient to evaluate the correlators for a complete basis of operators on subsystem A (e.g. the Pauli operators). In this case, we now have *two* requirements on the operator correlators, as listed in Section I: (*i*) all correlators must have maximal magnitude, i.e. equal to 1, and (*ii*) all correlators must have the *same phase*—if two operators both individually obey Eq. (10) but with different phases, their sum will not.

At infinite temperature, owing to Eq. (7), the first requirement is satisfied even in the absence of the coupling, for any symmetric or antisymmetric operator. However, to satisfy the second requirement, the role of the coupling e^{igV} must be to apply a Q_A-dependent overall phase. In the following Section, we analyze the action of the coupling and show precisely when such an overall phase occurs.

[3]For simplicity of notation and consistency with previous works [1, 7, 16], from here on we have assumed that the unitary is symmetric, $U^T = U$, $U^\dagger = U^*$.

III. CONNECTION TO OPERATOR SIZE

In this Section, we outline the connection between the coupling V and the operator size when V is acted on states of the form:

$$Q_{A,l}(t) |\mathrm{TFD}\rangle = Q_{A,l}(t) \rho_l^{1/2} |\mathrm{EPR}\rangle . \tag{12}$$

This connection has been noted in a number of previous works, focusing primarily on a specific bilinear coupling in fermionic systems [14, 15, 23, 24, 47–49]. In the following, we extend this notion to bosonic systems and more generic couplings. We then show that the action of the exponentiated coupling, e^{igV}, is particularly simple—it applies an overall phase—whenever operator size distributions are tightly peaked.

A. Coupling measures size

In bosonic qudit systems, we define the size of a Pauli string as its number of non-identity elements. For instance, the Pauli string

$$\mathbb{1} \otimes X \otimes \mathbb{1} \otimes \mathbb{1} \otimes Z \otimes X \otimes \mathbb{1} \tag{13}$$

has size 3. A more general operator can be written as a sum of Pauli strings, R:

$$Q_A(t)\rho^{1/2} = \sum_R c_R(t) R, \tag{14}$$

and possesses a corresponding *size distribution*. We define this distribution, $P(\mathcal{S})$, as

$$P(\mathcal{S}) = \sum_{\mathcal{S}[R]=\mathcal{S}} |c_R(t)|^2. \tag{15}$$

The distribution is normalized,

$$\sum_{\mathcal{S}} P(\mathcal{S}) = \sum_R |c_R(t)|^2 = \mathrm{tr}(\rho) = 1. \tag{16}$$

We note that, at finite temperature, the coefficients $c_R(t)$ will generally be complex. The role of their phases is discussed in Section VII.

The operator size is naturally measured in the doubled Hilbert space associated with the state in Eq. (12). In bosonic qudit systems, the *exact* measure of the operator size is a sum of individual EPR projectors on each qudit i:

$$V_s = \frac{1}{N}\sum_{i=1}^N P_{\mathrm{EPR},i} = \frac{1}{Nd^2}\sum_{i=1}^N \sum_{P_i} P_{i,l} P^*_{i,r}, \tag{17}$$

where d is the local qudit dimension, N is the number of qudits, and P_i form a complete basis of single-qudit operators (e.g. for qubits $P_i \in \{\mathbb{1}, X, Y, Z\}$). This coupling is clearly of the form used in the teleportation protocol [Eq. (1)]. Its eigenstates are $R_l \left|\text{EPR}\right\rangle$ for Pauli strings R, with eigenvalues determined by the size, $\mathcal{S}[R]$, of the Pauli string:

$$V_s R_l \left|\text{EPR}\right\rangle = \left(1 - \frac{\mathcal{S}[R]}{N}\right) R_l \left|\text{EPR}\right\rangle . \tag{18}$$

Acting on a general time-evolved operator, we have

$$V_s Q_{A,l}(t) \left|\text{TFD}\right\rangle = d^{N/2} \sum_R \left(1 - \frac{\mathcal{S}[R]}{N}\right) c_R(t) R_l \left|\text{EPR}\right\rangle . \tag{19}$$

The expectation value of V in the state $Q_{A,l}(t) \left|\text{TFD}\right\rangle$ therefore measures the *average* of the size distribution, which we denote as $\mathcal{S}[Q_A \rho^{1/2}]$, or, when the context is clear, simply $\mathcal{S}$.

We can derive Eq. (18) by first analyzing the action of a single EPR projector, $P_{\text{EPR},i}$. Writing each Pauli string as a tensor product of single-qudit Paulis, $R = \bigotimes_{j=1}^N R_j$, we find

$$P_{\text{EPR},i} R_l \left|\text{EPR}\right\rangle = \delta_{R_i,\mathbb{1}} R_l \left|\text{EPR}\right\rangle , \tag{20}$$

since $\left\langle \text{EPR}_i \right| R_{i,l} \left|\text{EPR}_i\right\rangle = \text{tr}_i(R_i)/d_i = \delta_{R_i,\mathbb{1}}$. A single EPR projector thus acts as a binary variable, giving eigenvalue 1 or 0 if a given Pauli string is, or is not, the identity on the designated qudit. The full coupling is a sum of these binary variables over all qudits, and therefore counts the total number of non-identity elements in the Pauli string, i.e. the operator size.

We now turn to more general couplings of the form in Eq. (1). First, as a trivial but useful modification, we can remove the identity operators from V_s. These constitute a fraction $1/d^2$ of the complete basis, P_i, summed in Eq. (17). Removing these terms simply renormalizes the eigenvalues of the coupling:

$$\begin{aligned} &\left(\frac{1}{N(d^2-1)} \sum_{i=1}^N \sum_{P_i \neq \mathbb{1}} P_{i,l} P_{i,r}^*\right) R_l \left|\text{EPR}\right\rangle \\ &\qquad = \left[1 - \left(\frac{1}{1-1/d^2}\right) \frac{\mathcal{S}[R]}{N}\right] R_l \left|\text{EPR}\right\rangle , \end{aligned} \tag{21}$$

where the left side sum is now over $N(d^2-1)$ non-identity operators.

Second, we consider omitting some of the operators non-identity P_i at each site. Intuitively, under thermalizing dynamics, if an operator has spread to some qudit i it should not matter which Pauli operator we use to probe the operator's presence. For example, in qubits, a typical Pauli string of $Q_A(t)\rho^{1/2}$ will have equal probability to commute with Z_i as it would with X_i and Y_i; thus, coupling only using Z_i operators is sufficient for measuring a thermalized operator's size.

Third, we expect even more general couplings, composed of O_i that are local but not necessarily Pauli operators, to behave similarly. Specifically, each individual coupling, $O_{i,l} O_{i,r}$, will asymptote to two different expectation values before and after the time-evolved operator has spread to the support of O_i. Before, the coupling will maintain its expectation value in the unperturbed TFD state, $\text{tr}(O_i \rho^{1/2} O_i^\dagger \rho^{1/2})$. After, the spread of $Q_A(t)$ will disrupt the two-sided correlations in the TFD state that give rise to this initial expectation value, and the coupling will instead asymptote to its value in two thermal states, $\text{tr}(O_i \rho) \cdot \text{tr}(O_i \rho)$. As before, the sum of many terms, each behaving as above, leads to an approximate measure of operator size.

Lastly, we consider the case where the coupling is restricted to act only on some subsystem C, consisting of K qudits[4]. The coupling now measures the number of non-identity elements of a Pauli string within C—we denote this as the *K-size*, $\mathcal{S}_K$, of the Pauli string. The eigenvalues the coupling are the same as those in Eq. (21), with the replacement $\mathcal{S}/N \to \mathcal{S}_K/K$. For a typical Pauli operator, we expect the K-size distribution of an operator to be similar to its full size distribution when K is large and the coupled qubits are distributed randomly. In particular, we expect the average K-size, $\mathcal{S}_K$, to be proportional to the average size, $\mathcal{S}$,

$$\frac{\mathcal{S}_K}{K} \approx \frac{\mathcal{S}}{N} . \tag{22}$$

For simplicity, we will make this substitution, when appropriate, in the remainder of the work. However, if C is a spatially local subsystem (instead of a random subsystem), then this replacement will be modified depending on the spatial extent of the operator.

As a final remark, we note that the operator size distribution is directly related to out-of-time-order correlators (OTOCs), a more familiar quantity for probing operator growth [18, 20, 24, 26]. In particular, the average size is equal to a sum of OTOCs between Q_A and O_i [23, 24],

$$\begin{aligned} \text{OTOC}_1 &= \langle V \rangle_Q \equiv \left\langle \text{TFD} \right| Q_{A,l}^\dagger(t)\, V\, Q_{A,l}(t) \left|\text{TFD}\right\rangle \\ &= \frac{1}{K} \sum_{i=1}^K \\ &= \frac{1}{K} \sum_{i=1}^K \text{tr}\Big(\rho^{1/2}\, Q_A(t)\, O_i\, Q_A^\dagger(t)\, \rho^{1/2}\, O_i^\dagger\Big) \end{aligned} \tag{23}$$

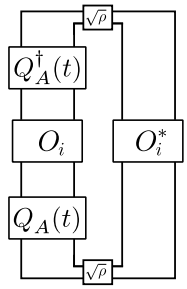

[4] For simplicity, this assumes that there is a single coupling per qudit in C.

To see this, one simply slides O_i^* and each $\sqrt{\rho}$ to the left side, and uses the fact that $\langle \text{EPR}| A_l |\text{EPR}\rangle = \text{tr}(A)/d^N$. Higher moments of the size distribution can also be probed by OTOCs, now between Q_A and various products of the O_i, e.g. O_iO_j for the size width. We discuss these relations further, paying particular to subtleties that arise at finite temperature, in Section VII.

B. Peaked-size distributions

We now turn to the action of the exponentiated coupling, e^{igV}. This applies a phase to each Pauli string of $Q_A(t)\rho^{1/2}$ determined by the string's size.

A particularly simple situation occurs when the operator's size distribution is *tightly peaked* about its average size. In this regime, each Pauli string gains approximately the same phase, and so the action of the coupling reduces to applying a Q_A-dependent overall phase,

$$e^{igV} Q_{A,l}(t) |\text{TFD}\rangle \approx e^{ig\langle V\rangle_Q} Q_{A,l}(t) |\text{TFD}\rangle , \tag{24}$$

where the applied phase is proportional to the average K-size [see Eq. (21)],

$$\begin{aligned} g\langle V\rangle_Q &= g \langle \text{TFD}| Q_{A,l}^\dagger(t) V Q_{A,l}(t) |\text{TFD}\rangle \\ &\approx g - g_d \frac{\mathcal{S}_K[Q_A(t)\rho^{1/2}]}{K}, \end{aligned} \tag{25}$$

and we define $g_d \equiv g/(1-1/d^2)$ for convenience.

Corrections to this behavior are controlled by higher moments of the size distribution. In particular, the leading order correction is equal to the K-size variance, $\delta S_K^2/K^2 = \langle V^2\rangle_Q - \langle V\rangle_Q^2$, multiplied by g^2:

$$\begin{aligned} \langle e^{igV}\rangle_Q &= \left\langle 1 + igV - \frac{1}{2}g^2V^2 + \dots \right\rangle_Q \\ &= \left(1 + ig\langle V\rangle_Q - \frac{1}{2}g^2\langle V\rangle_Q^2 + \dots\right) \\ &\quad - \frac{1}{2}g^2\left(\langle V^2\rangle_Q - \langle V\rangle_Q^2\right) + \dots \\ &= \exp\left(ig\langle V\rangle_Q\right) - \frac{1}{2}g^2\delta\mathcal{S}_K^2/K^2 + \dots \end{aligned} \tag{26}$$

The K-size variance receives contributions from two sources: the variance of the full size distribution, $\delta\mathcal{S}^2$, and a statistical error from sampling only K of N qubits for the K-size. If the K qubits are distributed randomly, these errors scale as $\delta\mathcal{S}_K \sim \delta\mathcal{S}\cdot(K/N)$ and $\delta\mathcal{S}_K \sim \sqrt{\mathcal{S}_K} \approx \sqrt{\mathcal{S}K/N}$, respectively (see Appendix E for a detailed derivation of the latter). These are small compared to the average K-size whenever $\delta\mathcal{S} \ll \mathcal{S}$ and $1 \ll \mathcal{S}_K$.

In Appendix A, we go beyond these leading order corrections and provide quantitative bounds on when the peaked-size approximation in Eq. (24) is valid. In general, we can strictly prove that this approximation holds whenever there is a parametric separation between an asymptotic size width, defined in the Appendix, and the average size.

IV. PEAKED-SIZE TELEPORTATION

We are now ready to demonstrate how the coupling leads to teleportation of a quantum state when size distributions are tightly peaked. We first demonstrate this in its simplest context: teleportation of a single qubit at infinite temperature. We then show that the fidelity of peaked-size teleportation is generally suppressed at finite temperature. For ease of reading, we relegate rigorous results supporting each of the above arguments to the end of the Section.

A. Single-qubit teleportation

To analyze teleportation of a single qubit, we turn to the two-sided correlators in Eq. (11), with $Q_A \in \{\mathbb{1}, X, Y, Z\}$ running over the single-qubit Pauli operators. We recall that the requirements for teleportation are for all C_Q to have (i) maximal magnitude and (ii) the same phase.

The first requirement is naturally satisfied at infinite temperature even *before coupling and decoding* but the second requirement is not. In particular, the four correlators with $D = \mathbb{1}$, $g = 0$ are:

Q_A	C_Q
$\mathbb{1}$	$+1$
X	$+1$
Y	-1
Z	$+1$

$(D = \mathbb{1})$
$(g = 0)$

where the left entries are qubit operators, Q_A, and the right entries are the correlators, C_Q. The correlators have maximal magnitude because each operator can be transferred perfectly from left to right using Eq. (7). However, the Y operator picks up an overall minus sign during this process, since $Y^T = -Y$, and so the correlator phases are not aligned. One can verify the resulting teleportation fidelity is indeed trivial. Our goal will be to show that the action of the coupling in Eq. (24), as well as a simple decoding operation, are sufficient to align the four phases.

To begin, we assume that all time-evolved Pauli operators have a tightly peaked size distribution and that the average size $\mathcal{S}$ is the same for all non-identity operators. From Eqs. (24-25), we have that the coupling applies a total phase difference $g_d\mathcal{S}/N$ between the thermofield double state (the identity operator; size zero) and all perturbed states (time-evolved Pauli operators; size $\mathcal{S}$). Our table of correlator phases is thus modified to:

Q_A	C_Q
$\mathbb{1}$	$+1$
X	$+1$
Y	-1
Z	$+1$

$(D=\mathbb{1})$ $(g=0)$ $\longrightarrow$

Q_A	C_Q
$\mathbb{1}$	$e^{ig_d\mathcal{S}/N}$
X	$+1$
Y	-1
Z	$+1$

$(D=\mathbb{1})$ $(g\neq 0)$

We again do not achieve perfect phase alignment. However, we can now correct the misaligned phases using the decoding operator, $D = Y$. This applies an additional minus sign to the X and Z correlators:

Q_A	C_Q
$\mathbb{1}$	$+1$
X	$+1$
Y	-1
Z	$+1$

$(D=\mathbb{1})$ $(g=0)$ $\longrightarrow$

Q_A	C_Q
$\mathbb{1}$	$e^{ig_d\mathcal{S}/N}$
X	$+1$
Y	-1
Z	$+1$

$(D=\mathbb{1})$ $(g\neq 0)$ $\longrightarrow$

Q_A	C_Q
$\mathbb{1}$	$e^{ig_d\mathcal{S}/N}$
X	-1
Y	-1
Z	-1

$(D=Y)$ $(g\neq 0)$

The correlator phases are now aligned whenever

$$g_d \frac{\mathcal{S}}{N} = \pi \bmod 2\pi, \tag{27}$$

leading to perfect teleportation at these values.

B. Finite temperature teleportation

There are two important modifications to peaked-size teleportation at finite temperature. First, the relevant notion of operator size is modified [24]. In particular, in the peaked-size regime, the difference in phase applied between the identity and non-identity Pauli operators is modified to

$$\mathcal{S}[Q_A(t)] \to \mathcal{S}[Q_A(t)\rho^{1/2}] - \mathcal{S}[\rho^{1/2}]. \tag{28}$$

Second, the maximal fidelity of peaked-size teleportation is reduced at finite temperature. In particular, when sizes are tightly peaked, the two-sided correlators factorize into a constant magnitude multipled by an overall phase:

$$\begin{aligned} C_Q &= \langle \mathrm{TFD}|\, \tilde{Q}^\dagger_{A,r} Q_{A,l}\, |\mathrm{TFD}\rangle\, e^{i(g-g_d\mathcal{S}_K[Q_A(t)\rho^{1/2}]/K)} \\ &= G_\beta(Q_A)\cdot e^{i\theta_Q} \end{aligned} \tag{29}$$

where θ_Q combines the effects of transposition, coupling, and decoding, and the correlator magnitude corresponds to an imaginary-time Green's function,

$$G_\beta(Q_A) \equiv \mathrm{tr}(Q_A^\dagger \rho^{1/2} Q_A \rho^{1/2}) \leq 1. \tag{30}$$

This Green's function is unity at infinite temperature and generically decreases at finite temperatures, due to the reduced entanglement of the TFD state. This violates the maximal magnitude requirement for teleportation, and therefore leads to a corresponding decrease in the teleportation fidelity.

The astute reader will recall that finite temperature teleportation is known to succeed with higher fidelities than G_β in the case of gravitational teleportation [1, 7, 16]; this is a signature of physics outside the peaked-size regime, which we connect to in Section VII.

C. Rigorous expressions for teleportation fidelity

We now derive formal expressions of the teleportation fidelity for n teleported qubits as a function of the correlator phases. To do so, we consider a variant of the protocol where instead of teleporting a quantum state we attempt to distill an EPR pair:

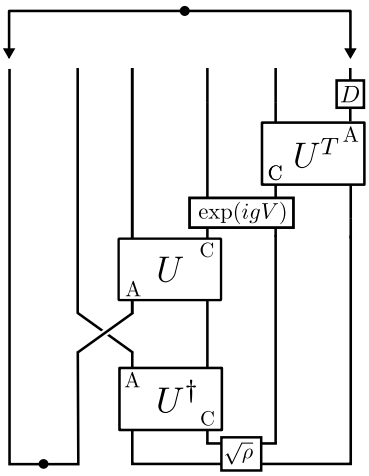

(31)

The fidelity of EPR distillation is precisely related to the average fidelity of state teleportation [11], $F_{\mathrm{EPR}} = [(d_A+1)\langle F_\psi\rangle - 1]/d_A$, where $d_A = 2^n$ is the dimension of subsystem A when teleporting n qubits.

We calculate the teleportation fidelity by Pauli decomposing the SWAP operator as $\mathrm{SWAP} = \sum_{Q_A} Q_A \otimes Q_A^\dagger/d_A$. This gives:

$F_{\rm EPR} =$ 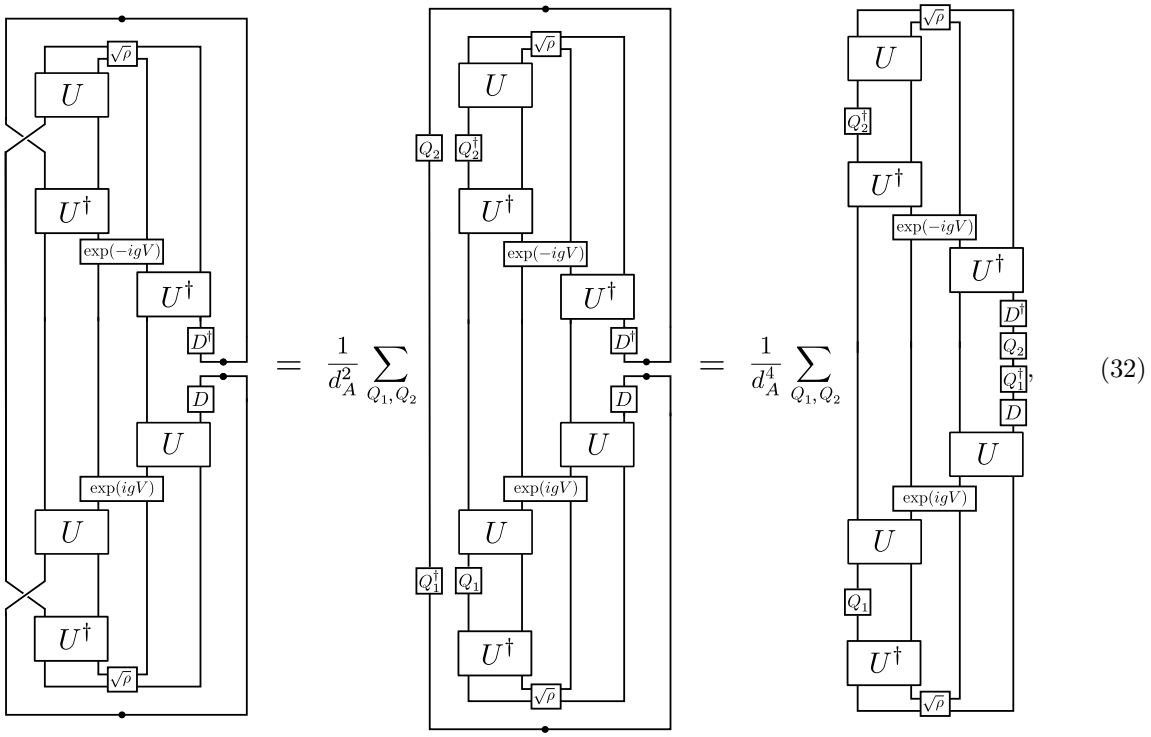 (32)

or

$$F_{\rm EPR} = \frac{1}{d_A^4} \sum_{Q_1,Q_2} \langle {\rm TFD}|\, Q_{2,l}(t)\, e^{-igV}\, \tilde{Q}^\dagger_{2,r}(-t) \times \tilde{Q}^\dagger_{1,r}(-t)\, e^{igV}\, Q_{1,l}(t)\, |{\rm TFD}\rangle\,. \tag{33}$$

Similar expressions for teleportation of quantum states are contained in Appendix C.

In general, the teleportation fidelity and two-sided correlators are related only by a lower bound,[5]

$$F_{\rm EPR} \geq \left| \frac{1}{d_A^2} \sum_{Q_A} C_Q \right|^2 . \tag{34}$$

This is obtained diagrammatically by inserting an identity, $\mathbb{1} = D_r U_r U_r^\dagger D_r^\dagger$, followed by the projector $|{\rm TFD}\rangle\langle{\rm TFD}|$, into the center of Eq. (32):

$\frac{1}{d_A^4} \sum_{Q_1,Q_2} \geq \frac{1}{d_A^4} \sum_{Q_1,Q_2}$ 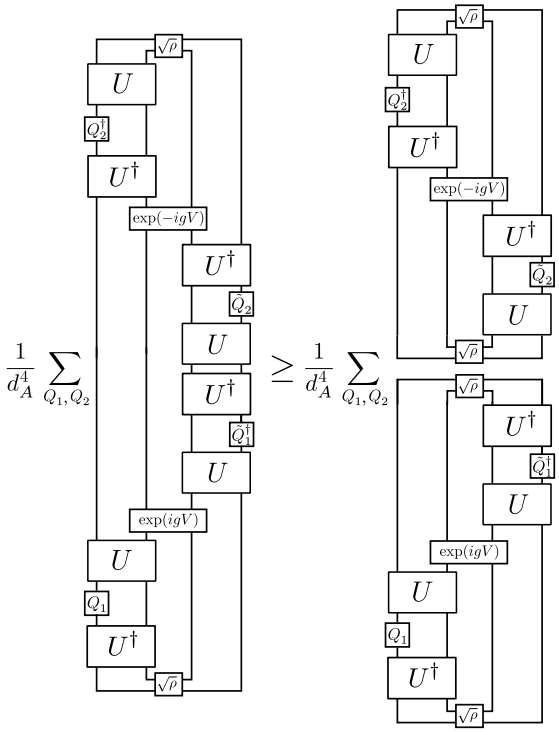 (35)

A similar bound was obtained in Ref. [14, 15], conditional on certain assumptions about operators' size distributions.

[5] Under special circumstances, namely large-N models, one may be able to factorize the above expression in terms of correlators of the form Eq. (11) [16].

At infinite temperature *in the peaked-size regime*, we have $C_Q = e^{i\theta_Q}$ and the fidelity is equal to the lower bound:

$$F_{\text{EPR}} = \frac{1}{d_A^4}\sum_{Q_1,Q_2} e^{i(\theta_{Q_1}-\theta_{Q_2})} = \left|\frac{1}{d_A^2}\sum_{Q_A} e^{i\theta_Q}\right|^2. \quad (36)$$

The sum is over d_A^2 terms, and is unity only when all the operators' phases are the same. At finite temperature in the peaked-size regime, we instead find

$$\begin{aligned} F_{\text{EPR}} &= \frac{1}{d_A^4}\sum_{Q_1,Q_2} e^{i(\theta_{Q_1}-\theta_{Q_2})}\,\text{tr}\Big(Q_2^\dagger Q_1^\dagger\,\rho^{1/2} Q_1 Q_2\,\rho^{1/2}\Big) \\ &\leq \frac{1}{d_A^2}\sum_{Q_A} G_\beta(Q_A). \end{aligned} \quad (37)$$

The maximum fidelity is again achieved when the phases align; however, its value is equal to the sum of various imaginary time Green's functions, i.e. the correlator magnitudes [Eq. (30)].

V. LATE TIMES

We now introduce the simplest physical example of peaked-size teleportation: teleportation in any scrambling system after the scrambling time. There are two distinguishing features of this regime: (*i*) the circuit can only teleport a single qubit, i.e. the channel capacity is one, and (*ii*) as for all peaked-size teleportation, the teleportation fidelity is suppressed at low temperatures. We also demonstrate that this regime of peaked-size teleportation, as well as the full quantum circuit implementing the TW protocol, are equivalent to HPR teleportation of a single qubit. In Section VI, we will demonstrate that the limited late time channel capacity can be overcome at intermediate times in many scrambling systems.

A. Teleportation at late times

At late times, the dynamics of a scrambling system can be approximated by a Haar random unitary [22, 50]. In this case, each time-evolved operator, $Q_A(t)$, becomes a sum of random Pauli strings, each with probability $1/d^2$ to be the identity at any individual site. As a result, time-evolved operators have an average size,

$$\mathcal{S} \approx (1-1/d^2)N, \quad (38)$$

and a size width,

$$\delta\mathcal{S} \sim \sqrt{N}, \quad (39)$$

where the scaling is based on the central limit theorem. The K-size distribution takes the same form, replacing N with K, and is tightly peaked as long as K is large (specifically, $g\delta\mathcal{S}_K/K \approx g/\sqrt{K} \ll 1$).

For simplicity, we will focus on late time teleportation at infinite temperature; finite temperature modifications follow according to Section IV B. Using Eqs. (24-25), we find that the coupling applies a relative phase e^{ig} between the identity operator (size zero) and all non-identity Pauli operators (size above) [1]:

$$\begin{aligned} e^{igV}\,|\text{EPR}\rangle &= e^{ig}\,|\text{EPR}\rangle \\ e^{igV} Q_{A,l}(t)\,|\text{EPR}\rangle &= Q_{A,l}(t)\,|\text{EPR}\rangle\,. \end{aligned} \quad (40)$$

The lack of an applied phase for non-identity Pauli operators corresponds to the vanishing of $\langle V\rangle_Q$ at late times, when OTOCs have decayed to zero [see Eq. (25)]. From Section IV A, we see that whenever

$$g = \pi \bmod 2\pi, \quad (41)$$

single-qubit teleportation succeeds.

A brief argument shows that late time teleportion of higher dimensional quantum states is not possible. Consider teleportation of a d-dimensional qudit, with a basis of states $|i\rangle$, $i = 0,\ldots,d-1$. The qudit Pauli operators are generated by the 'clock' and 'shift' operators: $Z\,|i\rangle = e^{i\omega}\,|i\rangle$, with $\omega = 2\pi/d$, and $X\,|i\rangle = |i+1\rangle$. The two generators obey the commutation relation, $XZ = e^{-i\omega}ZX$. After transposition, each Pauli operator, X^pZ^q, becomes

$$(X^pZ^q)^T = Z^{T,q}X^{T,p} = Z^qX^{-p} = e^{-ipq\omega}X^{-p}Z^q. \quad (42)$$

Meanwhile, late time dynamics ensure that the coupling applies an overall phase only to the identity operator. For teleportation to be successful, we would therefore require a decoding operation, D, that acts as $DX^{-p}Z^qD^\dagger \sim X^pZ^q$. Suppose there was such an operator, and consider its action on the generators: $DXD^\dagger = X^{-1}$ and $DZD^\dagger = Z$. The above action implies that commuting the two generators gives a different phase before and after decoding: $DXZD^\dagger = e^{-i\omega}DZXD^\dagger = e^{-i\omega}ZX^{-1}$ and $DXZD^\dagger = X^{-1}Z = e^{+i\omega}ZX^{-1}$. This is a contradiction whenever $e^{+i\omega} \neq e^{-i\omega}$, i.e. whenever $d > 2$.

B. Equivalence to HPR protocol

We now turn to the equivalence between peaked-size teleportation and teleportation in the HPR protocol. The latter was originally introduced to recover information in the Hayden-Preskill thought experiment [10, 22], and is reviewed in detail in Appendix B.

Here, we restrict our attention to teleportation in the deterministic variant of the protocol, of a single qubit at infinite temperature [10, 12]. The protocol takes the

form:

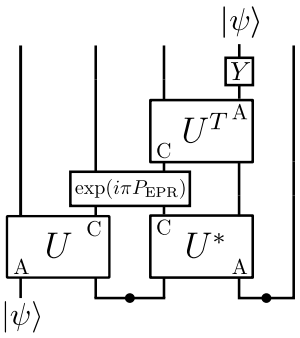

(43)

where P_{EPR} projects onto an EPR pair between subsystems C on the left and right sides.

The equivalence between this protocol and the TW protocol [Eq. (4)] is manifest, with the only difference being the locality of the coupling. Specifically, the HPR coupling is of the same general form as the TW coupling [Eq. (1)]:

$$gV \equiv \pi P_{\mathrm{EPR}} = \frac{\pi}{d_C^2} \sum_{P_C} P_{C,l}\, P_{C,r}^*, \tag{44}$$

where the sum is over of a complete basis of d_C^2 Pauli operators on C. However, the operators P_C are typically non-local across C, whereas the coupling considered in the TW protocol was restricted to local operators. As a consequence, the HPR coupling functions as a binary variable measuring whether or not an operator has support on subsystem C (see Section III). In contrast, the TW coupling measures the operator size within C, which takes an approximately continuous range of values when C is large. Crucially, at late times under scrambling dynamics, the effect of both couplings will be the same: to apply an overall phase to non-identity operators.

A few additional remarks are in order. First, while the leading order effect of the HPR and TW couplings is the same, they lead to different finite-size corrections. In particular, in a fully scrambled system, the variance in the phases applied by the HPR coupling is equal to the probability of a random Pauli string not having support on C, which is suppressed exponentially in the size of C, i.e. $1/d_C^2$. On the other hand, the variance in phases applied by the TW coupling is suppressed only polynomially, by $\sim g^2/K$ [Eq. (39)]. These enhanced phase fluctuations are relevant for finite-size implementations of the TW protocol, as discussed further in Section VIII.

Second, it has previously been shown that an extended version of the HPR protocol allows for teleportation of *multiple* qubits at late times [10]. Because of the equivalence between the protocols, this extension would also allow for multi-qubit teleportation via the peaked-size mechanism. However, the enhanced channel capacity comes with a trade-off: the circuit complexity (measured by the number of applications of the unitary U) grows exponentially in the number of qubits to be teleported. As we will see in the following Section, this limitation can be overcome by peaked-size teleportation at intermediate times (in the original TW protocol), owing to the locality of the TW coupling.

VI. INTERMEDIATE TIMES

We now turn to analyze the behavior of peaked-size teleportation at intermediate times, i.e. before the scrambling time. In this regime, multiple qubits can be teleported given a certain condition on the growth of time-evolved operators, namely when the overlap of their size distributions is sufficiently small.

We explicitly demonstrate that this condition is satisfied, and multi-qubit teleporation is possible, in a wide variety of physical systems at infinite temperature. These include random unitary circuits (RUCs) in $\geq$1D, for which peaked sizes naturally occur due to local thermalization within each operator's light cone, and time-evolved operators are non-overlapping due to spatial locality. More surprisingly, we show that multi-qubit peaked-size teleportation can also be achieved in 'fast scrambling', all-to-all coupled systems, including 0D random unitary circuits and the SYK model (at infinite temperature) [17, 22]. In this case, operators are *not* spatially separated at any nonzero time; nonetheless, the overlap of their size distributions remains *probabilistically* small at sufficiently early times.

Finally, we consider the channel capacity—i.e. the maximum number of qubits that can be teleported—of peaked-size teleportation in all-to-all coupled systems. This is an essential question for comparing the capabilities of peaked-size teleportation with those of gravitational teleportation in traversable wormholes [1]. Remarkably, we provide analytic and numerical evidence that the channel capacity of peaked-size teleportation in 0D RUCs, a quite simple microscopic system, is asymptotically equivalent to that of the gravitational mechanism!

A. Multi-qubit teleportation: additive operator sizes

We begin with a few simple examples of multi-qubit teleportation to build intuition. First, consider a unitary U that factorizes as $U = U_1 \otimes \cdots \otimes U_n$, where each U_i acts on a disjoint subsystem. If we insert n qubits individually into the n different subsystems, then the entire protocol decouples into n independent channels and there is no restriction on sending multiple qubits. This trivial example relies on the fact that U does not scramble information across the entire system but only within each disjoint subsystem.

A similar situation occurs even when the dynamics are not factorizable, as long as the teleported qubits are in causally separated regions. For example, consider a $(d \geq 1)$-dimensional system with short-range interac-

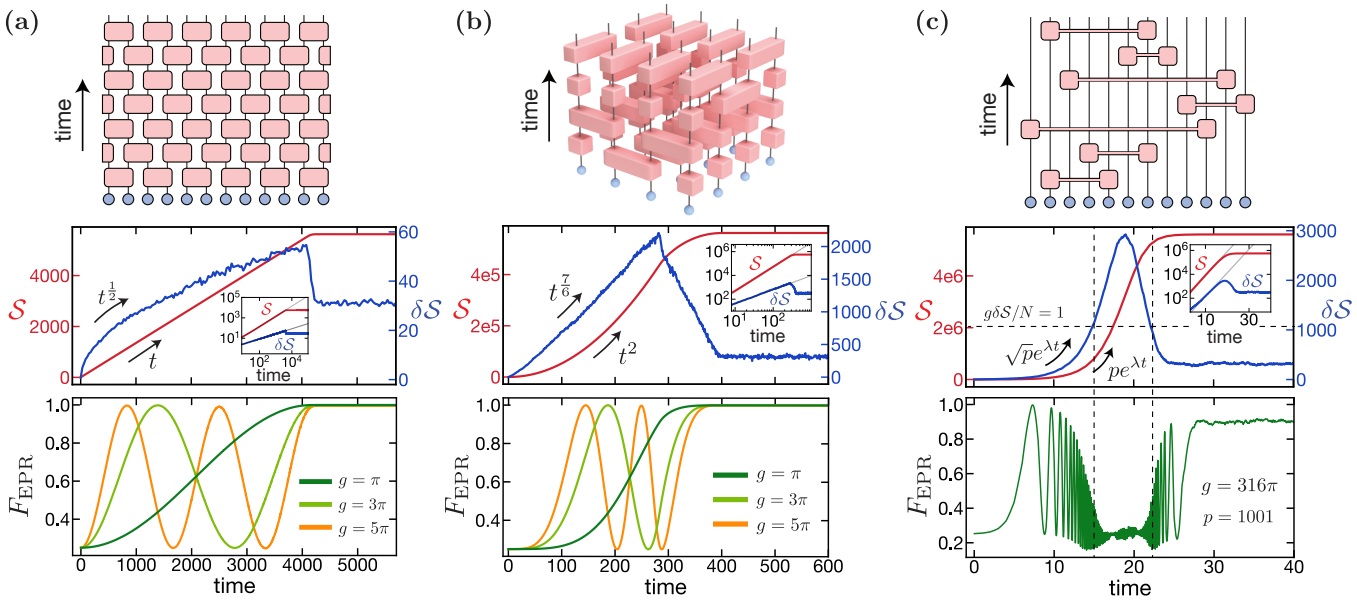

Figure 2. Operator sizes and peaked-size teleportation in 1D, 2D, and 0D RUCs. **(a-b)** In 1D and 2D RUCs, sizes grow ballistically in time, while the size width grows with a slower power of t and matches predictions from the KPZ universality class. For $\mathcal{O}(1)$ values of the coupling strength g, this leads to an oscillatory fidelity at all intermediate times, and saturation to 1 at late times (for teleportation of a single qubit and odd values of g). **(c)** In contrast, in 0D all-to-all coupled RUCs, both the size and size width grow exponentially in time, although they can be parametrically separated using a p-body encoding. The teleportation fidelity reflects this growth, displaying a distinct three-regime profile for $g \gg 1$. At early times and late times, peaked-size teleportation succeeds and the fidelity oscillates as in 1D and 2D. Between these, no teleportation occurs because the size width has grown too large, $g\delta\mathcal{S}/N \gtrsim 1$.

tions, where the inserted qubits are spatially separated. At intermediate times, the time-evolved qubit operators will have support within a local 'light cone' about their initial location, but will continue to act on disjoint subsystems. This scenario is therefore no different from the previous example and multi-qubit teleportation remains possible, as long as (*i*) the size distributions of each operator is tightly peaked, (*ii*) the coupling V has support within each qubit's light cone, and (*iii*) the light cones of each qubit are non-overlapping. This final requirement constrains the number of qubits that can be sent at a given time t. In particular, the light cone of each operator will have a radius $v_B t$ where v_B is the butterfly velocity. The maximum number of non-overlapping light cones—equal to the total number of qubits n that can be teleported—is therefore $n \lesssim N/(v_B t)^d$, where N is the total system volume.

More formally, we can analyze the success of n-qubit teleportation using the two-sided correlators, C_Q. We are concerned with n-qubit operators $Q(t) = Q_1(t)\dots Q_n(t)$, where each $Q_i \in \{I, X, Y, Z\}$ is a single-qubit Pauli on the i^{th} teleported qubit. We work at infinite temperature and assume that sizes are tightly peaked. Teleportation therefore succeeds whenever all correlators have the same phase.

Inspired by the example of n decoupled protocols, we will take the decoding operator to be the tensor product, $D = Y \otimes \dots \otimes Y$. The combination of transposition and conjugation by D thus applies a minus sign to every single-qubit non-identity Pauli operator. An additional phase is applied by coupling proportional to the size of each operator. For example, for $n = 2$ qubits, we have:

$\mathbb{1} \otimes \mathbb{1}$	1
$Q_1 \otimes \mathbb{1}$	$-1 \times e^{ig_d \mathcal{S}_1/N}$
$\mathbb{1} \otimes Q_2$	$-1 \times e^{ig_d \mathcal{S}_2/N}$
$Q_1 \otimes Q_2$	$(-1)^2 \times e^{ig_d \mathcal{S}_{12}/N}$

where $\mathcal{S}_i$ and $\mathcal{S}_{ij}$ are shorthand for $\mathcal{S}[Q_i(t)]$ and $\mathcal{S}[Q_i(t)Q_j(t)]$. In order for all correlators to have the same phase, we require that $g_d\mathcal{S}_1/N = g_d\mathcal{S}_2/N = \pi \bmod 2\pi$, and that the operator sizes *add*, such that $e^{ig_d\mathcal{S}_{12}/N} \approx e^{ig_d(\mathcal{S}_1+\mathcal{S}_2)/N} = e^{i(\pi+\pi)} = 1$.

This requirements generalize straightforwardly to n qubits. Specifically, teleportation succeeds whenever the single-qubit operator sizes obey $g_d\mathcal{S}_i/N = \pi \bmod 2\pi$ and the multi-qubit operator sizes *add* under operator multiplication:

$$\begin{aligned}&\mathcal{S}[Q_1(t)Q_2(t)\dots Q_n(t)]\\ &\qquad\approx \mathcal{S}[Q_1(t)] + \mathcal{S}[Q_2(t)] + \dots + \mathcal{S}[Q_n(t)].\end{aligned} \tag{45}$$

This latter requirement implies that the phases applied by the coupling, e^{igV}, factorize, and allows the n qubits to be teleported 'in parallel' as in the previous simple examples.

The size addition requirement naturally bounds the channel capacity in terms of the number of couplings,

K. Specifically, the K-size takes integer values between 1 and K. However, the requirement that all three single-qubit Pauli operators have the same K-size increases the minimum K-size to 2. From Eq. (45), this implies that an n-qubit operator has a K-size of at least $2n$, which is only possible if

$$2n \leq K. \tag{46}$$

Indeed, this strict upper bound can also be understood from an information theoretic perspective: teleporting n qubits requires an increase of $2n$ in the mutual information between the left and right sides of the system. Each of the K classical bits sent increases the mutual information by at most 1, so at least $2n$ bits are required.

B. ≥1D random unitary circuits

As a first concrete example of intermediate time peaked-size teleportation, we consider a random unitary circuit (RUC) applied to a lattice of N qubits in one or higher dimensions. At each time step, pairs of neighboring qubits are evolved via independent Haar random unitaries arranged in a 'brick-layer' fashion [Fig. 2(a,b)]. Operator growth in such systems has been studied at great length, and is believed to be a good model for many aspects of information scrambling under Hamiltonian dynamics [33, 51–55].

A key property of Haar random unitary circuits is that the expectation values of many circuit quantities can be computed by replacing the Haar random unitaries with randomly chosen *Clifford* unitaries, thereby enabling efficient classical simulation [33, 56]. Generally, this equivalence holds for any quantity that contains no more than *two* copies each of U and $U^\dagger$ (e.g. the Renyi-2 entropy, or the OTOC); for systems of qubits, it in fact holds for up to three copies [57–59]. From Eq. (33), we see that the teleportation fidelity contains three copies of U and $U^\dagger$, so the average fidelity is efficiently simulable[6]. Moreover, by definition, the size distributions of operators under Clifford dynamics are perfectly tightly-peaked, since a Pauli operator Q_A evolved under a Clifford unitary remains a Pauli string. Hence, the teleportation fidelity can be computed using the simplified expression given in Eq. (36).

In practice, we compute the average EPR fidelity for teleporting n qubits via the following steps. First, we choose a particular U by sampling each 2-qubit unitary from a uniform distribution of 2-qubit Clifford unitaries. Second, we determine the K-size of $UQ_AU^\dagger$ for each n-qubit Pauli operator, Q_A, or, if n is large, for a random subset of these operators; such simulations can be performed efficiently with a time cost that scales linearly with the circuit depth. Third, we compute the fidelity for a given coupling g using Eq. (36), with the phases $\theta_Q = g\mathcal{S}_K/K + \pi\mathcal{S}[Q_A(0)]$, where the latter term captures the fact that decoding and transposition apply a minus sign for each non-identity element of the initial Q_A. Lastly, we average the EPR fidelity over multiple realizations of U.

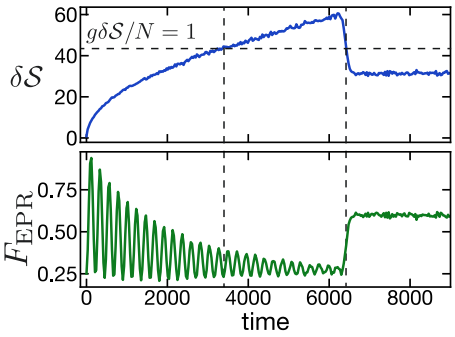

Figure 3. Probing operator size width in a 1D RUC. (top) The size width initially grows as $t^{1/2}$ and reaches a peak at the scrambling time $t^* \sim N = 10000$. (bottom) We probe this behavior by measuring the teleportation fidelity with a large coupling $g = 71\pi \sim \sqrt{N}$. The fidelity exhibits a distinct decay-revival profile, controlled by whether the size width has exceeded the threshold $g\delta\mathcal{S}/N \approx 1$: nearly perfect fidelity initially, power law decay to a trivial fidelity at intermediate times, and partial revival at late times.

The results of these simulations for $n = 1$ qubit in 1D and 2D are shown in Fig. 2(a,b). As expected, the average operator size grows ballistically, $\mathcal{S} \propto t^d$, until the operator's light cone reaches the edge of the system, at which point the size saturates to $3/4N$. While the behavior of the size width is more complex, in both dimensionalities it grows more slowly than the average size. This implies that size distribution is tightly-peaked and the teleportation fidelity can be approximated by $F = \frac{1}{2}[1 - \cos(g\mathcal{S})]$. We verify that the time profile of the fidelity follows this prediction, and nearly perfect fidelity is achieved when $g\mathcal{S} = \pi \mod 2\pi$. In Appendix D, we verify that teleportation of $n > 1$ qubits is also possible at intermediate times, as long as their light cones do not overlap.

Probing the size width—Let us now turn to the time profile of the size width, which exhibits a *peak* near the scrambling time in both 1D and 2D. Qualitatively, this behavior arises from fact that the size width receives contributions from two sources: the interior of the light cone, and the boundary of the light cone. Within the light cone, we expect a ≥1D system with a small local Hilbert space to 'locally thermalize' as the operator spreads. This implies that the bulk's contribution to the size width scales as $\delta\mathcal{S}_{\rm bulk} \propto \sqrt{\mathcal{S}} \propto t^{d/2}$ and saturates at the scrambling time. Second, the size width also receives contributions from the light cone's boundary, which has

[6] For higher-dimensional qudits, while we cannot efficiently simulate the teleportation fidelity, we can still calculate the correlators Eq. (11), which lower bound the fidelity via Eq. (34).

not yet thermalized. At late times, the boundary of the light cone reaches the edge of the system and these additional contributions subside, leading to the peak in the size width at the scrambling time.

To quantify these effects, we note that the growth of operators in ≥1D RUCs is predicted to fall in the Kardar–Parisi–Zhang (KPZ) universality class [33, 60]. In 1D, fluctuations in operator size near the boundary have been verified numerically to have a growing width $\sim t^{\alpha}$ with the KPZ growth exponent $\alpha = 1/2$. This implies that the contribution of the boundary to the size width is $\delta S_{\text{boundary}} \propto t^{1/2}$, and the full width is

$$\delta S = \begin{cases} (\alpha_{\text{bulk}} + \alpha_{\text{boundary}}) t^{1/2}, & t \lesssim t_{\text{scr}} \\ \alpha_{\text{bulk}} t_{\text{scr}}^{1/2}, & t \gtrsim t_{\text{scr}} \end{cases} \tag{47}$$

We note that the maximum size width relative to the late-time size width is a constant set by $(\alpha_{\text{bulk}} + \alpha_{\text{boundary}})/\alpha_{\text{bulk}}$. Comparing the size width of multiple system sizes, we observe excellent agreement with predicted scalings over a wide range of system sizes (Appendix D).

The time profile of the size width is directly observable in the peaked-size teleportation fidelity if we scale $g \sim t_{\text{scr}}^{1/2} \sim N^{1/2}$. In particular, by setting N/g to lie between the maximum size width and the late time size width, we observe a distinct decay-revival profile for the teleportation fidelity (Fig. 3). At early times, we observe successful teleportation with an oscillating fidelity. The fidelity decays slowly, as a power law in time, as it receives corrections proportional to the growing size variance $\sim g^2 \delta\mathcal{S}^2/N^2$. After the scrambling time, we see a revival in the teleportation fidelity as the size width narrows. The lack of a parametric separation between the maximum and late time size widths means that late time teleportation will also have some finite error for this value of g.

In 2D, the scaling of the size width also matches predictions from the KPZ universality class. In this case, the width of the boundary scales as $\sim t^{\alpha}$, with $\alpha = 1/3$ [33]. However, to calculate the boundary's contribution to the size width, one must take into account two additional considerations. First, the boundary is 1-dimensional, so its length trivially grows in time as $\sim t$. Second, fluctuations of the boundary are expected to have a finite correlation length, $\xi \sim t^{1/z}$, where $z = 3/2$ is the KPZ dynamic exponent [61]. Thus, the boundary can be modeled as $n_\xi \sim t/\xi = t^{1/3}$ uncorrelated regions, each of length ξ. Each region contributes $\sim \xi t^{\alpha}$ to the size width; adding the uncorrelated contributions from all regions yields a total size width $\delta\mathcal{S} \sim \sqrt{n_\xi}\, \xi\, t^{\alpha} = t^{1/6+2/3+1/3} = t^{7/6}$.

The time profile of the size width in 2D is thus given by

$$\delta S = \begin{cases} \beta_{\text{bulk}} t + \beta_{\text{boundary}} t^{7/6}, & t \lesssim t_{\text{scr}} \\ \beta_{\text{bulk}} t_{\text{scr}}, & t \gtrsim t_{\text{scr}} \end{cases} \tag{48}$$

We confirm these scalings in our numerics (Fig. 2(b) and Appendix D). Notably, the size width is now dominated by the boundary contribution at intermediate times, such that the ratio of the maximum size width to the late time size width scales as $t_{\text{scr}}^{1/6} \sim N^{1/12}$. As in 1D, one can probe this behavior using the peaked-size teleportation fidelity, now with $g \sim N/t_{\text{scr}}^{7/6} \sim N^{5/12}$. We emphasize that in 2D, the scaling of the size width is determined by *correlations* between different points on the light-cone boundary. This goes beyond the behavior studied in previous works on RUCs, which focus on quantities probed by local OTOCs.

C. 0D random unitary circuits

We now turn to random unitary circuits in zero dimensions, a prototypical model for 'fast scramblers' [17, 22]. We construct these circuits as follows: at each time-step, we partition the N qubits into randomly chosen pairs, and apply independent Haar random 2-qubit unitaries to each pair. As before, such circuits are efficiently simulable via Clifford numerics.

Peaked sizes—In all-to-all coupled systems, operators are generally expected to grow exponentially in time, $\mathcal{S} \sim e^{\lambda t}$, where λ is the Lyapunov exponent. The reason is simple: at each time step, every term in an operator—rather than just those on a 'light-cone' boundary—has a fixed probability of spreading under random pairwise unitaries. A somewhat less intuitive expectation is that the size width also generally grows exponentially. One way of understanding this is by imagining two realizations of the dynamics: in one realization the initial operator doubles at the first time and in the other it does not. In effect, the latter system now lags behind the former by one time step, Δt, and the difference in their sizes at later times will be exponentially magnified, to $e^{\lambda t}(1 - e^{-\lambda \Delta t})$.

The lack of separation between the size and size width seems to preclude the possibility of peaked-size teleportation at intermediate times. Nevertheless, we can engineer such a separation by *encoding* the information of each input qubit into p-body operators, with $p \gg 1$. As an example, consider encoding a single qubit into $p = 5$ qubit operators via

$$\begin{aligned} E(X \otimes \mathbb{1} \otimes \mathbb{1} \otimes \mathbb{1} \otimes \mathbb{1}) E^\dagger &= Z \otimes X \otimes X \otimes Y \otimes Z \\ E(Y \otimes \mathbb{1} \otimes \mathbb{1} \otimes \mathbb{1} \otimes \mathbb{1}) E^\dagger &= Y \otimes Z \otimes Z \otimes X \otimes Y \\ E(Z \otimes \mathbb{1} \otimes \mathbb{1} \otimes \mathbb{1} \otimes \mathbb{1}) E^\dagger &= X \otimes Y \otimes Y \otimes Z \otimes X, \end{aligned} \tag{49}$$

Here, E is a Clifford unitary encoding operation that conjugates state insertion and decoding [explicitly, replacing $U \to UE, U^* \to U^* E^*$, and $U^T \to E^T U^T$ in Fig. 1(a)]. The success of teleportation is now dependent on the size distributions of time-evolved p-body operators, $Q_A(t) = UEPE^\dagger U^\dagger$, where P runs over the initial unencoded single-qubit Pauli operators. As we will soon verify explicitly, before the scrambling time the support of each of the p operators composing Q_A will be approximately non-overlapping, so that their size distributions will convolve. Thus, the total operator size is multiplied

by a factor of p but, through the central limit theorem, the size width is multiplied only by $\sqrt{p}$.

In more detail, consider the size growth of an operator, Q_A, with initial size $\mathcal{S}_0 = p$. During a single time step, each qubit i in the support of $Q_A(t)$ is paired with another random qubit; for simplicity, we assume the second qubit is outside the support of $Q_A(t)$, which should be valid at times well before the scrambling time. Under random two-qubit Clifford time-evolution, $Q_A(t)$ grows to have support on both qubits with probability $\eta = 1-2(d^2-1)/(d^4-1)$ (9/15 for qubits). The operator size, $\mathcal{S}_t$, therefore grows stochastically in time, according to

$$\begin{aligned}\mathcal{S}_{t+1} &= \mathcal{S}_t + \sum_{i=0}^{\mathcal{S}_t} s_i \\ &= \mathcal{S}_t + \mathrm{Bi}_t(\mathcal{S}_t, \eta) \\ &\approx (1+\eta)\mathcal{S}_t + \sqrt{\mathcal{S}_t \eta(1-\eta)}\,\mathcal{N}_t(0,1)\end{aligned} \tag{50}$$

where each s_i is a binary random variable that increases the size by 1 with probability η and 0 with probability $1-\eta$, and $\mathrm{Bi}_t(\mathcal{S}_t, \eta)$ denotes the binomial distribution with $\mathcal{S}_t$ trials and probability η, which we can approximate as a normal distribution, $\mathcal{N}_t(\eta\mathcal{S}_t, \sqrt{\mathcal{S}_t\eta(1-\eta)})$. The size at arbitrary times can be written as a sum of random variables drawn at each time step:

$$\begin{aligned}\mathcal{S}_t \approx &(1+\eta)^t p \\ &+ \sqrt{\eta(1-\eta)} \sum_{t'=0}^{t-1} (1+\eta)^{t-t'-1} \sqrt{\mathcal{S}_{t'}}\,\mathcal{N}_{t'}(0,1)\end{aligned} \tag{51}$$

from which we see that the average size grows exponentially in time with Lyapunov exponent $e^\lambda = 1+\eta$. Deviations arise at each time step t', with typical magnitude $(1+\eta)^{t-t'-1}\sqrt{\mathcal{S}_{t'}} \approx (1+\eta)^{t-1-t'/2}\sqrt{p}$. Since this decays exponentially in t', we can approximate the total variation, $\delta\mathcal{S}_t$, as the largest term in the sum ($t' = 0$), which has magnitude

$$\delta\mathcal{S}_t \sim (1+\eta)^{t-1}\sqrt{p} \approx \frac{\mathcal{S}_t}{\sqrt{p}}. \tag{52}$$

As anticipated, the size width is dominated by early time errors that have exponentially grown in time, so that the ratio of the size width to the size remains constant at $\sim 1/\sqrt{p}$.

To support these claims, we numerically simulate the time-evolved size distribution of operators with an initial size $p \approx 1000$ [Fig. 2(c)]. As expected, we observe that the average size grows exponentially as $\sim pe^{\lambda t}$ and saturates at a timescale $t^* \sim \log(N/p)$. Moreover, the size width grows at the same exponential rate but its magnitude is suppressed by a factor of $\sqrt{p}$ compared to the average size.

To verify that this allows for teleportation, we next compute the fidelity for teleporting a single qubit, in the regime $g \gg 1$. As shown in Fig. 2(c), teleportation occurs with near perfect fidelity beginning at $t \approx t^* - \log(gp)$, corresponding $g\mathcal{S}/N \approx 1$. Thereafter, the teleportation fidelity decreases exponentially in time, consistent with the increase of the size width. At time $t \approx t^* - \log\big(g\sqrt{p}\big)$, teleportation stops succeeding entirely, since the size width has reached the limit $g\delta\mathcal{S}/N \approx 1$. Finally, at late times $t \approx t^* - \log(p)$, the fidelity revives as the system becomes fully scrambled and the operator size width narrows to $\delta\mathcal{S} \sim \sqrt{\mathcal{S}}$.

Size addition—We now turn to the possibility of teleporting multiple qubits in 0D RUCs. Within the peaked-size regime, this reduces to the question of whether operator sizes add according to Eq. (45). Satisfying this requirement in all-to-all coupled systems is not as trivial as in $\geq$ 1D, since time-evolved operators typically act on overlapping subsystems at any finite time. Nevertheless, we now provide a simple argument for why size addition holds despite this.

To do so, we model each time-evolved Pauli operator $Q_i(t)$ as an independent random Pauli string of size $\mathcal{S}[Q_i]$. Consider two such strings, P_1 and P_2, with support on regions A_1 and A_2 and sizes $\mathcal{S}[P_1] = |A_1|$ and $\mathcal{S}[P_2] = |A_2|$. The size of the product, P_1P_2, is the size of the union $A_1 \cup A_2$, minus the number of sites where the two strings overlap and have the same single-qubit Pauli operator. This occurs with probability $1/(d^2-1) = 1/3$ at each site in the region $A_1 \cap A_2$, giving

$$\begin{aligned}\mathcal{S}[P_1P_2] &\approx |A_1 \cup A_2| - \frac{1}{3}|A_1 \cap A_2| \\ &= \mathcal{S}[P_1] + \mathcal{S}[P_2] - \frac{4}{3}|A_1 \cap A_2|.\end{aligned} \tag{53}$$

The deviation from the simple additive rule $\mathcal{S}[P_1P_2] = \mathcal{S}[P_1] + \mathcal{S}[P_2]$ is thus controlled by $|A_1 \cap A_2|$.

For n-qubit teleportation, one must consider the combined size, $\mathcal{S}[P_1 \dots P_m]$, of m independent Pauli strings, where m takes a typical value $m \approx 3n/4$ (a typical n-qubit operator has non-identity support on $3n/4$ qubits). In general, this quantity will receive corrections from $\binom{m}{k}$ different k-way intersections of the strings, for all $2 \leq k \leq m$. For random Pauli strings, the expected size of these intersections scales as $\overline{|A_1 \cap \dots \cap A_k|} = \prod_{i=1}^k \frac{|A_i|}{N} \sim \mathcal{S}^k/N^{k-1}$, where $\mathcal{S}$ is the typical size of a single Pauli string. For a given k, the correction to size addition will be the sum of $\binom{m}{k} \sim m^k$ different intersections and therefore scales as $m\mathcal{S}(m\mathcal{S}/N)^{k-1}$. These corrections can be neglected if they are small compared to the total size; this occurs when $m\mathcal{S} \ll N$, which corresponds to a timescale much less than the scrambling time.

To demonstrate this claim, we numerically simulate the teleportation protocol with $n > 1$ qubits in the regime $1 \ll p, np \ll K$ [Fig. 4]. Analogous to single-qubit teleportation, the teleportation fidelity exhibits oscillations beginning at $t \approx t^* - \log(gp)$, and vanishes at $t \approx t^* - \log\big(g\sqrt{pn}\big)$ due to the growth of the combined size width. However, in contrast to the single-qubit case, teleportation of multiple qubits is not possible at late

times, $t \gtrsim t^* - \log(gpn)$, as predicted in Section V. Interestingly, between these two regimes, we observe a partial revival of the fidelity: this indicates that the operator size widths begin to narrow before the additive condition is completely invalidated.

Error analysis—While we have confirmed that multi-qubit teleportation can be achieved in certain ideal limits, a key question remains: how does the maximum number of qubits that can be teleported scale as a function of K, i.e. what is the protocol's channel capacity? To answer this question, we now estimate how deviations from these ideal limits lead to errors in peaked-size teleportation and ultimately constrain the channel capacity. Throughout this discussion, we assume that the size, $\mathcal{S}$, is extensive, but K is not; this is the natural regime for probing the channel capacity of the protocol at intermediate times, and is the physical scenario in the context of traversable wormholes [1].

In summary, we identify four distinct sources of error in the multi-qubit teleportation fidelity, $F = 1 - \epsilon$:

1. Errors due to finite p: $\epsilon \sim ng^2\mathcal{S}_K^2/K^2p$
2. Errors due to finite K: $\epsilon \sim ng^2\mathcal{S}_K/K^2$
3. Errors due to imperfect size addition: $\epsilon \sim \left[n^2g^2\mathcal{S}_K^4/K^4 + \dots\right]$, where ellipses indicate higher orders in $(n\mathcal{S}_K/K)^2$
4. Errors due to fluctuations in size addition: $\epsilon \sim \left[n^2g^2\mathcal{S}_K^2/K^3 + \dots\right]$, where ellipses indicate higher orders in $n\mathcal{S}_K/K$

We discuss each of these errors in detail below.

The first and second sources of error are due to imperfectly peaked K-size distributions. The K-size width receives contributions from finite-p corrections, $\sim \mathcal{S}_K/\sqrt{p}$, and finite-$K$ corrections, $\sim \sqrt{\mathcal{S}_K}$ [see the discussion below Eq. (26)]. To translate these into errors in the teleportation fidelity, we multiply the size width by g/K and take the square. This gives fidelity errors $\sim g^2\mathcal{S}_K^2/pK^2$ and $\sim g^2\mathcal{S}_K/K^2$ per teleported qubit.

The third and fourth sources of error arise from imperfect size addition. This leads both to 'systematic' errors, due to the average overlap of operators, as well as 'sampling' errors, due to random fluctuations in this overlap. We begin with the systematic errors: as we recall, the size addition of m time-evolved operators receives corrections from k-way overlaps of the operators, each scaling as $\sim m\mathcal{S}_K(m\mathcal{S}_K/K)^{k-1}$, for $2 \le k \le m$ (rescaling our previous results to the K-size instead of the size). The nonlinear dependence on m indicates that sizes do not add perfectly. Nevertheless, when teleporting an n-qubit initial state for large n, we can correct for the above effect at leading order by using a linear approximation for m^k about its typical value, $(3n/4)^k$. This leads to an effectively smaller operator size, which can be observed in the reduced frequency of the fidelity oscillations for 10-qubit teleportation compared to 1-,3-qubit teleportation in Fig. 4(a). The leading errors after this shift are quadratic in $\delta m \equiv m - 3n/4$, which has a typical magnitude $\delta m \sim \sqrt{n}$. Multiplying by g/K and taking the square, we therefore find multi-qubit fidelity errors $\sim (g\mathcal{S}_K/K)^2(n\mathcal{S}_K/K)^{2k-2}$; at leading order $k = 2$, this gives $\sim n^2g^2\mathcal{S}_K^4/K^4$.

Finally, each intersection above is subject to additional random fluctuations about its average value. When operator sizes are much smaller than the system size, we can treat each intersection as arising from a binomial process, in which case fluctuations are proportional to the square root of the intersection's average size (see Appendix E for a detailed accounting). These add in quadrature for $\sim n^k$ overlaps, producing a total fidelity error $\sim (g^2/K)(n\mathcal{S}_K/K)^k$.

Channel capacity— To define the channel capacity of the teleportation protocol, we fix a per qubit error threshold ϵ_{th}, and determine the maximum number of qubits that can be sent while maintaining a multi-qubit fidelity above this threshold[7], $F \ge 1 - n\,\epsilon_{\text{th}}$. We are interested in how the channel capacity scales with the number of couplings, K, while allowing both g and $\mathcal{S}_K$ (determined by the evolution time) to vary.

In 0D RUCs, all errors increase with g, so it is optimal to set g to its minimal value, $g\mathcal{S}/N = \pi$. This gives a per qubit error

$$\frac{\epsilon}{n} \sim \frac{1}{p} + \frac{1}{\mathcal{S}_K} + \left[\frac{n\mathcal{S}_K^2}{K^2} + \dots\right] + \left[\frac{n^2}{K} + \dots\right]. \tag{54}$$

The first term is negligible in the large p limit and so we will neglect it from here on.

We minimize the remaining terms with respect to $\mathcal{S}_K$. There are two relevant regimes. For $n \lesssim \sqrt{K}$, the minimum is determined entirely by the leading order contributions in $n\mathcal{S}_K/K$ to the error (i.e. neglecting the ellipses). Taking the derivative and setting to zero, we have the minimum at $\mathcal{S}_K^{(1)} \sim K^{2/3}/n^{1/3}$. As we increase n, the optimal size approaches the value $\mathcal{S}_K^{(2)} \sim K/n$. At this point, size addition errors of all orders (i.e. the ellipses) become large, and so the true minimum becomes fixed just below $\mathcal{S}_K^{(2)}$. This crossover between these two minima occurs at $n \sim \sqrt{K}$, at which $\mathcal{S}_K^{(1)} \sim \mathcal{S}_K^{(2)}$.

The above minima give two distinct scalings for the per qubit error and thus the channel capacity. The first minimum has a per qubit error $\epsilon^{(1)}/n \sim (n/K^2)^{1/3}$, which gives rise to a superlinear channel capacity, $n \lesssim \epsilon_{\text{th}}^3 K^2$. However, as we increase K, this capacity eventually surpasses the value $\sqrt{K}$. Above this, the optimal size is given by the second minimum, which has an error $\epsilon^{(2)}/n \sim n/K$, and thus the channel features an asymptotically linear capacity,

$$n \lesssim \epsilon_{\text{th}} K. \tag{55}$$

[7] We note that this definition of channel capacity differs from more conventional definitions [62]; we do not expect this difference to qualitatively affect the scaling of the channel capacity with K, as the fidelity drops off steeply above the capacity [Fig. 4(b)].

This is a stronger instance of the strict general bound Eq. (46). Intuitively, this channel capacity arises because the individual K-sizes must be large, $\mathcal{S}_K \gg 1$, for the K-size to be tightly peaked, while at same time the combined K-size must be much smaller than K, $n\mathcal{S}_K \ll K$, for the K-sizes to add; hence $n \ll K$.

We test this scaling numerically by simulating the teleportation protocol and measuring the per qubit fidelity, F, as a function of n and K. Specifically, for each value of K, we sweep the number of qubits n and determine the maximum qubits that can be sent before the infidelity exceeds a threshold, $1-F = \epsilon_{\text{th}}$. These results are shown in Fig. 4(b) and exhibit a clear linear trend across two orders of magnitude, confirming our prediction of a linear channel capacity.

A few final remarks are in order. First, while in principle the per qubit fidelity can be calculated by taking the n^{th} root of the full n-body fidelity, this approach is numerically unstable for large n. Thus, we instead compute the fidelity of a *single* qubit, while trying to send multiple qubits, using an approach derived in Appendix D. This amounts to performing a sum analogous to Eq. (36), but only including pairs of Q_1 and Q_2 that are equal on all sites except for one.

Second, the range of system parameters that lie within the linear scaling regime is ultimately constrained by the finite total system size, $N = 10^8$. In particular, to maximize the linear scaling regime, we choose $p = 101$ and $\epsilon_{\text{th}} = 0.07$. The former ensures that finite-p errors are negligible, while the latter allows the number of qubits at the threshold to be large enough to access the $n \gtrsim \sqrt{K}$ regime but small enough that the operators are initially dilute, i.e. $n \ll N/p$.

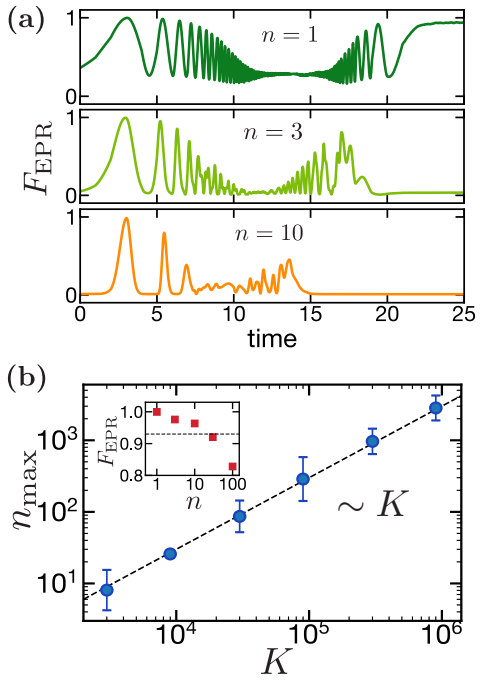

Figure 4. Teleportation of multiple qubits in 0D RUCs. **(a)** Teleportation fidelity as a function of time for teleportation of $n = 1, 3, 10$ qubits. The multi-qubit fidelity decays and revives earlier than the single-qubit fidelity, since multi-qubit operators both have a larger size width and saturate the system size earlier. At late times, teleportation of multiple qubits is not possible and the fidelity is trivial. **(b)** The teleportation fidelity per qubit F decreases as the number of qubits is increased (inset), due to errors in size addition. By setting a threshold for the minimal accepted fidelity (dashed line), we observe a linear scaling of the channel capacity $n_{\max}$ as a function of the number of coupled qubits K.

D. Large-q SYK model: infinite temperature

We now demonstrate peaked-size teleportation in a 0D Hamiltonian system, the large-q SYK model, at infinite temperature. While teleportation at low temperatures in the SYK model is known to succeed via the gravitational mechanism, teleportation at infinite temperature was discovered only recently [16]. In addition to showing that this mechanism is in fact peaked-size teleportation, we also find that, remarkably, *all* qualitative aspects of this teleportation match those of 0D RUCs.

The large-q SYK model is defined by the Hamiltonian [24, 31]:

$$H = i^{q/2} \sum_{1 \le j_1 \le \ldots \le j_q} J_{j_1,\ldots,j_q} \psi_{j_1} \ldots \psi_{j_q}, \tag{56}$$

where ψ_i are Majorana fermions, $\{\psi_i, \psi_j\} = 2\delta_{ij}$, and the couplings are drawn independently from a Gaussian distribution with zero mean and a variance $\langle J^2_{j_1,\ldots,j_q} \rangle = J^2/2q\binom{N-1}{q-1}$.

To construct the teleportation protocol for the SYK model, we first define the N-fermion EPR state,

$$\psi_{j,l} \left|\text{FEPR}\right\rangle \equiv -i\psi_{j,r} \left|\text{FEPR}\right\rangle, \quad \forall\, j = 1, \ldots, N \tag{57}$$

From this, the TFD state is obtained as before,

$$\left|\text{TFD}\right\rangle \equiv e^{-\beta H_l/2} \left|\text{FEPR}\right\rangle. \tag{58}$$

For the two-sided coupling, we consider the simple bilinear interaction,

$$V = \frac{1}{2qN} \sum_{j=0}^{N} i\psi_{j,l}\psi_{j,r}, \tag{59}$$

which measures the size of operators in the Majorana string basis, divided by qN [23, 24].

As in 0D RUCs, the size and size width of time-evolved operators in the SYK model increase exponentially in time, and exhibit a large separation only when initially encoded in p-body operators. To see this, we can generalize previous computations of size distributions in the large-q SYK model [24] to initial p-body operators, $\psi = \psi_1\psi_2 \ldots \psi_p$; this relies on the factorization of SYK

correlation functions in the large-N limit [16]. After the relaxation time ($t \gtrsim 1/J$), but before the scrambling time ($t \lesssim \log(N/p)/J$), the size and size width are:

$$\mathcal{S} \approx \frac{p}{2} e^{2Jt}, \quad \delta\mathcal{S} \approx \frac{\sqrt{2qp}}{4} e^{2Jt}. \tag{60}$$

The scaling $\delta\mathcal{S} \sim \mathcal{S}/\sqrt{p}$ matches that found for 0D RUCs; in particular, ensuring a large separation between the size and size width requires $p \gg 1$.

This large separation suggests that peaked-size teleportation is possible at early times in the large-p limit. To verify this, we analyze the two-sided correlator, which is given by [7]

$$\begin{aligned} C_\psi(t) &= \langle e^{-igV} \psi_r(-t) e^{igV} \psi_l(t) \rangle \\ &= \left(\frac{1}{1 + i\frac{g}{N}\frac{1}{4} e^{2Jt}} \right)^{2p/q} \end{aligned} \tag{61}$$

at infinite temperature before the scrambling time[8]. For large p and early times, we can approximate the correlator as

$$C_\psi(t) \approx \exp\left(-i \frac{g}{qN} \frac{p}{2} e^{2Jt} \right), \tag{62}$$

using $(1 + ix)^m \approx e^{imx}$, valid when $mx^2 \equiv \frac{2p}{q}\left(\frac{g}{N}\frac{1}{4} e^{2Jt}\right)^2 \ll 1$.

Crucially, as expected for peaked-size teleportation, the correlator in this regime corresponds to an overall phase equal the average operator size, Eq. (60), multiplied by g/qN. This indicates that teleportation succeeds with nearly maximal fidelity beginning when $g\mathcal{S}/qN \approx 1$. Teleportation continues to succeed until the above approximation breaks down, which occurs when the size width, $\delta\mathcal{S}$, becomes of order $(g/qN)^{-1}$. As for all scrambling systems, the two-sided correlator is expected to revive at late times, $t \gtrsim \log(N/p)/J$, at which point the sizes saturate the entire system [1, 7] (see Section V); this is not reflected in Eq. (61), which is valid only before the scrambling time.

VII. BEYOND PEAKED-SIZE TELEPORTATION

In this Section, we seek to understand the interplay between peaked-size and gravitational teleportation. A central theme in this understanding is a comparison between the size distribution introduced in Section III, and the *winding size distribution* introduced in Ref. [14, 15].

[8] The inclusion of e^{-igV} in the correlator applies a phase e^{-ig} to the bra on the left side, which conveniently subtracts off the constant term when V to operator size.

To illustrate the distinction between these distributions, consider a time-evolved Majorana fermion operator, decomposed in a basis of Majorana strings, χ:

$$\psi(t)\rho^{1/2} = \sum_\chi c_\chi \chi. \tag{63}$$

From this decomposition, we define the size distribution,

$$P(\mathcal{S}) = \sum_{\chi\,:\,\mathcal{S}[\chi]=\mathcal{S}} |c_\chi|^2, \tag{64}$$

and the winding size distribution [14, 15],

$$f(\mathcal{S}) = \sum_{\chi\,:\,\mathcal{S}[\chi]=\mathcal{S}} c_\chi^2, \tag{65}$$

where $\mathcal{S}[\chi]$ is the size of the string χ. Note that the size distribution is real-valued, while the winding size distribution may be complex.

The teleportation correlators are, in fact, directly related to the winding size distribution:

$$C_\psi(t) = -i \sum_{\mathcal{S}=0}^{\infty} e^{-ig\mathcal{S}/qN} f(\mathcal{S}), \tag{66}$$

which can be derived by explicitly plugging Eq. (63) into the teleportation correlator. The size distribution, by contrast, is related to "one-sided" correlation functions, e.g. Eq. (23), where both instances of the time-evolved operator appear on the same side of the TFD state.

Despite this distinction, we have so far been able to analyze teleportation using the size distribution, as opposed to the winding size distribution, because the two are equal in two circumstances. The first is at infinite temperature, where the coefficients c_χ are real because $\psi(t)$ is Hermitian. The second has been precisely our focus: when size distributions are perfectly tightly peaked, in which case both distributions approach a delta function.

In what follows, we describe several scenarios in which the distinction between the two distributions becomes relevant. First, we analyze the general behavior of the teleportation correlator at early times in large-N systems; this analysis relies on the connection between the teleportation correlator and OTOCs and demonstrates that the correlator deviates from the peaked-size prediction whenever the OTOC contains an imaginary part. Second, we review recent results showing that this deviation eventually leads to low temperature correlators with $\mathcal{O}(1)$ magnitude in models where the winding size distribution takes a particular form, which is conjectured to be the microscopic origin of gravitational teleportation [14, 15]. Third, we return to teleportation in the large-q SYK model and show that this model interpolates between gravitational teleportation at low temperatures and peaked-size teleportation at high temperatures. Surprisingly, this interpolation occurs despite the fact that the large-p encoding ensures a large separation between

the size and size width, i.e. the size distribution naively appears tightly peaked, even at low temperatures. Finally, motivated by this smooth interpolation, we conclude this Section by searching for a 'dual' description of peaked-size teleportation in a bulk gravitational theory. In particular, we argue that strong stringy effects lead to the same qualitative features as peaked-size teleportation.

A. Early time teleportation

Let us begin by considering the first moments of the size and winding size distribution. As we previously saw, the first moment of the former, i.e. the average size, is measured by a one-sided OTOC [Eq. (23)]. Similarly, the first moment of the winding size distribution is given by a two-sided OTOC,

$$\begin{aligned}\mathrm{OTOC}_2 &= i\langle \mathrm{TFD}|\, \psi_{1,r}(-t)\, V\, \psi_{1,l}(t)\, |\mathrm{TFD}\rangle \\ &= \frac{-1}{K}\sum_{i=1}^{K} \\ &= \frac{1}{K}\sum_{i=1}^{K} \mathrm{tr}\Big(\rho^{1/2}\,\psi_1(t)\,\psi_i\,\rho^{1/2}\psi_1(t)\,\psi_i\Big)\end{aligned} \tag{67}$$

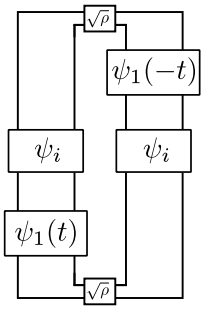

which differs from Eq. (23) in terms of the placement of the thermal density matrix. Just as for the distributions themselves, the two-sided OTOC is equal to the one-sided OTOC at infinite temperature and when sizes are perfectly tightly peaked.

The early time behavior of the teleportation correlator is directly dependent on the first moment of winding size distribution. We have already encountered this in the specific case of peaked-size teleportation, for which the two distributions are equal and the phase of the correlator is given by the operator size (see Section III). To generalize this relation beyond peaked-size regime, we consider two simplifying assumptions. First, we focus on 0D large-N systems, e.g. the SYK model, with a p-body initial encoding. In such systems, the teleportation correlator factorizes into a product of single-body correlators (up to $1/N$ corrections):

$$\begin{aligned}C_\psi(t) &= \left\langle e^{-igV}\psi_r(-t)e^{igV}\psi_l(t)\right\rangle \\ &\approx \left[\left\langle e^{-igV}\psi_{1,r}(-t)e^{igV}\psi_{1,l}(t)\right\rangle\right]^p,\end{aligned} \tag{68}$$

where ψ_1 is a single-body operator.

Second, generalizing Eq. (26), we consider sufficiently early times to work at leading order in g:

$$\begin{aligned}C_\psi(t) &\approx e^{-igp\langle V\rangle}\left[\langle\psi_{1,r}\psi_{1,l}\rangle + ig\langle\psi_{1,r}\,V\,\psi_{1,l}\rangle + \dots\right]^p \\ &\approx e^{-igp\langle V\rangle}\langle\psi_{1,r}\psi_{1,l}\rangle^p\left[\exp\left(igp\frac{\langle\psi_{1,r}\,V\,\psi_{1,l}\rangle}{\langle\psi_{1,r}\psi_{1,l}\rangle}\right) + \dots\right] \\ &= (-iG_\beta)^p\exp\left(-i\frac{gp}{2q}\left[\frac{\mathrm{OTOC}_2}{G_\beta} - G_\beta\right]\right) + \dots \\ &= (-iG_\beta)^p\exp\left(-i\frac{gp}{2qN}G_\beta\mathcal{F}_2(t)\right) + \dots\end{aligned} \tag{69}$$

where $G_\beta = i\langle\psi_{1,r}\psi_{1,l}\rangle = \mathrm{tr}\big(\rho^{1/2}\psi_1\rho^{1/2}\psi_1\big)$ is the imaginary time Green's function, and $\mathcal{F}_2(t)$ is the first-order, connected component of the two-sided OTOC [Eq. (67)],

$$\mathrm{OTOC}_2 \approx G_\beta^2\left(1 + \frac{1}{N}\mathcal{F}_2(t) + \cdots\right). \tag{70}$$

Similar to Eq. (26), the leading correction to Eq. (69) is $\sim pg^2[\langle V^2\rangle_\psi - \langle V\rangle_\psi^2/G_\beta]$, and the approximation holds when this is small.

In chaotic systems, the connected OTOC grows exponentially in time $\mathcal{F}_2(t) \sim e^{\lambda t}$ with a prefactor that is, in general, complex. From Eq. (69), the real part of $\mathcal{F}_2(t)$ causes rapid phase oscillations in the correlator, while the imaginary part increases/decreases the correlator magnitude, depending on the sign of the coupling g. As we have seen, the former is the sole effect at infinite temperature and when sizes are tightly peaked; in such cases, the OTOC is real and equal to the operator size. Outside of these regimes, the real part of $\mathcal{F}_2(t)$—i.e. the phase of the teleportation correlator—is fundamentally distinct from the first moment of the size distribution. Rather, recent work has shown that $\mathrm{Re}\{\mathcal{F}_2(t)\}$ is computable via a ladder diagram identity and is physically interpreted as a 'branching time' [46].

On the other hand, the imaginary part of $\mathcal{F}_2(t)$ is dominant in systems with a gravity dual [32, 46] (as well as other maximally chaotic systems, e.g. maximally chaotic 2D CFTs with a large central charge [63]). It leads to a growth (or decay) in the magnitude of the correlator, which is not possible in peaked-size teleportation. This opens the door to $\mathcal{O}(1)$ teleportation fidelities even at low temperatures [14, 15] (see the following Section). Interpolating between these two limits, it has been conjectured that the prefactor of $\mathcal{F}_2(t)$ is proportional to $e^{i\lambda\beta/4\pi}$ [32, 46]. This would imply that the imaginary part is dominant if and only if $\lambda \approx 2\pi\beta$, i.e. the system approaches the bound on chaos.

B. Gravitational teleportation and the size-winding mechanism

We now move beyond early times and provide a brief review of how the correlator can achieve its maximal mag-

nitude, 1, even at finite temperatures. This occurs via the 'size winding' phenomenon introduced in Ref. [14, 15] as the microscopic mechanism for gravitational teleportation. As we emphasize in Section II, maximizing the magnitude of the correlators is necessary for high fidelity teleportation, but it is not sufficient: we must also align the correlator phases, for every operator on the subspace to be teleported.

To begin, note that the winding size distribution is normalized to the two-point function, $G_\beta \leq 1$, in contrast to the size distribution, which is normalized to 1. From Eq. (65), we see that this norm being less than one implies that the phases of the coefficients c_χ are not perfectly aligned for different strings χ. It is convenient to separate this misalignment into two classes: first, when coefficients of strings of the same size $\mathcal{S}$ are misaligned, which manifests in the magnitude of $f(\mathcal{S})$ being less than maximal for a given $\mathcal{S}$, and second, when the phases of $f(\mathcal{S})$ for different sizes $\mathcal{S}$ do not align with each other.

We focus on the latter case and, more specifically, consider an ansatz in which the coefficients' phases *wind* with the size [14, 15]:

$$c_\chi = e^{i\alpha \mathcal{S}[\chi]} |c_\chi|, \tag{71}$$

In this case, the coupling of the teleportation protocol, by applying a phase that is also proportional to the size, can serve to unwind the phases of $f(\mathcal{S})$ at the value $g/qN = 2\alpha$ [see Eq. (65)]. This increases the teleportation correlator magnitude from its initial value, G_β, to unity. Although seemingly artificial, we next show that this ansatz holds exactly for the SYK model at low temperatures.

C. Large-q SYK model: finite temperature

We now turn to explore the interplay between peaked-size and gravitational teleportation in an explicit example: the large-q SYK model at finite temperature and large-p encoding. Despite the fact that this model features a large separation between the size and size width, we show that teleportation is *not* governed by the peaked-size mechanism at low temperatures, due to the presence of strong size winding.

To begin, let us consider the finite-temperature teleportation correlator, given by [16]:

$$C_\psi(t) = (-iG_\beta)^p \left(\frac{1}{1 - \frac{g}{N}\frac{J}{2\lambda} e^{\lambda t} \sin(\lambda\beta/4) + i\frac{g}{N}\frac{1}{4} e^{\lambda t}} \right)^{2p/q}, \tag{72}$$

where $G_\beta^p = i^p \langle \psi_r \psi_l \rangle = (\lambda/2J)^{2p/q}$ is the p-body two-point function, and the Lyapunov exponent λ corresponds to the solution of $\beta\lambda = 2\beta J \cos(\lambda\beta/4)$, and interpolates between $2\pi/\beta$ at low temperatures and $2J$ at high temperatures. At infinite temperature, the correlator reduces to Eq. (61), and follows our expectations for peaked-size teleportation (see Section VI D). At low temperatures, where the model is known to possess a gravitational dual [30–32], the correlator behaves substantially differently; most notably, its magnitude increases from G_β^p at time zero to unity when $gJe^{\lambda t}/2\lambda N = 1$ [illustrated in Fig. 1(c)].

From this correlator, we can verify the two predictions made in Sections VII A and VII B: (*i*) the early time behavior is governed by the two-sided OTOC, and (*ii*) the size winding mechanism is responsible for the $\mathcal{O}(1)$ peak in the correlator magnitude at low temperatures. To see the former, we expand the correlator at leading order:

$$C_\psi(t) \approx (-iG_\beta)^p \exp\left(-\frac{igp}{2qN} \left[i\frac{2J}{\lambda} e^{\lambda t} \sin(\lambda\beta/4) + e^{\lambda t} \right] \right). \tag{73}$$

Indeed, the term in the exponent is directly proportional to the connected piece of the two-sided OTOC [46],

$$\mathcal{F}_2(t) = i\frac{2J}{\lambda} e^{\lambda t} \sin(\lambda\beta/4) + \frac{1}{N} e^{\lambda t}, \tag{74}$$

matching Eq. (69)[9]. At high temperatures this OTOC is equal to the operator size [Eq. (60)], resulting in phase oscillations, whereas at low temperatures the OTOC rotates to become predominantly imaginary, leading to an exponential growth in the correlator magnitude.

Next, to understand the role of size winding, we must analyze the full winding size distribution. We can derive this distribution by expanding the teleportation correlator in powers of $e^{-ig/qN}$ to match Eq. (66). To do so, it is convenient to consider the exact correlator (before a $g/N \ll 1$ approximation) [16, 24]:

$$C_\psi(t) = (-iG_\beta)^p \left(\frac{e^{-ig/2N}}{1 + i(1 - e^{-ig/N})[\frac{J}{2\lambda}\sin(\lambda\beta/4) + \frac{i}{4}]e^{\lambda t}} \right)^{2p/q} \tag{75}$$

Rewriting this correlator using the Taylor expansion,

$$\left(\frac{1}{1 + (1 - e^{-\mu})x} \right)^{2p/q} = \frac{1}{(1+x)^{2p/q}} \sum_{n=0}^{\infty} e^{-n\mu} \binom{n + \frac{2p}{q} - 1}{n} \frac{1}{(1 + 1/x)^n}, \tag{76}$$

and identifying the n^{th} coefficient with the winding size

[9] More precisely, the correlator in Eq. (73) is missing a factor of G_β^p compared to Eq. (69). This same mismatch is noted in Ref. [24], and is attributed to the large-q limit utilized for the calculation, since in this limit G_β approaches 1.

distribution, we have:

$$f(qn+p) = -\frac{(-iG_\beta)^p}{(1+\frac{J}{2\lambda}e^{\lambda t}e^{-i\lambda\beta/4})^{2p/q}} \times \binom{n+\frac{2p}{q}-1}{n}\frac{1}{(1+\frac{2\lambda}{J}e^{-\lambda t}e^{i\lambda\beta/4})^n}. \tag{77}$$

At intermediate times and large p, the distribution takes a particularly simple form,

$$f(qn+p) \approx (-iG_\beta)^p \frac{(\gamma+i2\alpha)^{2p/q}}{\Gamma(\frac{2p}{q})} n^{\frac{2p}{q}-1} e^{-\gamma n} e^{i2\alpha n} \tag{78}$$

where we define the size decay rate, γ, as

$$\gamma = \frac{2\lambda}{J}e^{-\lambda t}\cos(\lambda\beta/4) = \left(\frac{\lambda}{J}\right)^2 e^{-\lambda t}, \tag{79}$$

and the size winding coefficient, α, as

$$2\alpha = \frac{2\lambda}{J}e^{-\lambda t}\sin(\lambda\beta/4). \tag{80}$$

The above expression holds when $(2p/q)^2 \ll n \ll 1/\gamma^2, 1/\alpha^2$. Crucially, the distribution follows the size winding ansatz, $f(n) = |f(n)|e^{i2\alpha n}$. Thus, we recognize that the maximum in the correlator magnitude occurs when the coupling has unwound the phases of $f(n)$, at $g/N = 2\alpha$, as expected from Section VII B.

The fact that the correlator magnitude increases in time, and moreover reaches an $\mathcal{O}(1)$ value at low temperatures, is a hallmark of gravitational teleportation and signals physics outside the peaked-size regime. Naively, this result is surprising, as we expect the p-body encoding to ensure a peaked size distribution. Indeed, the average size and size width remain separated by $\sqrt{p}$ at all temperatures [24]:

$$\mathcal{S}[\psi(t)\rho^{1/2}] - \mathcal{S}[\rho^{1/2}] \approx \frac{p}{2}\left(\frac{2J}{\lambda}\right)^2 e^{\lambda t} = \frac{2p}{\gamma}, \tag{81}$$

$$\delta\mathcal{S}[\psi(t)\rho^{1/2}] \approx \frac{\sqrt{2qp}}{4}\left(\frac{2J}{\lambda}\right)^2 e^{\lambda t} = \frac{\sqrt{2qp}}{\gamma}. \tag{82}$$

This demonstrates that our simple intuition, of judging a size distribution to be tightly peaked if the ratio between the size width and average size is small, is not always correct. Rather, in Appendix A, we provide a more precise condition for when peaked-size teleportation holds, and explicitly show that this condition breaks down for the SYK model at finite temperature (but remains satisfied at infinite temperature).

Let us now provide intuition for *how* peaked-size teleportation is modified by size winding at low temperatures. To this end, we express the SYK correlator in terms of the winding size distribution parameters:

$$\begin{aligned} C_\psi(t) \approx& (-iG_\beta)^p \frac{(\gamma+i2\alpha)^{2p/q}}{\Gamma(\frac{2p}{q})} \\ &\times \int_0^\infty dn\, n^{\frac{2p}{q}-1}\exp(-\gamma n)\exp(-i[g/N+2\alpha]n). \\ =& (-iG_\beta)^p\left[\frac{\gamma+i2\alpha}{\gamma+i2\alpha+ig/N}\right]^{2p/q} \end{aligned} \tag{83}$$

At early times, this integral can be solved using a saddle-point approximation. At infinite temperature, the saddle point, n_s, occurs precisely at the average size, $n_s = (2p/q)/\gamma = \mathcal{S}/q$, giving the peaked-size correlator, $C_\psi = (-iG_\beta)^p \cdot \exp(-ig\mathcal{S}/qN)$. In contrast, at finite temperature, the size winding α shifts the saddle point in the imaginary direction of the complex plane, giving $n_s = (2p/q)/(\gamma+2i\alpha)$ and a correlator $C_\psi = (-iG_\beta)^p \cdot \exp(-ign_s/qN)$. From this, we recognize the saddle point as precisely the two-sided OTOC, $n_s = \frac{p}{2q}\mathcal{F}_2(t)$.

The inclusion of the size winding in the low temperature saddle point thus has two effects. First, it contributes an imaginary part to the OTOC and thereby increases the magnitude of the teleportation correlator. More subtly, it also alters the *real* part of the OTOC. At low temperatures, $\alpha/\gamma \approx \beta J \gg 1$, and we can approximate the saddle as $n_s \approx (2p/q)/(2i\alpha) + (2p/q\gamma)(\gamma/2\alpha)^2$. Recognizing $\mathcal{S} = 2p/\gamma$, we see that the real part of the OTOC now corresponds to the average size suppressed by two factors of the ratio $(\alpha/\gamma)^2$.

D. Gravity with stringy effects

While the bulk of this paper approaches teleportation firmly through the lens of quantum mechanics, we would be remiss not to explore the analog of peaked-size teleportation in gravitational physics. Specifically, we would like to ask: is there a teleportation mechanism in gravitational systems that shares the same features as peaked-size teleportation? Such a connection might seem surprising, given the prevalence of peaked-size teleportation in quantum mechanical models with no apparent connection to gravity. Nonetheless, the smooth blending between gravitational teleportation and peaked-size teleportation in the SYK model suggests a positive answer.

Here, we demonstrate—in a particular gravitational geometry, AdS_2—that an analog of peaked-size teleportation indeed occurs when strong stringy corrections are included in the gravitational theory. Intuitively, our results are consistent with our previous analysis of the SYK model, where, in the dual gravitational theory, increasing the temperature is known to add stringy effects [32].

Our derivation assumes familiarity with the gravitational description of teleportation in AdS_2, a thorough summary of which can be found in the seminal works of

Refs. [1, 7]. In this setting, the teleportation correlator can be calculated explicitly by considering gravitational scattering in a wormhole geometry. We will maintain our SYK notation, so that V consists of K single-body fermion operators, ψ_i, and our input operator is a p-body fermion, ψ. The correlator can be solved for by decomposing the fermion operators in a momentum basis and applying the scattering matrix:

$$C_\psi^{\rm sc}(t) = e^{-ig\langle V\rangle}\int dk \Psi_r(k,t)\Psi_l^*(k,t) \times \exp\left(ig\int ds e^{i\delta(k,s)} i\Psi_{1,r}(s,0)\Psi_{1,l}^*(s,0)\right) \tag{84}$$

where $\Psi_{l/r}(k,t)$ is the wavefunction for the p-body operator inserted on the left/right boundary with in-falling momentum k (and similarly $\Psi_{1,l/r}(s,0)$ for any single-body operator in V), and $e^{i\delta(k,s)}$ is the scattering matrix element between $\psi(t)$ and $\psi_1(0)$. In pure gravity, i.e. in the absence of stringy effects, these quantities take the form [1]:

$$\Psi_r(k,t)\Psi_l^*(k,t) = \frac{(2ike^{-t})^{2\Delta}e^{-4ike^{-t}}}{i\Gamma(2\Delta)(-k)}\Theta(-k) \tag{85}$$

$$\delta(k,s) = G_N k s \tag{86}$$

where we have set $\beta = 2\pi$ for convenience, $\Theta(x)$ is the Heavyside function, and $\Delta = p/q$ is the conformal weight of ψ. The single-body wavefunction, $\Psi_1(s,0)$, is obtained by setting $t = 0$ and replacing $\Delta \to \Delta_1 = 1/q$ (i.e. the conformal weight of a single fermion).

In the semiclassical limit, we can evaluate the correlator by expanding $e^{i\delta}$ to linear order in G_N [1]. We find:

$$C_\psi^{\rm sc}(t) = \langle\psi_l\psi_r\rangle\,\frac{(-i)4^{2\Delta}}{\Gamma(2\Delta)} \times\int_0^\infty dk\,(-ik)^{2\Delta-1}\exp\left(-i(\tilde{g}G_N e^t - 4)k\right), \tag{87}$$

where $\tilde{g} \equiv g4^{-\Delta_0}\Delta_0/2$. This expression is almost identical to the large-q SYK correlator of Eq. (83), setting the size decay rate to zero, $\gamma = 0$, and identifying the momentum k in the gravitational calculation with the size n in the SYK model [64]. Notably, the correlator diverges at the teleportation time, $4 = \tilde{g}G_N e^t$. In bulk gravity, this divergence is exactly the light-cone pole between the left and right sides of the traversable wormhole, and is regulated by including higher order terms in G_N or stringy corrections [1].

While the full effects of stringy scattering in an AdS background are not known, we will take a phenomenological treatment as in Ref. [1, 45]. Here, the total effect of stringy corrections is to change the scattering amplitude to

$$\delta(k,s) = iG_N(-iks)^\varepsilon,\ 0 \le \varepsilon \le 1, \tag{88}$$

where ε controls the strength of stringy effects, and varies from 1 in pure gravity to 0 in the highly stringy limit.

Again expanding $e^{i\delta}$ to leading order in G_N, and Wick rotating $k \to -ik$, we can write the correlator as

$$C_\psi^{\rm stringy}(t) = \langle\psi_l\psi_r\rangle\,\frac{4^{2\Delta}}{\Gamma(2\Delta)} \times\int dk\,k^{2\Delta-1}e^{-4k}\exp\left(-i^{1+\varepsilon}gG_N A_\varepsilon k^\varepsilon e^{\varepsilon t}\right) \tag{89}$$

where A_ε is a constant of order 1. Note that the k-dependence in front of exponential is a Poisson distribution with a saddle point at $k_s \approx \Delta/2$ in the heavy particle limit, $\Delta = p/q \gg 1$. At early times, $e^{\varepsilon t}G_N \ll 1$, and for strong stringy effects, $\varepsilon \to 0$, the change in this saddle point from the scattering, g, is negligible. In these limits, the saddle point approximation thus gives the correlator:

$$C_\psi^{\rm stringy}(t) \approx \langle\psi_l\psi_r\rangle\exp\left(-igG_N A_\varepsilon(\Delta/2)^\varepsilon e^{\varepsilon t}\right), \tag{90}$$

which has exactly the same form as in peaked-size teleportation [Eq. (29)]! Specifically, the correlator is equal to the two-point function, $G_\beta = i\langle\psi_l\psi_r\rangle$, multiplied by a pure phase. Tentatively, this suggests interpreting the phase as the operator size in a dual boundary theory. This size,

$$\mathcal{S}/N \sim G_N A_\varepsilon(\Delta/2)^\varepsilon e^{\varepsilon t}, \tag{91}$$

grows exponentially in time with a non-maximal Lyapunov exponent, $2\pi\varepsilon/\beta$.

A few remarks are in order. First, while in the above treatment the strength of stringy effects depends on a 'free' parameter ε, we expect that in a UV complete theory ε would in turn depend on the temperature (and other physical parameters). In particular, we expect $\varepsilon \to 1$ at low temperature in theories that are dual to pure gravity, and $\varepsilon \to 0$ at high temperature, where stringy, UV effects should play an important role. This statement also follows from the point of view of the boundary field theory, since the scattering matrix is proportional to an OTOC of the boundary theory, which is real at infinite temperature.

Second, if we would like to recover the infinite temperature SYK correlator, Eq. (61), from the scattering computation, choosing a proper ε as a function of β is not enough. One also needs to modify the *wavefunction* of ψ, to:

$$\Psi_r(k,t)\Psi_l^*(k,t) = \frac{\varepsilon(2ik^\varepsilon e^{-\varepsilon t})^{2\Delta}e^{-4ik^\varepsilon e^{-\varepsilon t}}}{i\Gamma(2\Delta)(-k)}\Theta(-k) \tag{92}$$

Such a wavefunction modification due to UV data should be model dependent, and it would be interesting to understand how to derive this 'stringy-corrected' wavefunction from the bulk point of view. Nevertheless, one particular feature of the modified wavefunction has a clear motivation from the boundary perspective. Specifically, Wick rotating Eq. (92), $k \to -ik$, leads to a distribution whose width, $\delta k \sim \Delta^{1/\varepsilon}$, *broadens* as $\varepsilon \to 0$. This broadening increases the phase variations in the exponential of

Eq. (89) and results in the decay of the correlator at the timescale $e^{\varepsilon t} G_N/\sqrt{\Delta} \approx 1$ for small ε. From the boundary point of view, this decay corresponds to the requirement that the size width must be small, $g\delta\mathcal{S}/N \lesssim 1$, for peaked-size teleportation, as we saw for 0D RUCs and infinite temperature SYK (Section VI). We expect this decay to be common to many 0D quantum systems at high temperatures, which suggests that the broadening of the bulk stringy wavefunction as $\varepsilon \to 0$ might also be a general feature.

Finally, the most obvious effect of a non-unity ε is to change the scattering phase, $\delta(k, s)$, from being real-valued to complex. Indeed, in the strong stringy limit, $\delta(k, s)$ becomes purely imaginary. In general scattering theory, a complex δ means that the scattering matrix, $e^{i\delta}$, is no longer normalized, and implies the existence of inelastic scattering [45]. Since peaked-size teleportation is replicated in the limit $\varepsilon \to 0$, this suggests a more general relationship between peaked sizes and inelastic scattering. In Appendix G, we demonstrate that these two phenomena also coincide at infinite temperature, for arbitrary wavefunctions and scattering amplitudes.

VIII. EXPERIMENTAL PROPOSALS

Having illustrated the wide breadth of physics that enters into the teleportation protocol, in this Section we outline explicitly how one can probe this physics in the laboratory. We begin with a qualitative guideline on using the teleportation circuit to probe scrambling physics. Next, we introduce a 'one-sided' implementation of the teleportation circuit, which eliminates the need to experimentally prepare the thermofield double state. This one-sided circuit can be efficiently implemented in several state-of-the-art experimental platforms. The fundamental requirement is the ability to time-evolve forwards and backwards under many-body scrambling dynamics, which is well within reach for existing and near-term quantum simulators with $N \sim 10^2$ qubits [34, 65, 66]. As concrete examples, we present two near-term experimental realizations of our protocol using pristine and replicable atomic qubits: first with neutral atoms and second with trapped ions.

A. Experimental signatures

We begin by outlining the utility of peaked-size teleportation for probing operator size distributions in experiment. As we have seen, in addition to measuring more familiar aspects of the size distribution, i.e. the average size (equivalent to an average OTOC), the teleportation circuit also opens the door to measuring the size width and size addition of operators.

The simplest experimental signal to be detected is any non-trivial teleportation fidelity of a single qubit. This signifies that the implemented unitary is scrambling and has been demonstrated using the HPR coupling [12, 13]. As in the HPR protocol, the success of teleportation is a *robust* signature of scrambling physics, in the sense that it cannot arise from decoherence or experimental error, unlike the decay of OTOCs [11]. Notably, the teleportation protocol represents a 'single-shot' measurement of scrambling in the presence of error, and does not rely upon any outside estimate of the error.

Once teleportation is established, measuring the fidelity as a function of the time parameterizing U probes the size distribution of time-evolved local operators in two ways. First, within the peaked-size regime, oscillations in the teleportation fidelity as a function of time provide a direct measurement of the growth in operator size. In particular, setting $g = 2\pi n + \pi$, one expects to see n oscillations in the teleportation fidelity before it reaches its late time plateau. The peaks in these oscillations give the operator size as a function of time: $\mathcal{S} = (m/n)(1 - 1/d^2)N$ at the m^{th} peak.

Second, since peaked-size teleportation relies on the size *width* $\delta\mathcal{S}$ being small, $g\delta\mathcal{S}/N \lesssim 1$, its success or failure indicates whether the width has surpassed the tunable value N/g. Dependent on the model and the value of g, this leads to an illuminating three-regime profile for the teleportation fidelity as a function of time: initial teleportation when size width is small, no teleportation when $\delta\mathcal{S} \gtrsim N/g$, and late time teleportation once the size width relaxes to its small late time value [as depicted schematically in Fig. 1(c) and observed numerically in 0D RUCs in Fig. 2(c)]. As outlined in detail for 0D, 1D, and 2D RUCs in Section VI, the timescales at which these regimes occur directly probe the scaling of the size width of the distribution.

Moving forward, teleportation of multiple qubits verifies that the sizes of these qubits add under operator composition, and could explicitly demonstrate the equivalent channel capacities of peaked-size and gravitational teleportation. While operator size addition is trivial when the teleported qubits are causally separated under U, determining the requirements for size addition under more general dynamics—e.g. all-to-all or power-law interactions—remains an open question.

Finally, the teleportation protocol can be used as a sharp diagnostic for gravitational physics. Given the presence of peaked-size teleportation in the same circuit, the mere observation of teleportation, even of multiple qubits, is in fact not enough to conclude that gravitational scrambling is present. Instead, we propose to use two experimental signatures that differ starkly between the two teleportation mechanisms: (i) the teleportation fidelity at low temperature, and (ii) the behavior of the teleportation fidelity as a function of time, t, and the coupling strength, g. For the former, the observation of a high teleportation fidelity, $\sim \mathcal{O}(1)$, at low temperatures strongly suggests the occurrence of gravitational teleportation, since the fidelity of peaked-size teleportation is limited at such temperatures by the (small) two-point function, G_β. For the latter, one observes that

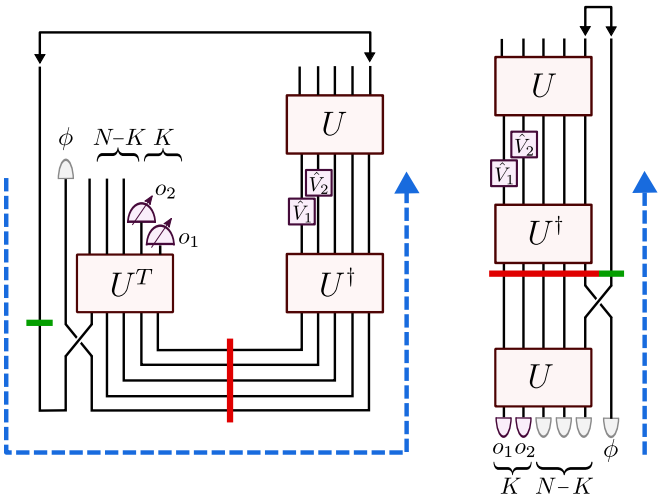

Figure 5. One-sided implementation (right) of the original two-sided teleportation protocol (left) (replacing $U \to U^T$ for convenience, compared to Fig. 1). Blue arrows denote the sequence of operations in the one-sided protocol, while green and red bands mark corresponding sections of the two implementations.

the qualitative profile of the teleportation fidelity as a function of time differs greatly between the two mechanisms (see Fig. 1(c) for a comparison between the two, and Figs. 2, 3 for additional examples of peaked-size teleportation). Furthermore, gravitational teleportation works only for a specific *sign* of the coupling, $g > 0$, while peaked-size teleportation is even as a function of g [1, 7, 14, 15].

B. One-sided implementation of teleportation circuit

Turning towards our experimental proposals, we now introduce a one-sided implementation of the teleportation protocol, at infinite temperature (Fig. 5). This circuit eliminates the need to prepare the highly entangled thermofield double state, at the cost of a higher depth quantum circuit. We derive the one-sided implementation from the 'two-sided' implementation [copied in Fig. 5 from Fig. 1(a)] by sliding all operations from the left side of the thermofield double state to the right side, using Eq. (7). The one-sided implementation then proceeds as follows.

The initial state of the circuit corresponds to the top left of the two-sided implementation. Namely, we initialize the K 'measured' qubits of subsystem C in a definite outcome state, $|o_1 \cdots o_K\rangle$. These states should be drawn from the distribution of measurement outcomes, but when teleporting an EPR pair at infinite temperature they will be uniformly distributed. For the $N-K$ unmeasured qubits, we use the resolution of the identity $\mathbb{1} \propto \sum_s |s\rangle\langle s|$ to replace the unterminated legs with an initial product state in the computational basis, $|o_{K+1} \cdots o_N\rangle$. At the end of the computation, one should average over all 2^{N-K} states. Finally, we include one additional ancillary qubit for each qubit to be teleported, whose initial state is sampled over a complete basis $|\phi\rangle$ for subsystem A. Similar to the unmeasured qubits, this corresponds to the unterminated leg of the thermofield double state when we insert the teleported qubit $|\psi\rangle$ in the two-sided implementation.

Having defined an initial pure state, we now implement the circuit starting from the top left of the two-sided implementation and proceeding counter-clockwise (Fig. 5). The circuit consists of three successive applications of U or $U^\dagger$, interspersed with a swap gate exchanging the 'teleported' subsystem A of U with the ancillary qubit(s), and operations $\hat{V}_i = e^{igo_i\hat{O}_i/K}$ determined by the initial state of the 'measured' qubits. The outcome of the circuit is an EPR measurement between the ancilla qubit and subsystem A.

Compared to the two-sided implementation, the only practical drawback of the one-sided implementation is the additional overhead associated with summing over the initial states of the $N-K$ unmeasured qubits [10]. Crucially, this does not yield an exponential overhead as the sum can be approximated through sampling, requiring a number of realizations that is quadratic in the desired fidelity. Perhaps even simpler, the same result can computed 'physically' by initializing the qubits in a maximally mixed state instead. In either case, for measuring operator size it is most accurate to take $K \approx N$, in which case the overhead is negligible.

A more philosophical difference is that the one-sided implementation no longer performs teleportation, but rather prepares an EPR pair from an otherwise scrambled, many-body system. Specifically, we know that upon swapping out, subsystem A is maximally entangled with the remaining qubits whenever the unitary, U, is scrambling; the one-sided circuit then acts to distill this entanglement into an output EPR pair. This connection has been noted in gravity, where the one-sided protocol can be interpreted as distilling the partner operators of emitted Hawking radiation [67, 68] or observing behind the horizon in the SYK model [69].

C. Implementation with neutral Rydberg atoms

One particularly promising platform for implementing the traversable wormhole protocol is a quantum simulator based on neutral alkali or alkaline-earth atoms held in a reconfigurable and controllable array of optical dipole traps. Recent experiments have already achieved near-deterministic trapping and loading of atoms into

[10] Note that averaging over the K measured qubits should not be considered overhead because it would also be required in the two-sided variant.

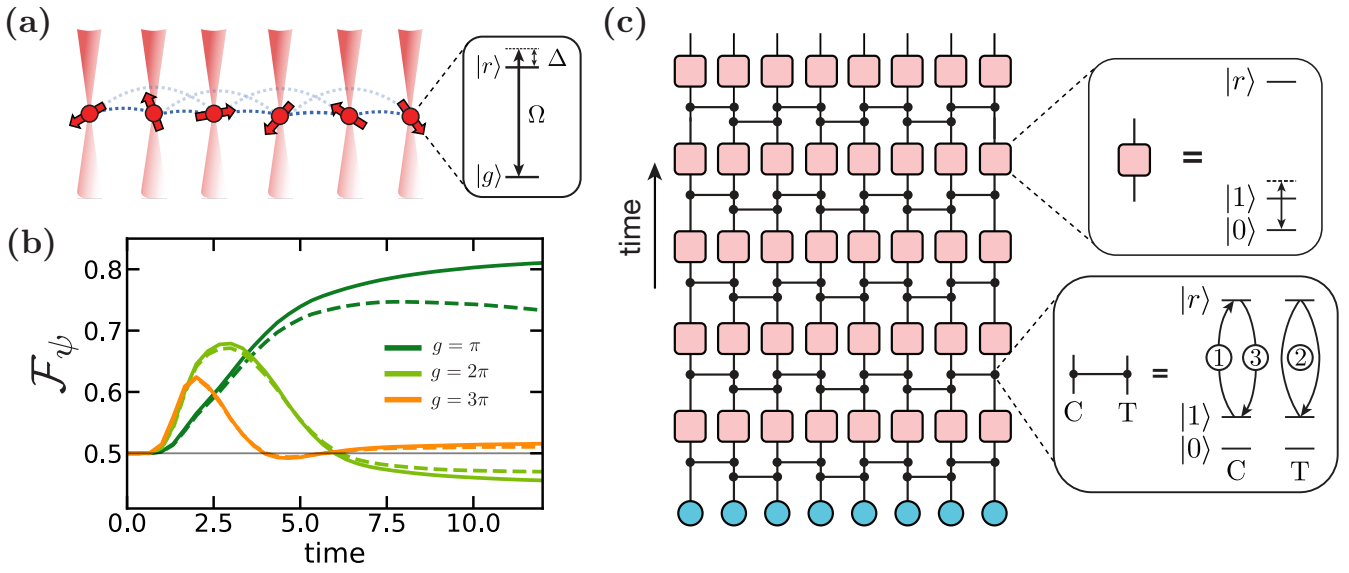

Figure 6. **(a)** In the proposed analog Rydberg teleportation protocol, qubits are encoded in a ground state $|g\rangle$ and a Rydberg state $|r\rangle$. Nearest-neighbor interactions (dark blue) can be time-reversed, but next-nearest neighbor interactions (light blue) cannot. **(b)** Numerical results comparing the teleportation fidelity with perfectly reversed time-evolution (solid) with the proposed, imperfect time-reversal (dashed), for $N = 20$ spins and $\Omega_i = .9$, $\Delta_i = -1.5$, $V_0 = 1$. **(c)** In the digital protocol, qubits are encoded in two hyperfine ground states. Time evolution is performed by alternating layers of controlled-phase gates between nearest neighbor atoms and single-qubit rotations (red boxes). Insets show possible pulse sequences to implement the controlled-phase gate and the single-qubit rotations [70].

arbitrary geometries in one, two, and three dimensions [35, 71, 72]. By leveraging the strong dipole coupling between atomic Rydberg states, high-fidelity analog quantum simulations and digital gates have also recently been demonstrated [34–39]. These demonstrations have primarily used two natural schemes of encoding qubits into neutral atoms:

1. A qubit can be encoded by choosing an atomic ground state $|g\rangle$ to be the $|0\rangle$ state, and a highly excited Rydberg state $|r\rangle$ with principal quantum number $n \gg 1$ as the $|1\rangle$ state [see Fig. 6(a)].

2. Alternatively, the qubit states can be chosen as two long-lived hyperfine ground states (for alkali atoms or fermionic alkaline earth atoms) or a ground state and a metastable clock state (for bosonic alkaline earth atoms), such that the $|1\rangle$ state can be coupled to a Rydberg state to perform entangling gates [see Fig. 6(c)].

We will show how both encodings can be used to realize the teleportation protocol in feasible near-term experiments. We find that the first encoding is naturally suited 'analog' time-evolution under the native (Ising-type) Hamiltonian for a Rydberg setup, but is fundamentally limited to smaller system sizes of $\lesssim 30-35$ qubits (in one spatial dimension) due to the inability to perfectly time-reverse long-range interactions. On the other hand, the second encoding is more flexible and allows for digital time-evolution including RUCs and Floquet dynamics. This time-evolution can be reversed exactly and is limited only by qubit and gate fidelities. While we will primarily consider realizations of our protocol in experimental setups where the neutral atoms are individually trapped in optical tweezers and undergo (near-)resonant excitation to Rydberg states, we also conclude by discussing how similar physics can be seen in an optical lattice setup where the atoms are primarily in ground states $|0\rangle$ and $|1\rangle$, but one of these states is 'dressed' by an off-resonant laser field which couples it to a Rydberg state [73–75].

Analog implementation—We first consider the encoding where the qubit states $|0\rangle$ and $|1\rangle$ correspond to a ground state $|g\rangle$ and a highly excited Rydberg state $|r\rangle$. While neutral atoms are effectively non-interacting in their ground states, nearby atoms interact strongly via van der Waals interactions $\propto n^{11}/r^6$ if they are both in the Rydberg state, where r is the distance between the atoms. Thus, if we drive the transition $|g_i\rangle \leftrightarrow |r_i\rangle$ at each site i with tunable Rabi frequency Ω_i and detuning Δ_i [see Fig. 6(b)], the system will undergo analog time evolution under the Hamiltonian

$$H = \sum_i \frac{\Omega_i}{2} X_i + \sum_i \Delta_i (1 - Z_i) + \sum_{i \neq j} \frac{V_{ij}}{4} (1 - Z_i)(1 - Z_j) \tag{93}$$

where $X_i = |g_i\rangle\langle r_i| + |r_i\rangle\langle g_i|$, $Z_i = |g_i\rangle\langle g_i| - |r_i\rangle\langle r_i|$, and $V_{ij} = V_0/|i-j|^6$ is the van der Waals interaction strength between two atoms at positions i and j.

The Hamiltonian in Eq. (93) is scrambling and exhibits a scrambling time limited by the smaller of V_0 and Ω_i,

$t^* \sim N/\min(V_0, \Omega_i)$. To minimize the total evolution time, we set $|\Omega_i| \sim V_0$, so that evolution under H for a time $\sim N/V_0$ implements a fully scrambling unitary U in the teleportation protocol. To implement $U^\dagger$, we reverse the sign of the tunable single-site parameters Ω_i and Δ_i, and reverse the strong nearest-neighbor interactions by conjugating time-evolution via Pauli operators X_i (i.e. applying π-pulses) on every other site.

In a one-dimensional array, the errors in our implementation will arise from two main sources: (i) the finite lifetime of the Rydberg state, which gives rise to a nonzero decoherence rate at each of the N sites, and (ii) the weak next-nearest neighbor interactions $\sim V_0/2^6 = V_0/64$, which cannot be time-reversed simultaneously with nearest neighbor interactions. To estimate the effect of the former, let us consider the specific case of ^{87}Rb atoms excited to the $70S$ Rydberg state [34, 36], which has a lifetime $\tau \approx 150$ μs. Realistically achievable Rabi frequencies and interaction strengths are of order $\sim 2\pi \times 10 - 100$ MHz. The total time to implement the three scrambling unitaries of the teleportation protocol is thus $\sim 3N/|\Omega_i|$; when summed over N qubits and compared to the Rydberg lifetime, this gives an estimated many-body error $\sim 3N^2/|\Omega_i|\tau$.

Errors due to imperfect backwards time-evolution are more fundamentally restrictive to the analog approach. In order to precisely characterize the effects of these errors on the teleportation fidelity, we perform large-scale numerical simulations of the teleportation protocol with the Rydberg Hamiltonian, Eq. (93) [76]. We find that for a one-dimensional chain of up to $N = 20$ atoms, the fidelity under our proposed protocol exhibits a $\sim 10\%$ error at the scrambling time compared to the ideal case [Fig. 6(b)]. This is consistent with a simple estimate, where the error adds coherently over time-intervals $\delta t \sim 1/V_0$ (the local thermalization time), and incoherently at larger time-scales. Within each δt, each atom accumulates an error $\sim (\delta t\, V_0/64)^2$; summed over N atoms and total time $3t^* \approx 3N\delta t$, this gives a total many-body error $\sim 3N^2/64^2$.

Combined with the Rydberg lifetime error, this suggests that near-term experiments should be able to implement many-body teleportation in systems of $N \sim 35$ qubits. We note that in higher dimensions, the smaller relative distance of next-nearest neighbor atoms gives rise to a substantially larger error contribution from imperfect time-reversal, and the analog protocol is not suitable beyond very small system sizes.

Digital implementation—To implement the protocol in larger systems and higher dimensions, we turn to digital time-evolution, using the second type of qubit encoding (i.e. hyperfine ground states) [Fig. 6(c)]. In this approach, we envision applying alternating layers of nearest-neighbor controlled-phase gates and single-qubit rotations. Here, the controlled-phase gates can be implemented by applying a simple pulse sequence to excite and de-excite qubits from the $|1\rangle$ state to the $|r\rangle$ state, so that the wavefunction acquires a -1 phase if either of the two qubits are in the $|1\rangle$ state, but not if both qubits are in the $|0\rangle$ state (see Fig. 6(c) insets) [70]. As demonstrated in recent experiments [77], these Rydberg-mediated controlled-phase gates can be performed in parallel for sufficiently well-separated pairs of qubits, and non-nearest neighbor interactions can be avoided by slightly reducing the parallelism within each layer of controlled-phase gates. Single-qubit rotations can be performed with sufficiently high fidelity such that the overall circuit fidelity is primarily limited by the entangling gates [71, 78].

For a generic choice of gates, the circuit will be fully scrambling when U is composed of $\sim N$ layers of controlled-phase gates. The fidelity of the overall implementation is again limited by the finite lifetime of the Rydberg state, which is populated for time $\sim 1/V_0$ during each controlled-phase gate. Assuming the same experimental parameters as in the analog case, one expects to be able to perform approximately $\Omega\tau \sim 2\pi \times 10^3 - 10^4$ controlled-phase gates within the decoherence time-scale. Thus, in the digital approach, one expects that the teleportation protocol can naturally be implemented for $N \sim 200$ qubits up to the scrambling time.

Interestingly, the digital approach can also be adapted to experiments using Rydberg-dressed neutral atoms in an optical lattice [73–75]. In such a setup, qubits are again encoded in hyperfine ground states. Strong Ising-like interactions are generated by coupling the qubit state $|1\rangle$ to a Rydberg state with a far-detuned laser field. In this way, the Rydberg interaction gives rise to an energy shift for two neighboring atoms both in the $|1\rangle$ state. Analogous to our previous discussion, a simple scrambling unitary could consist of alternating layers of Rydberg-dressed interactions and single-qubit rotations. While the total accumulated error in the Rydberg-dressing approach is comparable to the gate-based protocol, one potential advantage is an increased tunability of the interactions [79, 80].

In all of the above settings, there are three additional ingredients to the teleportation circuit: (i) the ability to 'swap' in the qubit $|\phi\rangle$ after the first application of U, (ii) the single-qubit rotations $\hat{V}_i$, and (iii) the final measurement in the EPR basis. In both digital setups, these are easily accomplished by combining controlled-phase gates, arbitrary single-qubit rotations, and local measurements. In the analog setup, we propose to temporarily 'turn off' the Hamiltonian by transferring each Rydberg state $|r\rangle$ to a hyperfine ground state (e.g. the state used as $|1\rangle$ in the *digital* protocol) using a resonant laser pulse. Once this is done, all of the above operations can be performed identically as in the digital setup. Afterwards, an additional resonant laser pulse returns the system to the analog encoding.

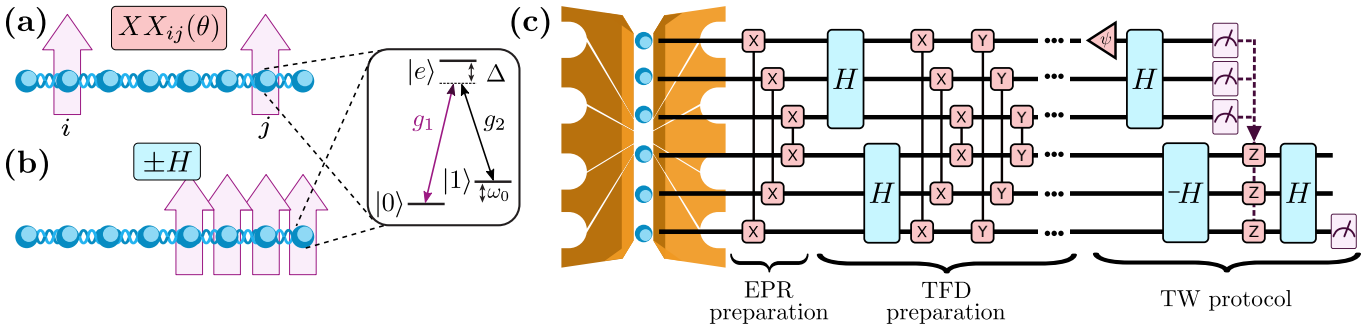

Figure 7. **(a-b)** Chain of atomic ions, with qubit states $|0\rangle$, $|1\rangle$ represented by hyperfine ground states. The states are coupled by a pair of laser beams, one with individual addressing (with strength g_1, purple) and one applied globally (with strength g_2). Each beam is strongly detuned from an excited state $|e\rangle$ by an amount Δ. The coherent beatnote between the beams, at frequency ω_0, drives stimulated Raman transitions between the qubit levels with an effective Rabi frequency $g_1 g_2/2\Delta$, and also modulates the Coulomb interaction between qubits to give rise to an effective Ising interaction. **(a)** A two-qubit entangling gate, $XX_{ij}(\theta)$, (red) is performed by addressing only ions i and j with the first beam. **(b)** Half of the qubits are addressed, which leads to analog time-evolution under the Hamiltonian Eq. (94) (blue) for all addressed spins. **(c)** Quantum circuit implementation of the teleportation protocol at finite temperature. EPR pairs are formed using two-qubit gates. The TFD state is then prepared via a QAOA approach by iterating multiple times between two-qubit gates coupling the sides and analog time-evolution on both sides individually [81, 82]. The state $|\psi\rangle$ is inserted either by projectively measuring the designated qubit and preparing the state, or by digitally swapping in an additional qubit (not shown). Finally, teleportation is implemented using similar ingredients as well as feed-forward measurements (purple dotted lines).

D. Implementation with trapped ions

A second experimental platform, which naturally enables the implementation of our proposed many-body teleportation protocol, is arrays of individual trapped atomic ions [83–85]. Trapped ion qubits feature near-perfect replicability, negligible idle errors, and the ability to implement both a universal set of reconfigurable quantum gates [44] as well as analog long-range spin Hamiltonians [40, 41]. Entangling quantum gates have been demonstrated between isolated pairs of trapped ions with fidelities exceeding 99.9% [42, 43]. Teleportation protocols—including the HPR protocol [12]—involving gate operations, partial measurement and feedforward operations, have been experimentally realized in a number of contexts [4, 5, 12, 86].

Compared to Rydberg atom arrays, trapped ions offer two new regimes for exploring many-body teleportation. First, trapped ions naturally interact via a long-range analog Hamiltonian, whose time-evolution can be fully reversed. Implementing the TW protocol in this setting would provide a window into operator spreading and size distributions under such long-range dynamics [87, 88]. Second, when operated digitally, the same long-range interaction enables the preparation of thermofield double states [81, 82, 89, 90], paving the way towards a realization of the two-sided TW protocol at finite temperature.

We begin by outlining the analog and digital forms of time-evolution that are possible in trapped ion systems. Interactions between qubits typically stem from state-dependent optical dipole forces that off-resonantly drive motional sidebands of the qubit [91, 92]. These phonon sideband operations mediate entanglement and give rise to an effective Ising coupling. When the optical forces are symmetrically detuned far from the upper and lower sidebands, the motion is only virtually excited, resulting in a long-range Ising Hamiltonian [Fig. 7(b)]:

$$H = \sum_{i<j} J_{ij} X_i X_j + B_z \sum_i Z_i, \tag{94}$$

where $J_{ij} \approx J_0/|i-j|^\alpha$, $0 < \alpha < 3$, and the effective magnetic field B_z can be realized by slightly asymmetrically detuning the driving field [93].

On the other hand, when the optical dipole forces are closer to resonances of the motional modes, one can mediate interactions significantly faster, allowing for the execution of rapid, entangling quantum gates between pairs of illuminated ion qubits [Fig. 7(a)] [94, 95]. The native entangling gates are based upon Ising interactions between any selected pair of ions with a tunable interaction angle; in particular, both $XX_{ij}(\theta) = e^{-iX_iX_j/2}$ and $YY_{ij}(\theta) = e^{-i\theta Y_iY_j/2}$ gates are available and $\theta = \pi/2$ naturally creates an EPR pair [96, 97]. Typical entangling and single qubit operations have durations of ~ 100 μs and ~ 5 μs, respectively, while decoherence time-scales are on the order of ~ 1000 s [42, 43].

Let us now describe an implementation of the one-sided TW protocol [Fig. 5]. We first focus on the ability to implement both U and its inverse $U^\dagger$. For analog time-evolution (Eq. 94), $U^\dagger$ can be implemented by changing the sign of the detuning [98], while for digital time-evolution, one can directly invert and reverse the ordering of the quantum gates.

The one-sided protocol also requires the ability to locally address a sub-extensive number of individual qubits. In particular, a subset K of the qubits, which are initially

prepared in a product state, $|o_1, \ldots, o_K\rangle$, must each be rotated by $\hat{V}_i = e^{igo_i\hat{O}_i/K}$ at a later time. These rotations can be achieved by taking $\hat{O}_i = \hat{Z}_i$ and individually addressing the target ions using an auxiliary "poke" laser beam [85, 99].

Following the first application of U, one must swap out the qubit(s) corresponding to the teleported subsystem. This swap can be implemented either digitally by applying a SWAP-gate, or physically, by exchanging the two ions via a modulation of the ion trap's axial fields [41, 100, 101].

Extending this implementation to the two-sided protocol [Fig. 1(a)] at *infinite temperature* is straightforward. Initialization into EPR pairs can be accomplished via simple Ising gates at the input of the circuit [Fig. 7(a,c)], while time-evolution can again take the form of either digital quantum gates [Fig. 7(a)] or analog Hamiltonian dynamics. To separately implement analog dynamics on the two sides of the system, one would illuminate only *half* of the ion chain at any given time [Fig. 7(b)]; this has the added benefit of avoiding unwanted coupling between the left and right sides, but implies that the time-evolution must be performed serially [Fig. 7(c)].

Finally, in the two-sided protocol, one must perform projective measurements on K qubits that feed-forward to the conditional rotations, $\hat{V}_i$. These partial measurements can be accomplished by using multiple ion species (i.e. different elements or isotopes) [86], or alternatively, this entire procedure can be replaced with a specific interaction, e^{igV}, between the two sides; this interaction is naturally realized via an $XX_{ij}(\theta)$ gate with $\theta = 2g/K$.

Implementing the two-sided protocol at *finite temperature* requires all of the above ingredients, in addition to the ability to prepare an entangled thermofield double state. Interestingly, the TFD state can be prepared variationally using the quantum approximate optimization algorithm (QAOA) [81, 82], and requires no additional experimental capabilities beyond those already necessary for the TW protocol. The optimization step within a QAOA-based TFD preparation relies on a cost function that requires one to measure the entanglement entropy between the two sides [81, 82]. While challenging, this can in principle be experimentally realized by either using several copies of the system [102–104] or via randomized measurements [105], both of which have been demonstrated in trapped ion experiments [106, 107].

IX. OUTLOOK

In this work, we developed a unified framework for understanding many-body teleportation from the perspective of operator growth under scrambling dynamics. The unifying concept within this framework is the size distribution of time-evolved operators [14, 15, 23–25]: these form the backbone of peaked-size teleportation, and provide a more fine-grained measure of operator growth compared to the average operator size (as given by the expectation value of OTOCs).

Our work suggests several future directions for applying and building upon this framework. First, while we have studied the size distributions in 0D and $\geq$ 1D RUCs, it would be interesting to extend this analysis to a multitude of other physical systems, where one expects to find qualitatively distinct behavior. These include long-range interacting systems [108, 109], interacting and non-interacting integrable systems [25], $\geq$ 1D systems with a large on-site Hilbert space [110], 0D systems with sparse couplings [111], and systems with conserved quantities [52].

Another set of open questions concerns the notion of operator size at finite temperature. In systems with peaked size distributions, we found that the phase of the two-sided teleportation correlator was directly proportional to the conventional definition of operator size [24]. Surprisingly, we observed that this relationship did not hold in the finite temperature SYK model; rather, the phase was given by the real part of the two-sided OTOC. Unlike the conventional size, this OTOC is not UV divergent, and is thus expected to be inherently independent of the microscopic Hilbert space. Recent work has shown that its real part isolates an incoherent component of operator spreading in large-N models [46]; further work is needed to establish and expand this framework. Related to these considerations, one may hope to better understand the bulk analogue of operator size in theories dual to gravity with strong stringy effects. While we have seen that stringy effects can mimic peaked-size teleportation, developing a physical interpretation of this correspondence would be extremely exciting.

Third, we have shown that a promising application of the teleportation protocol is to distinguish between different classes of scrambling dynamics. In particular, we have focused on two classes of scramblers—generic thermalizing systems and those with gravitational duals—and demonstrated that the key distinction between them is their teleportation fidelity at low temperatures. It is intriguing to ask whether the fidelity increase associated with gravitational teleportation may also occur in other systems, without a gravitational dual. For instance, recently the teleportation correlator magnitude was observed to increase slightly above G_β in non-local random Hamiltonian systems [14, 15]; generalizing this to other physical models would be of tremendous interest.

One may also wonder what role an extensive low temperature entropy—a key feature of the SYK model [31]—plays in the teleportation process. In particular, how well can systems with extensive low temperature entropy but no known gravitational dual teleport [112, 113]? We conjecture that an extensive entropy would allow one to *locally* encode each qubit into low-energy degrees of freedom (i.e. operators with an $\mathcal{O}(1)$ two-point function), since one would only require $\mathcal{O}(1)$ qubits on the left side of the TFD in order to have one qubit of mutual information with the right side. Such an encoding would allow low temperature teleportation with perfect fidelity if op-

erator sizes were peaked, naturally motivating the study of operator size distributions in such models.

From an experimental perspective, using teleportation as a near-term diagnostic of scrambling necessitates a greater understanding of the effects of experimental imperfections on the protocol. Most significantly, we have already noted that the teleportation fidelity acts as a robust indicator of scrambling in the presence of experimental error, in the sense that it can rise to unity only when scrambling is present [11]. However, it is unclear how other signatures of the protocol, e.g. the oscillations and decay/revival profile of the teleportation fidelity, are affected by errors, and to what extent these effects can be mitigated through post-processing [114].

As an additional experimental direction, we note that one can precisely measure the size distribution of operators via small modifications to the teleportation protocol, in two distinct ways. In the first, one directly measures the operator size as a quantum mechanical observable, in which case the probability distribution of measurement outcomes equals the size distribution. In the two-sided protocol, this is achieved by measuring the coupling, V, after state insertion and time-evolution. This can also be generalized to the one-sided protocol, for infinite temperature and classical couplings. A second approach is to measure the *characteristic function* of the size distribution (i.e. its Fourier transform). At infinite temperature, this is precisely equal to the correlator, Eq. (2), whose real part can be isolated from the teleportation fidelity of different initial states (see Appendix C) [23, 24]. Measuring the correlator's imaginary part requires one to replace state insertion, e.g. the projection $(1+Z)/2$, with a unitary operation, $(1+iZ)/\sqrt{2}$, in the teleportation protocol. At finite temperature, this procedure naturally probes the winding size distribution (see Section VII A). To obtain the size distribution, one should instead measure a 'one-sided' correlator, which corresponds to performing the same protocol but measuring the final quantum state on the left, not right, side of the TFD state.

Finally, our work has broad implications in the context of quantum coding theory, where many-body teleportation can be understood as an especially generic method of entanglement-assisted quantum error correction (EAQEC). Indeed, the setup for EAQEC is identical to that of the teleportation protocol: two parties, Alice and Bob, share entanglement (the TFD state), Alice applies an encoding circuit to her share of qubits (the left unitary, U), and decoding is achieved by teleporting Alice's quantum state to Bob's share of qubits (via the coupling, V, and unitaries on right). Crucially, because the coupling acts on a subsystem of Alice's qubits, this scheme protects against any errors on her remaining qubits; moreover, which subsystem the coupling acts on is arbitrary, so the encoding protects against errors on *any* subsystem of $N-K$ qubits. Previous schemes for EAQEC have focused primarily on encodings via Clifford unitaries. In contrast, many-body teleportation, and more specifically peaked-size teleportation, succeeds for a *vastly* broader class of encoding procedures—i.e. many-body time dynamics—indicating that naturally occurring, strongly interacting dynamics offer novel methods of EAQEC. These observations suggest a number of potential future directions, including theoretically characterizing the quantum communication capacity of the teleportation protocol for different classes of dynamics, and experimentally realizing EAQEC in quantum simulators.

Note added: After this work had been completed, we learned of an independent investigation of gravitational many-body teleportation by Nezami, Lin, Brown, Gharibyan, Leichenauer, Salton, Susskind, Swingle, and Walker, which will appear in the same arXiv posting.

Acknowledgments: We gratefully acknowledge discussions with Sepehr Nezami, Yingfei Gu, Xiangyu Cao, Jaewon Kim, Yimu Bao, Hannes Pichler, Alexander Keesling, Harry Levine, Geoffrey Pennington, Maxwell Block, Sagar Vijay, and Daniel Jafferis. This work was supported by the U.S. Department of Energy through the Quantum Information Science Enabled Discovery (QuantISED) for High Energy Physics (KA2401032) and through the GeoFlow Grant No. de-sc0019380. This research used resources of the National Energy Research Scientific Computing Center, a U.S. Department of Energy Office of Science User Facility operated under Contract No. DE-AC02-05CH11231. The exact dynamical simulations used the `dynamite` Python frontend [76], which supports a matrix-free implementation of Krylov subspace methods based on the `PETSc` and `SLEPc` packages. T.S. acknowledges support from the National Science Foundation Graduate Research Fellowship Program under Grant No. DGE 1752814. P.G. acknowledges support by the US Department of Energy grants DE-SC0018944 and DE-SC0019127, and also the Simons foundation as a member of the *It from Qubit* collaboration. I.C. acknowledges support from the Alfred Spector and Rhonda Kost Fellowship of the Hertz Foundation and the Department of Defense through the National Defense Science and Engineering Graduate Fellowship Program. E.T.K. acknowledges support from the National Science Foundation Graduate Research Fellowship Program under Grant Nos. DGE1144152 and DGE1745303. N.M.L. acknowledges support from the Maryland—Army-Research-Lab Quantum Partnership under Grant No. W911NF1920181.

[1] J. Maldacena, D. Stanford, and Z. Yang, Fortschritte der Physik **65**, 1700034 (2017).

[2] C. H. Bennett, G. Brassard, C. Crépeau, R. Jozsa, A. Peres, and W. K. Wootters, Physical review letters **70**, 1895 (1993).

[3] M. Barrett, J. Chiaverini, T. Schaetz, J. Britton,

W. Itano, J. Jost, E. Knill, C. Langer, D. Leibfried, R. Ozeri, *et al.*, Nature **429**, 737 (2004).
[4] M. Riebe, H. Häffner, C. Roos, W. Hänsel, J. Benhelm, G. Lancaster, T. Körber, C. Becher, F. Schmidt-Kaler, D. James, *et al.*, Nature **429**, 734 (2004).
[5] S. Olmschenk, D. N. Matsukevich, P. Maunz, D. Hayes, L.-M. Duan, and C. Monroe, Science **323**, 486 (2009).
[6] J.-G. Ren, P. Xu, H.-L. Yong, L. Zhang, S.-K. Liao, J. Yin, W.-Y. Liu, W.-Q. Cai, M. Yang, L. Li, *et al.*, Nature **549**, 70 (2017).
[7] P. Gao, D. L. Jafferis, and A. C. Wall, **2017**, 151 (2017).
[8] N. Bao, A. Chatwin-Davies, J. Pollack, and G. N. Remmen, **2018**, 71 (2018).
[9] J. Maldacena and X.-L. Qi, arXiv preprint arXiv:1804.00491 (2018).
[10] B. Yoshida and A. Kitaev, arXiv preprint arXiv:1710.03363 (2017).
[11] B. Yoshida and N. Y. Yao, Physical Review X **9**, 011006 (2019).
[12] K. A. Landsman, C. Figgatt, T. Schuster, N. M. Linke, B. Yoshida, N. Y. Yao, and C. Monroe, Nature **567**, 61 (2019).
[13] M. S. Blok, V. V. Ramasesh, T. Schuster, K. O'Brien, J. M. Kreikebaum, D. Dahlen, A. Morvan, B. Yoshida, N. Y. Yao, and I. Siddiqi, to appear (2020).
[14] A. R. Brown, H. Gharibyan, S. Leichenauer, H. W. Lin, S. Nezami, G. Salton, L. Susskind, B. Swingle, and M. Walter, arXiv preprint arXiv:1911.06314 (2019).
[15] S. Nezami, H. W. Lin, A. R. Brown, H. Gharibyan, S. Leichenauer, G. Salton, L. Susskind, B. Swingle, and M. Walter, to appear (2021).
[16] P. Gao and D. L. Jafferis, arXiv preprint arXiv:1911.07416 (2019).
[17] Y. Sekino and L. Susskind, **2008**, 065 (2008).
[18] S. H. Shenker and D. Stanford, **2014**, 67 (2014).
[19] D. A. Roberts, D. Stanford, and L. Susskind, **2015**, 51 (2015).
[20] J. Maldacena, S. H. Shenker, and D. Stanford, **2016**, 106 (2016).
[21] P. Hosur, X.-L. Qi, D. A. Roberts, and B. Yoshida, **2016**, 4 (2016).
[22] P. Hayden and J. Preskill, **2007**, 120 (2007).
[23] D. A. Roberts, D. Stanford, and A. Streicher, **2018**, 122 (2018).
[24] X.-L. Qi and A. Streicher, **2019**, 12 (2019).
[25] X.-L. Qi, E. J. Davis, A. Periwal, and M. Schleier-Smith, arXiv preprint arXiv:1906.00524 (2019).
[26] A. Larkin and Y. N. Ovchinnikov, Sov Phys JETP **28**, 1200 (1969).
[27] C. H. Bennett, P. W. Shor, J. A. Smolin, and A. V. Thapliyal, Phys. Rev. Lett. **83**, 3081 (1999).
[28] T. Brun, I. Devetak, and M.-H. Hsieh, science **314**, 436 (2006).
[29] S. Sachdev and J. Ye, Physical review letters **70**, 3339 (1993).
[30] A. Kitaev, "A simple model of quantum holography," (2015).
[31] J. Maldacena and D. Stanford, Physical Review D **94**, 106002 (2016).
[32] A. Kitaev and S. J. Suh, **2018**, 183 (2018).
[33] A. Nahum, S. Vijay, and J. Haah, Physical Review X **8**, 021014 (2018).
[34] H. Bernien, S. Schwartz, A. Keesling, H. Levine, A. Omran, H. Pichler, S. Choi, A. S. Zibrov, M. Endres, M. Greiner, V. Vuletic, and M. D. Lukin, Nature **551**, 579 (2017).
[35] K. M. Maller, M. T. Lichtman, T. Xi, Y. Sun, M. J. Piotrowicz, A. W. Carr, L. Isenhower, and M. Saffman, Phys. Rev. A **92**, 022336 (2015).
[36] H. Labuhn, D. Barredo, S. Ravets, S. de D. Léséleuc, M. Macri, T. Lahaye, and A. Browaeys, Nature **534**, 667 (2016).
[37] T. M. Graham, M. Kwon, B. Grinkemeyer, Z. Marra, X. Jiang, M. T. Lichtman, Y. Sun, M. Ebert, and M. Saffman, Phys. Rev. Lett. **123**, 230501 (2019).
[38] I. S. Madjarov, J. P. Covey, A. L. Shaw, J. Choi, A. Kale, A. Cooper, H. Picher, V. Schkolnik, J. R. Williams, and M. Endres, Nat. Phys. (2020).
[39] J. Wilson, S. Saskin, Y. Meng, S. Ma, R. Dilip, A. Burgers, and J. Thompson, arXiv preprint arXiv:1912.08754 (2018).
[40] R. Blatt and D. Wineland, Nature **453**, 1008 (2008).
[41] C. Monroe and J. Kim, Science **339**, 1164 (2013).
[42] C. J. Ballance, T. P. Harty, N. M. Linke, M. A. Sepiol, and D. M. Lucas, Phys. Rev. Lett. **117**, 060504 (2016).
[43] J. P. Gaebler, T. R. Tan, Y. Lin, Y. Wan, R. Bowler, A. C. Keith, S. Glancy, K. Coakley, E. Knill, D. Leibfried, and D. J. Wineland, Phys. Rev. Lett. **117**, 060505 (2016).
[44] M. Cetina, L. N. Egan, C. A. Noel, M. L. Goldman, A. R. Risinger, D. Zhu, D. Biswas, and C. Monroe, arXiv preprint arXiv:2007.06768 (2020).
[45] S. H. Shenker and D. Stanford, **2015**, 132 (2015).
[46] Y. Gu and A. Kitaev, **2019**, 75 (2019).
[47] H. W. Lin, J. Maldacena, and Y. Zhao, arXiv preprint arXiv:1904.12820 (2019).
[48] L. Susskind, arXiv preprint arXiv:1904.12819 (2019).
[49] H. W. Lin and L. Susskind, arXiv preprint arXiv:1911.02603 (2019).
[50] D. A. Roberts and B. Yoshida, **2017**, 121 (2017).
[51] C. Von Keyserlingk, T. Rakovszky, F. Pollmann, and S. L. Sondhi, Physical Review X **8**, 021013 (2018).
[52] V. Khemani, A. Vishwanath, and D. A. Huse, Physical Review X **8**, 031057 (2018).
[53] T. Rakovszky, F. Pollmann, and C. von Keyserlingk, Physical Review X **8**, 031058 (2018).
[54] Y. Li, X. Chen, and M. P. Fisher, Physical Review B **98**, 205136 (2018).
[55] B. Skinner, J. Ruhman, and A. Nahum, Physical Review X **9**, 031009 (2019).
[56] C. Dankert, R. Cleve, J. Emerson, and E. Livine, Physical Review A **80**, 012304 (2009).
[57] Z. Webb, arXiv preprint arXiv:1510.02769 (2015).
[58] R. Kueng and D. Gross, ArXiv **abs/1510.02767** (2015).
[59] H. Zhu, Phys. Rev. A **96**, 062336 (2017).
[60] M. Kardar, G. Parisi, and Y.-C. Zhang, Physical Review Letters **56**, 889 (1986).
[61] I. Corwin, Random matrices: Theory and applications **1**, 1130001 (2012).
[62] M. A. Nielsen and I. Chuang, "Quantum computation and quantum information," (2002).
[63] P. Gao and H. Liu, arXiv preprint arXiv:1810.01444 (2018).
[64] L. Susskind, arXiv preprint arXiv:1802.01198 (2018).
[65] F. Arute, K. Arya, R. Babbush, D. Bacon, J. C. Bardin, R. Barends, R. Biswas, S. Boixo, F. G. Brandao, D. A.

Buell, *et al.*, Nature **574**, 505 (2019).
[66] B. Yang, H. Sun, R. Ott, H.-Y. Wang, T. V. Zache, J. C. Halimeh, Z.-S. Yuan, P. Hauke, and J.-W. Pan, Nature **587**, 392 (2020).
[67] B. Yoshida, arXiv preprint arXiv:1910.11346 (2019).
[68] B. Yoshida, **2019**, 132 (2019).
[69] I. Kourkoulou and J. Maldacena, arXiv preprint arXiv:1707.02325 (2017).
[70] D. Jaksch, J. I. Cirac, P. Zoller, S. L. Rolston, R. Cote, and M. D. Lukin, Phys. Rev. Lett. **85**, 2208 (2000).
[71] T. Xia, M. Lichtman, K. Maller, A. W. Carr, M. J. Piotrowicz, L. Isenhower, and M. Saffman, Phys. Rev. Lett. **114**, 100503 (2015).
[72] D. Barredo, V. Lienhard, S. De Leseleuc, T. Lahaye, and A. Browaeys, Nature **561**, 79 (2018).
[73] A. W. Glaetzle, M. Dalmonte, R. Nath, C. Gross, I. Bloch, and P. Zoller, Phys. Rev. Lett. **114**, 173002 (2015).
[74] I.-D. Potirniche, A. C. Potter, M. Schleier-Smith, A.Vishwanath, and N. Yao, Phys. Rev. Lett. **119**, 123601 (2017).
[75] J. Zeiher, J. y. Choi, A. Rubio-Abadal, T. Pohl, R. van Bijnen, I. Bloch, and C. Gross, Phys. Rev. X **7**, 041063 (2017).
[76] Our parallelized dynamics code is available open-source as the package `dynamite`: https://dynamite.readthedocs.io/ DOI:10.5281/zenodo.3606826.
[77] H. Levine, A. Keesling, G. Semeghini, A. Omran, T. T. Wang, S. Ebadi, H. Bernien, M. Greiner, V. Vuletic, H. Pichler, and M. D. Lukin, arXiv preprint arXiv:1908.06101 (2019).
[78] H. Levine, A. Keesling, A. Omran, H. Bernien, S. Schwartz, A. S. Zibrov, M. Endres, M. Greiner, V. Vuletic, and M. D. Lukin, Phys. Rev. Lett. **121**, 123603 (2018).
[79] R. van Bijnen and T. Pohl, arXiv preprint arXiv:1411.3118 (2014).
[80] S. de Léséleuc, V. Lienhard, P. Scholl, D. Barredo, S. Weber, N. Lang, H. P. Büchler, T. Lahaye, and A. Browaeys, Science **365**, 775 (2019).
[81] J. Wu and T. H. Hsieh, Phys. Rev. Lett. **123**, 220502 (2019).
[82] D. Zhu, S. Johri, N. M. Linke, K. A. Landsman, N. H. Nguyen, C. H. Alderete, A. Y. Matsuura, T. H. Hsieh, and C. Monroe, arXiv preprint arXiv:1906.02699 (2019).
[83] J. G. Bohnet, B. C. Sawyer, J. W. Britton, M. L. Wall, A. M. Rey, M. Foss-Feig, and J. J. Bollinger, Science **352**, 1297 (2016).
[84] B. Vermersch, A. Elben, L. M. Sieberer, N. Y. Yao, and P. Zoller, Physical Review X **9**, 021061 (2019).
[85] J. Zhang, G. Pagano, P. W. Hess, A. Kyprianidis, P. Becker, H. Kaplan, A. V. Gorshkov, Z.-X. Gong, and C. Monroe, Nature **551**, 601 (2017).
[86] M. D. Barrett, B. DeMarco, T. Schaetz, V. Meyer, D. Leibfried, J. Britton, J. Chiaverini, W. M. Itano, B. Jelenković, J. D. Jost, C. Langer, T. Rosenband, and D. J. Wineland, Phys. Rev. A **68**, 042302 (2003).
[87] D. V. Else, F. Machado, C. Nayak, and N. Y. Yao, Phys. Rev. A **101**, 022333 (2020).
[88] T. Zhou, S. Xu, X. Chen, A. Guo, and B. Swingle, Phys. Rev. Lett. **124**, 180601 (2020).
[89] J. Martyn and B. Swingle, Physical Review A **100**, 032107 (2019).
[90] V. P. Su, arXiv preprint arXiv:2009.04488 (2020).
[91] J. I. Cirac and P. Zoller, Phys. Rev. Lett. **74**, 4091 (1995).
[92] K. Mølmer and A. Sørensen, Phys. Rev. Lett. **82**, 1835 (1999).
[93] C. Monroe, W. Campbell, L.-M. Duan, Z.-X. Gong, A. Gorshkov, P. Hess, R. Islam, K. Kim, G. Pagano, P. Richerme, *et al.*, arXiv preprint arXiv:1912.07845 (2019).
[94] S.-L. Zhu, C. Monroe, and L.-M. Duan, Phys. Rev. Lett. **97**, 050505 (2006).
[95] S. Debnath, N. M. Linke, C. Figgatt, K. A. Landsman, K. Wright, and C. Monroe, Nature **563**, 63 (2016).
[96] K. A. Landsman, Y. Wu, P. H. Leung, D. Zhu, N. M. Linke, K. R. Brown, L. Duan, and C. Monroe, Phys. Rev. A **100**, 022332 (2019).
[97] K. Wright *et al.*, Nat. Commun. **10**, 5464 (2019).
[98] M. Gärttner, J. G. Bohnet, A. Safavi-Naini, M. L. Wall, J. J. Bollinger, and A. M. Rey, Nature Physics **13**, 781 (2017).
[99] J. Smith, A. Lee, P. Richerme, B. Neyenhuis, P. Hess, P. Hauke, M. Heyl, D. Huse, and C. Monroe, Nature Physics **12**, 907 (2016).
[100] W. Hensinger, S. Olmschenk, D. Stick, D. Hucul, M. Yeo, M. Acton, L. Deslauriers, C. Monroe, and J. Rabchuk, Applied Physics Letters **88**, 034101 (2006).
[101] H. Kaufmann, T. Ruster, C. T. Schmiegelow, M. A. Luda, V. Kaushal, J. Schulz, D. von Lindenfels, F. Schmidt-Kaler, and U. G. Poschinger, Phys. Rev. A **95**, 052319 (2017).
[102] A. Daley, H. Pichler, J. Schachenmayer, and P. Zoller, Physical review letters **109**, 020505 (2012).
[103] D. A. Abanin and E. Demler, Physical review letters **109**, 020504 (2012).
[104] S. Johri, D. S. Steiger, and M. Troyer, Phys. Rev. B **96**, 195136 (2017).
[105] A. Elben, B. Vermersch, M. Dalmonte, J. I. Cirac, and P. Zoller, Phys. Rev. Lett. **120**, 050406 (2018).
[106] N. M. Linke, S. Johri, C. Figgatt, K. A. Landsman, A. Y. Matsuura, and C. Monroe, Phys. Rev. A **98**, 052334 (2018).
[107] T. Brydges, A. Elben, P. Jurcevic, B. Vermersch, C. Maier, B. P. Lanyon, P. Zoller, R. Blatt, and C. F. Roos, Science **364**, 260 (2019), https://science.sciencemag.org/content/364/6437/260.full.pdf.
[108] D. V. Else, F. Machado, C. Nayak, and N. Y. Yao, arXiv preprint arXiv:1809.06369 (2018).
[109] M. C. Tran, C.-F. Chen, A. Ehrenberg, A. Y. Guo, A. Deshpande, Y. Hong, Z.-X. Gong, A. V. Gorshkov, and A. Lucas, arXiv preprint arXiv:2001.11509 (2020).
[110] Y. Gu, X.-L. Qi, and D. Stanford, **2017**, 125 (2017).
[111] G. Bentsen, Y. Gu, and A. Lucas, Proceedings of the National Academy of Sciences **116**, 6689 (2019).
[112] O. Salberger, T. Udagawa, Z. Zhang, H. Katsura, I. Klich, and V. Korepin, Journal of Statistical Mechanics: Theory and Experiment **2017**, 063103 (2017).
[113] R. N. Alexander, G. Evenbly, and I. Klich, arXiv preprint arXiv:1806.09626 (2018).
[114] B. Swingle and N. Y. Halpern, Physical Review A **97**, 062113 (2018).

Appendix A: Precise bound for the peaked size regime

As in the main text, we decompose a time-evolved finite temperature operator into a sum of Pauli strings:

$$Q_A(t)\rho^{1/2} = \sum_R c_R(t) S \tag{A1}$$

In this basis, for qubit systems the correlator takes the form

$$C_Q = \langle \mathrm{TFD}| \tilde{Q}^\dagger_{A,r}(-t) e^{igV} Q_{A,l}(t) |\mathrm{TFD}\rangle = e^{ig+i\pi\mathcal{S}[Q_A(t=0)]} \sum_R e^{-ig\mathcal{S}[R]/N} c_R^2(t) = e^{ig+i\pi\mathcal{S}[Q_A(t=0)]} \sum_n e^{ign/N} f(n) \tag{A2}$$

where again $\tilde{Q}^\dagger_{A,r} = DQ^\dagger_{A,r}D^\dagger$ for the decoding operation $D = Y \otimes \ldots \otimes Y$, and we use $\langle \mathrm{TFD}| \tilde{Q}^\dagger_{A,r}(-t) = e^{i\pi\mathcal{S}[Q_A]} \langle \mathrm{EPR}| Q_{A,l}(t)\rho^{1/2}$ for qubit Pauli operators Q_A. Here we define the winding size distribution [14, 15]

$$f(n) \equiv \sum_{S:\mathcal{S}[R]=n} c_R^2(t). \tag{A3}$$

At finite temperature, this size wavefunction is distinct from the size distribution:

$$P(n) \equiv \sum_{S:\mathcal{S}[R]=n} |c_R(t)|^2, \tag{A4}$$

which is a real, normalized probability distribution probed by the *one*-sided correlator [24]

$$\langle \mathrm{TFD}| Q^\dagger_{A,l}(t) e^{igV} Q_{A,l}(t) |\mathrm{TFD}\rangle = e^{ig} \sum_R e^{-ig\mathcal{S}[R]/N} |c_R|^2(t) = \sum_n e^{ign/N} P(n). \tag{A5}$$

Nevertheless, the size distribution bounds the size wavefunction magnitude via the triangle inequality:

$$|f(n)| \le P(n), \tag{A6}$$

with equality achieved when all Pauli operators of size n contribute the same phase to $f(n)$.

The average size and size variance are easily found from the size distribution as

$$\mathcal{S} = \int_0^\infty dn\, n\, P(n), \quad \delta\mathcal{S}^2 + \mathcal{S}^2 = \int_0^\infty dn\, n^2\, P(n) \tag{A7}$$

where we work in the continuum limit replacing sums over the size by integrals for simplicity. We now define the *asymptotic size width with error* ε as the minimal width W_ε about the average size such that

$$1 - \int_{\mathcal{S}-W_\varepsilon}^{\mathcal{S}+W_\varepsilon} dn\, P(n) \le \varepsilon, \tag{A8}$$

i.e. a fraction $1-\varepsilon$ of the size distribution's support is contained in the interval $I = [\mathcal{S}-W_\varepsilon, \mathcal{S}+W_\varepsilon]$ (the lower limit of the integral should be bounded by zero; for simpler notation we'll deal with this by instead defining $P(n) = f(n) = 0$ for $n < 0$). We can now separate the correlator into two pieces, one arising from sizes in the interval I and the other from the interval's complement $\bar{I} = [-\infty, \mathcal{S} - W_\varepsilon] \cup [\mathcal{S} + W_\varepsilon, \infty]$:

$$C_Q = \int_I dn\, f(n) e^{ign/N} + R \tag{A9}$$

where the remainder $R = \int_{\bar{I}} dn\, f(n) e^{ign/N}$ is strictly smaller than ε:

$$\begin{aligned} |R| &= \left| \int_{\bar{I}} dn\, f(n) e^{ign/N} \right| \\ &\le \int_{\bar{I}} dn\, \left| f(n) e^{ign/N} \right| \\ &\le \int_{\bar{I}} dn\, |P(n)| \\ &\le \varepsilon \end{aligned} \tag{A10}$$

Peaked size teleportation occurs in the regime where $gW_\varepsilon/N \ll 1$. In this limit, we can expand

$$e^{ign/N} = e^{ig\mathcal{S}/N}\left[1 + E(n)\right] \tag{A11}$$

where the deviation for $n \in I$ is bounded by

$$|E(n)| \leq \max_{n\in I}\left|1 - e^{ig(n-\mathcal{S})/N}\right| = \left|\sin(gW_\varepsilon/N)\right|, \tag{A12}$$

which holds as long as $gW_\varepsilon/N \leq \pi/2$. We then have

$$\begin{aligned} C_Q &= \int_I dn\, f(n) e^{ig\mathcal{S}/N}\left[1 + E(n)\right] + R \\ &= e^{ig\mathcal{S}/N} G_\beta(Q_A) + R + R' + R'' \end{aligned} \tag{A13}$$

where $G_\beta(Q_A) = \int_0^\infty dn\, f(n) = \mathrm{tr}\left(Q_A^\dagger \rho^{1/2} Q_A \rho^{1/2}\right)$ is the imaginary time two-point function, and the error $R' = e^{ig\mathcal{S}/N}\int_I dn\, f(n)E(n)$ is bounded by

$$\begin{aligned} |R'| &= \left|\int_I dn\, f(n)E(n)\right| \\ &\leq \int_I dn\, |f(n)||E(n)| \\ &\leq \left|\sin(gW_\varepsilon/N)\right| \int_I dn\, |f(n)| \\ &\leq \left|\sin(gW_\varepsilon/N)\right| \end{aligned} \tag{A14}$$

and the second error $R'' = G_\beta(Q_A) - \int_I dn\, f(n)$ is bounded by

$$|R''| = \left|G_\beta(Q_A) - \int_I dn\, f(n)\right| = \left|\int_{\bar{I}} dn\, f(n)\right| \leq \varepsilon. \tag{A15}$$

We therefore conclude that whenever $gW_\varepsilon/N \leq \pi/2$, the deviation of C_Q from the peaked size value is controlled by the upper bound

$$\left|C_Q - e^{ig\mathcal{S}/N} G_\beta(Q_A)\right| \leq 2\varepsilon + \left|\sin(gW_\varepsilon/N)\right| \equiv \mathcal{B}. \tag{A16}$$

Practically speaking, the lowest value of g for successful peaked-size teleportation is $g\mathcal{S}/N = \pi$. Therefore, for a given size distribution, we can guarantee that peaked-size teleportation is possible if we find ε such that $\mathcal{B} \ll G_\beta(Q_A)$, i.e. the error in the correlator is small compared to the correlator magnitude.

We illustrate this with some examples, in the few cases where we can exactly solve for operators' full size distribution. First, consider a thermalized system at late times, which we will approximate by setting the size distribution of $Q_A(t)$ to be that of a random Pauli string. For large n, N is a Gaussian distribution with mean $\mathcal{S} = 3N/4$ and variance $\delta\mathcal{S}^2 = 3N/16$:

$$P(n) = (3/4)^n (1/4)^{N-n} \approx \frac{1}{\sqrt{2\pi}\delta\mathcal{S}} \exp\left(-(n-\mathcal{S})^2/2\delta\mathcal{S}^2\right). \tag{A17}$$

We therefore have

$$1 - \int_{\mathcal{S}-W_\varepsilon}^{\mathcal{S}+W_\varepsilon} dn\, P(n) = 2\,\mathrm{erfc}\left(\frac{W_\varepsilon}{\sqrt{2}\delta\mathcal{S}}\right) = \varepsilon. \tag{A18}$$

The error function decays exponentially in its argument, so even for exponentially small ε we require only $W_\varepsilon = A\delta\mathcal{S}$ for some constant $A \sim \mathcal{O}(1)$. Setting g equal to its minimal value, $g\mathcal{S}/N = \pi$, we have both $\varepsilon \ll 1$ and $\left|\sin(gW_\varepsilon/N)\right| \approx A\delta\mathcal{S}/\mathcal{S} \sim 1/\sqrt{N} \ll 1$, and so peaked size teleportation is guaranteed.

We can also use this method to guarantee peaked-size teleportation in the large-q SYK model at infinite temperature. Here, the generating function for the size distribution is [24]

$$\sum_n P(n)e^{-\mu n} = \frac{e^{-\mu p}}{(1+(1-e^{-\mu q})\sinh^2 Jt)^{2p/q}} = \sum_n \frac{\Delta_n}{n!}x^n(1-x)^\Delta e^{-\mu(qn+p)} \tag{A19}$$

where we define

$$\Delta_n \equiv \frac{\Gamma(\Delta+n)}{\Gamma(\Delta)}, \quad x \equiv \frac{\sinh^2 Jt}{1+\sinh^2 Jt}, \quad \Delta \equiv 2p/q. \tag{A20}$$

From this, we can identify the size distribution:

$$P(qn+p) = \frac{\Delta_n}{n!}x^n(1-x)^\Delta. \tag{A21}$$

The size and size width are

$$\mathcal{S} = \overline{n} = \sum_n n\frac{\Delta_n}{n!}x^n(1-x)^\Delta = \frac{\Delta x}{1-x}, \qquad \delta\mathcal{S} = \sqrt{\overline{n^2}-\overline{n}^2} = \frac{\sqrt{\Delta x}}{1-x}. \tag{A22}$$

Therefore, the ratio of size width to average size is

$$\delta\mathcal{S}/\mathcal{S} = \sqrt{\frac{x}{\Delta}}\frac{1}{1+x}, \tag{A23}$$

which approaches zero when $p \to \infty$ ($\Delta \to \infty$).

To apply the upper bound Eq. (A16), we need to integrate (i.e. sum) the tail of the size distribution in order to compute its asymptotic width. In this example, the discrete tail can be summed explicitly and we define

$$I(k) \equiv \sum_{n=k}^\infty P(qk+p) = \sum_{n=k}^\infty \frac{\Delta_n}{n!}x^n(1-x)^\Delta = \frac{B_x(k,\Delta)}{B(k,\Delta)} \tag{A24}$$

where $B_x(a,b)$ and $B(a,b)$ are incomplete and ordinary beta function respectively. Let us take $k = \bar{n}(1\pm\eta)$ for some small η representing the asymptotic width

$$W_\varepsilon = \bar{n}\eta q. \tag{A25}$$

This width corresponds to an error

$$\varepsilon = 1 - I(\bar{n}(1-\eta)) + I(\bar{n}(1+\eta)). \tag{A26}$$

Taking $g\mathcal{S}/N = \pi$, the upper bound is

$$\begin{aligned}\mathcal{B} &= 2[1 - I(\bar{n}(1-\eta)) + I(\bar{n}(1+\eta))] + \sin\frac{2\pi\eta x}{1+x} \\ &= 2\left(1 - \frac{B_x(\frac{\Delta x(1-\eta)}{1-x},\Delta)}{B(\frac{\Delta x(1-\eta)}{1-x},\Delta)} + \frac{B_x(\frac{\Delta x(1+\eta)}{1-x},\Delta)}{B(\frac{\Delta x(1+\eta)}{1-x},\Delta)}\right) + \sin\frac{2\pi\eta x}{1+x}.\end{aligned} \tag{A27}$$

At infinite temperature $G_\beta(Q_A) = 1$, we need to show that the minimum of $\mathcal{B}$ tends to zero when $\Delta \to \infty$.

For early time $\sinh Jt \sim \mathcal{O}(1)$, $1-x$ is an order 1 number, and we take $\Delta \to \infty$ limit to get

$$\frac{B_x(\frac{\Delta x(1-\eta)}{1-x},\Delta)}{B(\frac{\Delta x(1-\eta)}{1-x},\Delta)} \to 1, \qquad \frac{B_x(\frac{\Delta x(1+\eta)}{1-x},\Delta)}{B(\frac{\Delta x(1+\eta)}{1-x},\Delta)} \to 0 \tag{A28}$$

The bound becomes

$$\mathcal{B} \to \sin\frac{2\pi\eta x}{1+x} \tag{A29}$$

This basically means that the integrated probability between $\bar{n}(1-\eta)$ and $\bar{n}(1+\eta)$ for any finite η is 1. One can thus take $\eta \to 0$ with speed slower than $1/\Delta \to 0$ in order to have the bound vanish. This computation applies for $x \in (0,1)$, which means that the peaked size always holds for early time. This is physically reasonable as the operator has not yet been scrambled extensively. However, since the size is small at such early times, in order for teleportation to work we must choose $g \sim N$.

For intermediate times, such that $\sinh^2 Jt \sim N$ and $\Delta \ll N \sim 1/(1-x)$, we must take the $x \to 1$ limit first. Using the fact that

$$\frac{B_x(\frac{\Delta x(1-\eta)}{1-x}, \Delta)}{B(\frac{\Delta x(1-\eta)}{1-x}, \Delta)} = 1 - \frac{(1-x)^\Delta x^{\frac{\Delta x(1-\eta)}{1-x}} \Gamma(\frac{\Delta(1-x\eta)}{1-x})}{\Gamma(\frac{\Delta x(1-\eta)}{1-x})\Gamma(1+\Delta)} F(1, \frac{\Delta(1-x\eta)}{1-x}; \Delta+1; 1-x) \tag{A30}$$

where F is Gauss hypergeometric function, in $x \to 1$ limit the right portion of Eq. (A30) tends to

$$F(1, \frac{\Delta(1-x\eta)}{1-x}; \Delta+1; 1-x) \to {}_1F_1(1; \Delta+1; \Delta(1-\eta)) = \Delta^{1-\Delta} e^{\Delta(1-\eta)} (1-\eta)^{-\Delta} (\Gamma(\Delta) - \Gamma(\Delta, \Delta(1-\eta))) \tag{A31}$$

where $\Gamma(x,a)$ is incomplete gamma function. Meanwhile, the left portion of the second term of Eq. (A30) gives

$$\frac{(1-x)^\Delta x^{\frac{\Delta x(1-\eta)}{1-x}} \Gamma(\frac{\Delta(1-x\eta)}{1-x})}{\Gamma(\frac{\Delta x(1-\eta)}{1-x})\Gamma(1+\Delta)} \to \frac{\Delta^\Delta (1-\eta)^\Delta e^{-\Delta(1-\eta)}}{\Gamma(1+\Delta)} \tag{A32}$$

under $x \to 1$. Combining the two, we have

$$\lim_{x\to 1} \frac{B_x(\frac{\Delta x(1-\eta)}{1-x}, \Delta)}{B(\frac{\Delta x(1-\eta)}{1-x}, \Delta)} = \frac{\Gamma(\Delta, \Delta(1-\eta))}{\Gamma(\Delta)}. \tag{A33}$$

It follows that the upper bound is

$$\mathcal{B} = 2\left(1 - \frac{\Gamma(\Delta, \Delta(1-\eta))}{\Gamma(\Delta)} + \frac{\Gamma(\Delta, \Delta(1+\eta))}{\Gamma(\Delta)}\right) + \sin \pi\eta \tag{A34}$$

This function has a unique minimum for $\eta \in [0, 1/2]$ and this minimum decreases as Δ increases. Taking derivative with respect to η, we get

$$\begin{aligned} \partial_\eta \mathcal{B} &= \pi \cos \pi\eta - \frac{2\Delta^\Delta}{\Gamma(\Delta)} \left[(1+\eta)^{\Delta-1} e^{-\Delta(1+\eta)} + (1-\eta)^{\Delta-1} e^{-\Delta(1-\eta)}\right] \\ &\to \pi \cos \pi\eta - \sqrt{\frac{2\Delta}{\pi}} \left[(1+\eta)^{\Delta-1} e^{-\Delta\eta} + (1-\eta)^{\Delta-1} e^{\Delta\eta}\right] \end{aligned} \tag{A35}$$

where in the second step we have taken large Δ limit. Solving $\partial_\eta \mathcal{B} = 0$ in this limit, we find the minimum at

$$\eta \approx \sqrt{\frac{1}{\Delta} \log \frac{8\Delta}{\pi^3}} \to 0 \tag{A36}$$

which in turn gives the limit value of $\mathcal{B}$ to be zero. This proves that at infinite temperature, teleportation exactly matches the peaked-size prediction for both early and intermediate times. For late times $t \gg \frac{1}{2J} \log N$ the size distribution above breaks down, as can be seen since $P(n)$ is dominated by some $n > N$, which is unphysical since N is the total number of fermions.

In contrast, we can also show that the above bound does *not* apply at low temperatures for large-q SYK, as expected from the main text. At low temperature, the upper bound $\mathcal{B}$ needs to be much smaller than the two-sided correlation function $G_\beta(Q_A) \sim (\beta J)^{-2\Delta}$ in order to guarantee peaked-size teleportation. The low temperature size distribution is essentially the same as at infinite temperature, requiring only the replacement

$$x \to \frac{\sinh^2 \pi t/\beta}{(\pi/\beta J)^2 + \sinh^2 \pi t/\beta} \in [0,1] \tag{A37}$$

and adding $e^{-\mu N \delta_\beta}$ to the distribution, which shifts the initial size by a constant amount $N\delta_\beta$ (accounting for the size of the thermal density matrix). Following a similar computation to above, one can show that $\mathcal{B}$ still asymptotes to zero, but now with a *slower* speed than $G_\beta(Q_A)$. For example, in the early time and large Δ limits, $\mathcal{B} \sim \exp(-\Delta C(x,\eta))/\sqrt{\Delta}$ where $C(x,\eta)$ is order 1, while $G_\beta(Q_A) \sim \exp(-2\Delta \log(\beta J))$ is exponentially smaller for large βJ. Therefore, the upper bound $\mathcal{B}$ fails to guarantee peaked-size teleportation. This is consistent with the fact that the correlation function $C_Q(t)$ in Eq. (75) in low temperature is far from being a pure phase.

Appendix B: The Hayden-Preskill recovery protocol

In this Section we review the HPR protocol following Refs. [10, 11] and derive its equivalence to the TW protocol in the case of infinite temperature teleportation of a single qubit. This single-qubit variant of the HPR protocol was experimentally implemented in Ref. [12], although an explicit derivation of its quantum circuit was not provided.

There are two variants of the HPR protocol: a probabilistic variant, which teleports successfully only with some finite probability, and a deterministic variant, which uses an analog of Grover's search algorithm and succeeds with unit probability, but involves a more complex decoding operation. Both protocols take the general form,

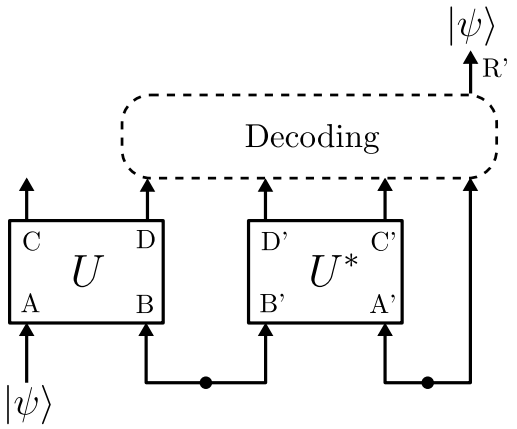

(B1)

shown for teleportation of a quantum state $|\psi\rangle$ (the generalization to EPR teleportation is straightforward). We now outline the interpretation of each aspect of the above protocol in the context of the Hayden-Preskill thought experiment. For consistency with past literature, we have used *different* subsystem labels than introduced in the main text—most notably, subsystem D now denotes the coupled qubits, and subsystem C denotes its complement. Subsystem B represents an eternal black hole that is maximally entangled with its past Hawking radiation subsystem B', as represented by a dimension $d_B = d'_B$ EPR pair between the two subsystems. Subsystem A contains the initial state $|\psi\rangle$ of an observer Alice's diary. Upon falling into the black hole, the diary's information is scrambled by the unitary time-evolution U acting on the left subsystem $l \equiv \text{AB} = \text{CD}$. Far from destroying the information of Alice's diary, scrambling by U in fact allows an outside observer Bob to decode the diary if he has access *any* few qubits of new Hawking radiation D, along with the past Hawking radiation B' and an ancillary EPR pair between A' and R', where $d'_A = d_A$. This decoding relies on OTOCs between subsystem A and D being minimal, a general feature of thermalizing time-evolution after the scrambling time. The decoding begins by applying the conjugate time-evolution U^* to the right system $r \equiv \text{A'B'} = \text{C'D'}$, followed by coupling the black hole and its past radiation with $W = e^{i\pi P_{\text{EPR},D}}$, and finally by time-evolving the right side under U^T and a single-qubit Y gate.

a. Probabilistic decoding: intuition

Although our main focus will be on the deterministic teleportation protocol, we review the probabilistic protocol here for completeness, and as a convenient platform to introduce the intuition connecting operator spreading to the success of teleportation. The decoding operation of the probabilistic HPR protocol consists of projection onto EPR pairs on a subsystems D, D':

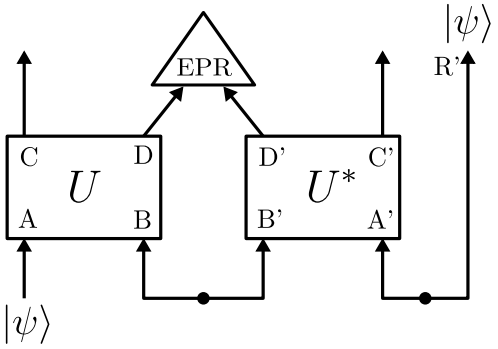

(B2)

Perfect teleportation requires $d_D \geq d_A$, and succeeds with probability $1/d_A^2$ when U is maximal scrambling. The non-unity success probability signifies that the decoding protocol becomes exponentially more complex with the number of qubits to be teleported.

To provide intuition for the protocol's success, we analyze the action of EPR projection on the initial states $Q_{A,l}(t)\,|\mathrm{TFD}\rangle$. We write $Q_A(t)$ as a sum of Pauli strings S on the entire system:

$$Q_A(t) = \sum_R c_R(t) S. \tag{B3}$$

Denoting the EPR projector on subsystems D, D' as $P_{\mathrm{EPR},D}$ and writing each Pauli string as a tensor product $R = R_C \otimes R_D$ of Paulis on subsystems D and C, we have

$$P_{\mathrm{EPR},D} R_l\,|\mathrm{EPR}\rangle = \delta_{R_D,\mathbb{1}} R_l\,|\mathrm{EPR}\rangle\,, \tag{B4}$$

since $\langle \mathrm{EPR}_{D,D'}|\, S_{D,l}\,|\mathrm{EPR}_{D,D'}\rangle = \mathrm{tr}_D(R_D)/d_D = \delta_{R_D,\mathbb{1}}$. Perfect teleportation is achieved when all input Pauli operators on subsystem A have spread to subsystem D, such that every Pauli string S composing $Q_A(t)$ has non-identity support on subsystem D, for all non-identity Q_A. In this situation, the EPR projector has eigenvalue 1 on the thermofield double state and eigenvalue 0 in *all* perturbed states:

$$P_{\mathrm{EPR},D}\,|\mathrm{EPR}\rangle = |\mathrm{EPR}\rangle \quad , \quad P_{\mathrm{EPR},D}\,Q_{A,l}(t)\,|\mathrm{EPR}\rangle = 0. \tag{B5}$$

However, this is no different than projecting onto EPR pairs between subsystems A and A' before time-evolution by $U_l U_r^*$! This projection would, of course, have an action

$$P_{\mathrm{EPR}}\,|\mathrm{EPR}\rangle = |\mathrm{EPR}\rangle \quad , \quad P_{\mathrm{EPR}}\,Q_{A,l}\,|\mathrm{EPR}\rangle = \mathrm{tr}(Q_A) = 0. \tag{B6}$$

Expressed diagrammatically, this equivalence is:

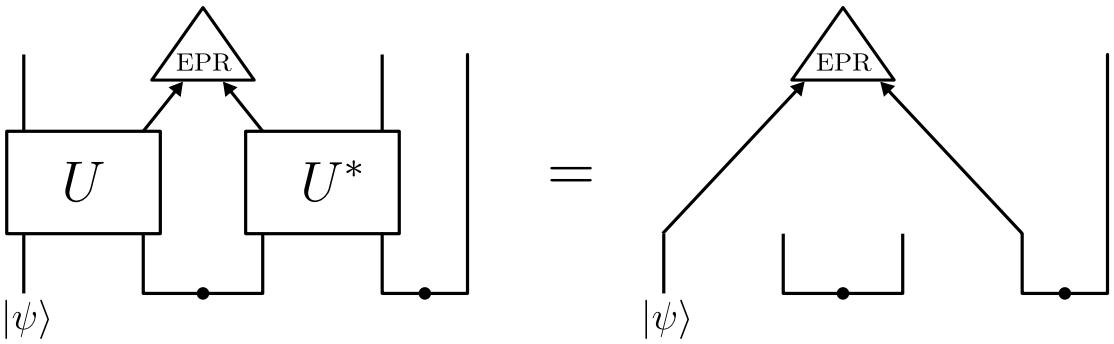

(B7)

for all initial states ψ. However, performing EPR projection between subsystems A, A' before time-evolution is precisely the standard quantum teleportation protocol, applied to subsystems A, A', and R'. The scrambling dynamics of U allow one to perform this teleportation via coupling *any* subsystem D of the system's qubits.

b. Deterministic decoding

After scrambling, the probability of successful EPR projection on subsystem D, $O(1/d_A^2)$, is exponentially small in the size of subsystem A, the state to be teleported. In contrast to standard teleportation, non-successful EPR projection (i.e. projection onto a different maximally entangled state, not $|\mathrm{EPR}_{D,D'}\rangle$) *cannot* be corrected via an additional decoding operation. This exponential decrease in success probability is overcome in the deterministic HPR protocol, which uses an analog of Grover's search algorithm to search for an EPR pair between subsystems D, D'. The protocol requires $O(d_A)$ steps for completion, again exponential in the number of qubits to be teleported (albeit with half the exponent of the probabilistic decoding).

Grover's search algorithm involves two operations: the first applies a minus sign to the state one is searching for, and the second applies a minus sign to the system's initial state. We will search for an EPR pair on subsystem D, so for the first step we apply $W_D \equiv 1 - 2P_{\mathrm{EPR},D} = e^{i\pi P_{\mathrm{EPR},D}}$:

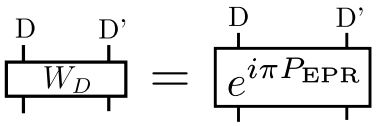

(B8)

In the second step, we flip the sign of the initial state (the time-evolved EPR pair between A' and the reference qubit R') by applying $\widetilde{W}_A \equiv U^* W_A U^T$:

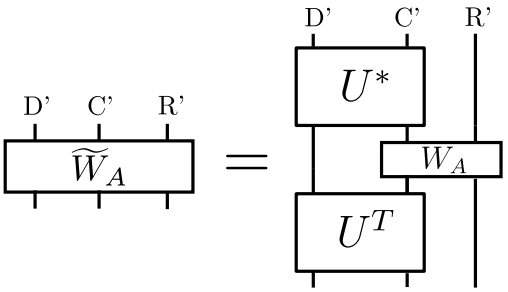

(B9)

where $W_A = 1 - 2P_{\mathrm{EPR},A}$ acts on A', R' to apply a minus sign if the two are in an EPR pair.

The entire Grover protocol is identical to the probabilistic protocol, but with EPR measurement replaced by repeated applications of the two above steps until the EPR pair is found. Displaying, for instance, only the first two iterations:

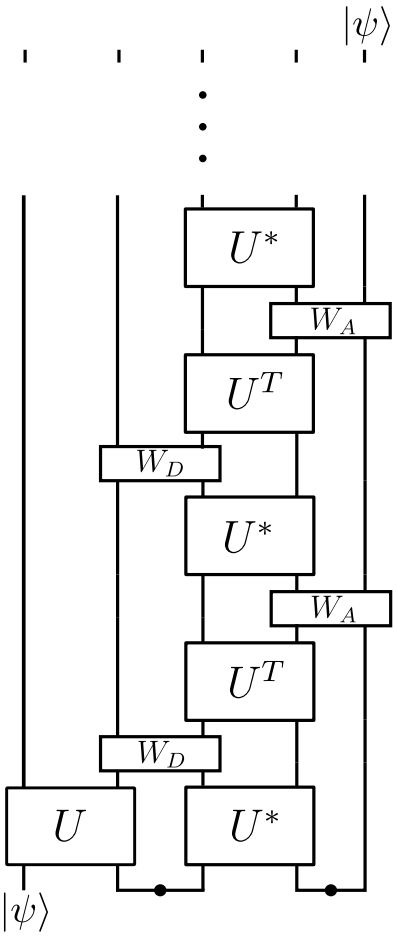

(B10)

After $O(d_A)$ iterations, the state $|\psi\rangle$ is found on subsystem R'.

c. Single qubit deterministic decoding

Two important simplifications occur to the deterministic HPR protocol in the case of single qubit teleportation, $d_A = 2$. The first is that the Grover operator W_A is equal to a SWAP operator composed with single-qubit Y

operations. To see this, we expand W_A in terms of Pauli operators:

$$\begin{aligned} W_A &= 1 - 2P_{\mathrm{EPR},A} \\ &= 1 - \frac{2}{d_A^2} \sum_{P_A} P_{A,l}\, P_{A,r}^* \\ &= \frac{1}{2} - \frac{1}{2} X_l X_r + \frac{1}{2} Y_l Y_r - \frac{1}{2} Z_l Z_r \\ &= \frac{1}{2} Y_l \left[1 + X_l X_r + Y_l Y_r + Z_l Z_r\right] Y_l \\ &= Y_l \left(\mathrm{SWAP}\right) Y_l, \end{aligned} \tag{B11}$$

where we used the Pauli decomposition for the swap operator between two d_A-dimensional boson systems:

$$\mathrm{SWAP} = \frac{1}{d_A} \sum_{P_A} P_{A,l} P_{A,r}^{\dagger}. \tag{B12}$$

Expressed graphically, we have

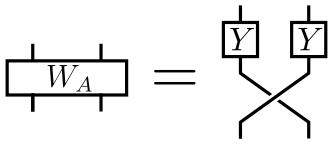

(B13)

The second simplification is that Grover's search for an EPR pair D, D' succeeds after only one step; this is a general result for Grover's search in a $d_D^2 = 4$-dimensional database [62]. It implies that the Grover protocol can teleport one qubit through the circuit:

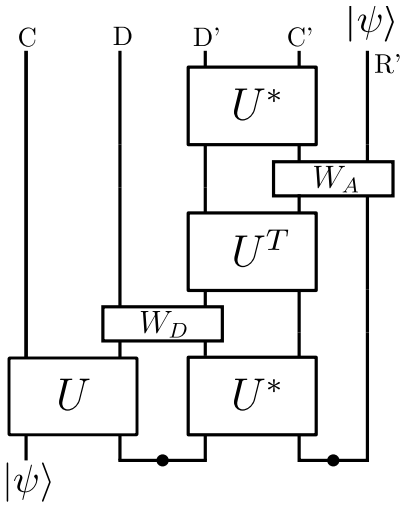

(B14)

If we only care about the fidelity of the teleported state, we can neglect the final application of U^*. Performing the

SWAP gate explicitly, and neglecting the action of the final Y operator on R', we have:

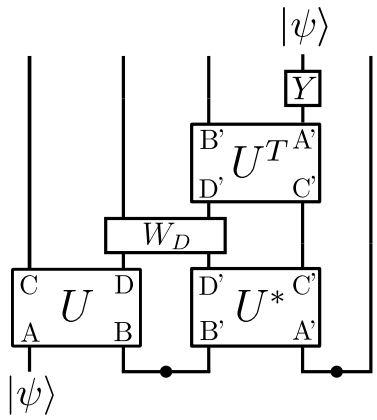

(B15)

This exact circuit has been performed in trapped ion experiment [12]. We now make a small cosmetic adjustment, and move the reference qubit R' from the far right to the far left,

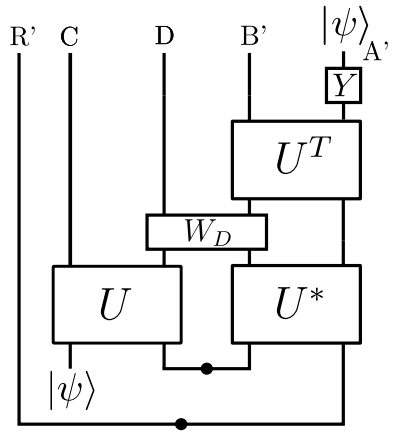

(B16)

Sliding U^* to the left side using Eq. (7), we have:

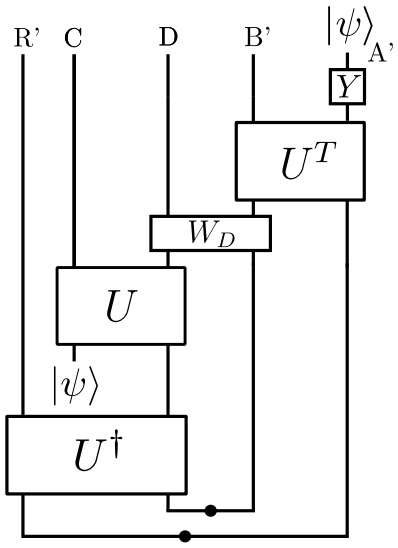

(B17)

This is the same circuit appearing the teleportation protocol of Ref. [14, 15], modulo the precise form of the coupling.

In the case of EPR teleportation, we would instead have

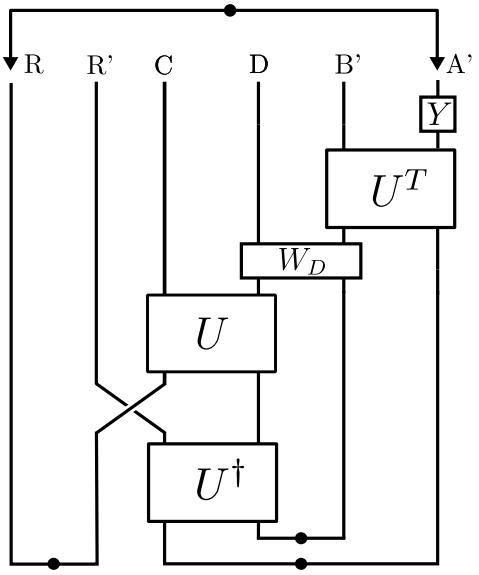

(B18)

where subsystems R' and A' are in an EPR pair when teleportation is successful. This is the circuit appearing in Ref. [16], modulo the form of the coupling as well as the Y decoding operation. The lack of a Y decoding operation for fermionic teleportation is discussed in Appendix F.

Appendix C: State teleportation fidelity

We begin by quickly demonstrating the relation between the correlator of the time-evolved operator $|\psi\rangle\langle\phi|$ and the success of state teleportation. We do so by inserting the resolution of the identity $\frac{1}{d_A}\sum_{|\phi\rangle}|\phi\rangle\langle\phi| = \mathbb{1}$ into the ancillary qubit leg of the diagram for the state teleportation fidelity. We find:

$$F_\psi =$$

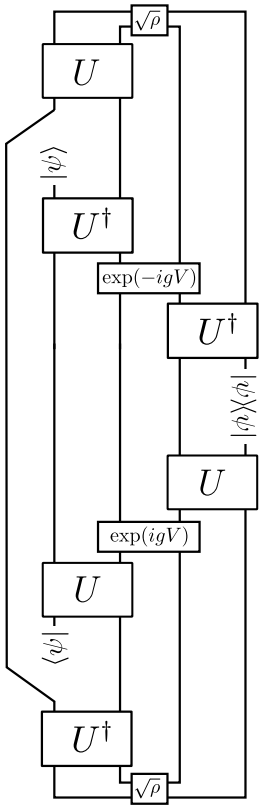

$$= \frac{1}{d_A}\sum_{|\phi\rangle}$$

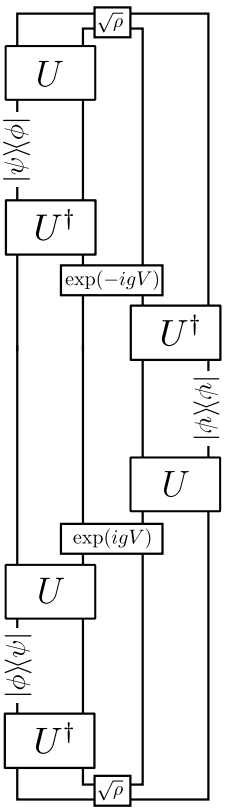

(C1)

Plugging Eq. (10) into this diagram clearly provides unit teleportation fidelity. When teleportation is successful each of the d_A terms of the sum must succeed individually, so the right input state $|\phi\rangle$ will not affect the success of the teleportation.

As with EPR distillation, we can relate the state teleportation fidelity to correlators of Pauli operators by decomposing the SWAP operator. Diagramatically,

$F_\psi =$ 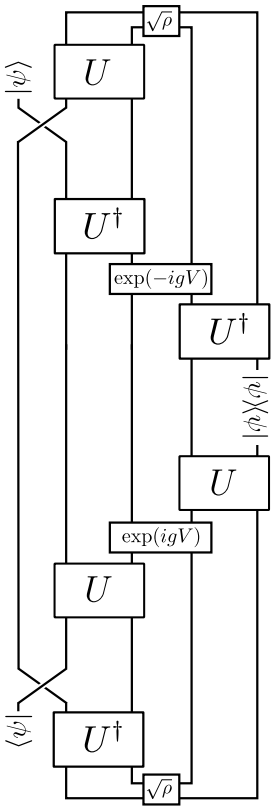 $=$ $\frac{1}{d_A^2}\sum_{P_1,P_2}$ 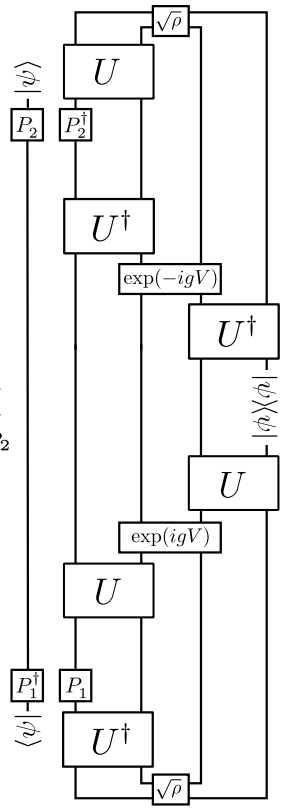 (C2)

and in equation form,

$$F_\psi = \frac{1}{d_A^2}\sum_{P_1,P_2}\langle\psi|\,P_2^\dagger P_1^\dagger\,|\psi\rangle\cdot\langle\mathrm{TFD}|\,P_{2,l}(t)e^{-igV}\,|\psi\rangle\langle\psi|_r(-t)\;e^{igV}P_{1,l}(t)\,|\mathrm{TFD}\rangle\,. \tag{C3}$$

When the correlators are maximal with phases $e^{i\theta_P}$, we can simplify this expression as

$$\begin{aligned}
F_\psi &\approx \frac{1}{d_A^2}\sum_{P_1,P_2}\langle\psi|\,P_2^\dagger P_1^\dagger\,|\psi\rangle\cdot\langle\mathrm{TFD}|\,P_{2,r}(-t)\,|\psi\rangle\langle\psi|_r(-t)\;P_{1,r}(-t)\,|\mathrm{TFD}\rangle \\
&= \frac{1}{d_A^2}\sum_{P_1,P_2}e^{i(\theta_{P_1}-\theta_{P_2})}\cdot\langle\psi|\,P_2^\dagger P_1^\dagger\,|\psi\rangle\cdot\mathrm{tr}\left(\rho\,P_2\,|\psi\rangle\langle\psi|\,P_1\right) \\
&= \frac{1}{d_A^2}\sum_{P_1,P_2}e^{i(\theta_{P_1}-\theta_{P_2})}\cdot\mathrm{tr}\left(P_1^\dagger\,|\psi\rangle\langle\psi|\,P_2^\dagger\right)\cdot\mathrm{tr}\left(\rho\,P_2\,|\psi\rangle\langle\psi|\,P_1\right).
\end{aligned} \tag{C4}$$

As expected, when the phases $e^{i\theta_P}$ are the same for all operators, this gives unit fidelity:

$$\begin{aligned}
F_\psi &= \frac{1}{d_A^2}\sum_{P_1,P_2}\mathrm{tr}\Big(P_1^\dagger\,|\psi\rangle\langle\psi|\,P_2^\dagger\Big)\cdot\mathrm{tr}(\rho\,P_2\,|\psi\rangle\langle\psi|\,P_1) \\
&= \frac{1}{d_A}\sum_{P_1}\mathrm{tr}\Big(P_1^\dagger\,|\psi\rangle\langle\psi|\,|\psi\rangle\langle\psi|\,P_1\rho\Big) \\
&= \mathrm{tr}(|\psi\rangle\langle\psi|)\,\mathrm{tr}(\rho) \\
&= 1,
\end{aligned} \tag{C5}$$

using properties of Pauli operators as a 1-design. Differing phases $e^{i\theta_P}$ cause the terms in the sum to interfere with each other, giving lower fidelity. At finite temperature, the fidelity of peaked-size teleportation is again limited. For instance, if $|\psi\rangle$ is a single-qubit eigenstate of the Pauli Z operator, we have:

$$\begin{aligned} F_{\text{EPR}} &= \frac{1}{2^2}\sum_{P_1,P_2}\langle\psi|\,P_2P_1\,|\psi\rangle\cdot\langle\text{TFD}|\,P_{2,l}(t)e^{-igV}[Y\,|\psi\rangle\langle\psi|Y]_r(-t)\;e^{igV}P_{1,l}(t)\,|\text{TFD}\rangle \\ &= \frac{1}{2^2}\sum_{P_1,P_2}\langle\psi|\,P_2P_1\,|\psi\rangle\cdot\text{tr}\Big(|\psi\rangle\langle\psi|\;\rho^{1/2}P_2P_1\rho^{1/2}\Big) \\ &= \sum_{P}\langle\psi|\,P\,|\psi\rangle\cdot\text{tr}\Big(|\psi\rangle\langle\psi|\;\rho^{1/2}P\rho^{1/2}\Big) \\ &= 2\,\text{tr}\Big(|\psi\rangle\langle\psi|\;\rho^{1/2}\,|\psi\rangle\langle\psi|\,\rho^{1/2}\Big) \\ &\approx \frac{1}{2}\,\text{tr}\Big((\mathbb{1}+Z)\,\rho^{1/2}(\mathbb{1}+Z)\rho^{1/2}\Big) \\ &\approx \frac{1}{2}+\frac{1}{2}G(t'-t+i\beta/2)+\langle Z\rangle_\beta\,, \end{aligned} \tag{C6}$$

where $\langle Z\rangle_\beta = \text{tr}(Z\rho)$, which averages to zero for different initial states $|\psi\rangle$.

1. Rydberg simulations

For numerical or experimental simulations, it is often convenient to measure teleportation state fidelity rather than EPR fidelity to avoid the inclusion of ancilla qubits. We followed this approach for the Rydberg numerics presented in Fig. 6. In particular, we utilized the one-sided protocol shown in Fig. 5(b) except with EPR measurement replaced by measurement of a two-qubit state $|\psi\rangle\otimes|\psi^*\rangle$. To compute the average state fidelity, we simulated the protocol for all single-qubit states in a 2-design, i.e. $|\psi\rangle\in\{|0\rangle\,,|1\rangle\,,|0\rangle\pm|1\rangle\,,|0\rangle\pm i\,|1\rangle\}$. In addition, we sampled uniformly over ~ 100 initial states in the computational basis to account for the K 'measured' and $N-K$ 'unmeasured' qubits. Time evolution was performed using Krylov subspace methods, which are amenable to parallelization and generally more efficient than exact diagonalization [76].

Additional results showing finite-size effects on the fidelity are shown in Fig. 8. We observe that the fidelity generally increases for larger systems but decreases for larger values of g. This is consistent with our error analysis, where we showed that the error scales $g^2\delta S^2/N^2$. In particular, at late times, we expect the size distribution to approach a binomial and the error to scale as g^2/N. Finally, let us comment on the crossing of the curves observed in Fig. 8(a). At early times, smaller systems acquire a larger phase because the phase scales as $g\mathcal{S}/N$, where g and $\mathcal{S}$ are independent of size; however, at late times, larger systems saturate to a higher fidelity due to their narrower size distributions, i.e. $\delta\mathcal{S}/\mathcal{S}\sim 1/\sqrt{N}$. Thus, the curves intersect near the scrambling time as they transition between these two regimes.

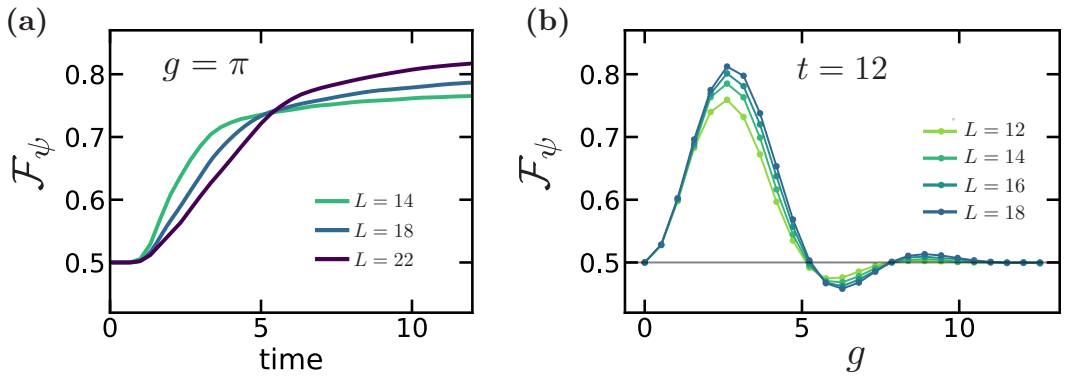

Figure 8. Finite-size scaling of the Rydberg simulations **(a)** as a function of time with $g=\pi$, and **(b)** as a function of coupling strength g with $t=12$. The system was evolved under the Rydberg Hamiltonian, Eq. (93), with the same system parameters as in Fig. 6. We observe the maximum fidelity increase at larger systems, owing to the narrowing of the size distribution.

Appendix D: Random unitary circuit numerics

Here we provide additional details and numerical data from our random unitary circuit simulations.

1. Algorithm

As discussed in the main text, our approach relies on the fact that the EPR fidelity is simulable using a unitary 3-design. Thus, we can replace each Haar-random gate in the circuit with a random *Clifford* gate, whose action on a Pauli operator can be efficiently simulated with a classical computer. More specifically, our algorithm consists of the following three ingredients. First, following a standard approach, we represent an n-qubit Pauli operators as a binary string $v = x_1 x_2 \cdots x_n z_1 z_2 \cdots z_n$ of length $2n$:

$$Q = \prod_{i=1}^{n} Q_i(x_i, z_i) \tag{D1}$$

where $Q_i(0,0) = I_i$, $Q_i(1,0) = X_i$, $Q_i(0,1) = Z_i$, and $Q_i(1,1) = Y_i$ denote individual Pauli operators within the Pauli string. Note that, for our purposes, the overall phase of Q is irrelevant.

Second, we consider circuits composed of random 2-qubit Clifford unitaries, whose layout depends on the dimension. Each of the 2-qubit unitaries is sampled uniformly from the set of 2-qubit Clifford unitaries. While efficient procedures exist to perform this sampling directly, in practice it is sufficient to pre-compute and enumerate the entire 2-qubit set (consisting of 11520 unitaries). Acting a 2-qubit unitary on a Pauli operator corresponds to applying a map to the relevant components of v, e.g. a unitary with support on the jth and kth qubits updates the values of (x_j, z_j, x_k, z_k).

Third, for a given circuit U, we calculate the EPR fidelity using [Eq. (36)]:

$$F_{\text{EPR}} = \left| \frac{1}{d_A^2} \sum_{Q_A} e^{i\theta_{Q_A}} \right|^2 \tag{D2}$$

where

$$\theta_{Q_A} = g\mathcal{S}_K[UQ_AU^\dagger]/K + \pi\mathcal{S}[Q_A]. \tag{D3}$$

This amounts to determining the size of Pauli operators after evolving under the Clifford circuit. When A consists of a few qubits, we iterate over all Pauli operators Q_A explicitly; otherwise we compute the sum for ~ 100 randomly selected operators. To compute the average EPR fidelity, we sample ~ 100 realizations of U.

The time complexity of computing the EPR fidelity scales linearly with the number of 2-qubit gates in the circuit and does not otherwise depend on the number of qubits n. This is in contrast to most other observables in the context of Clifford circuits, which require one to compute the evolution of n distinct operators (the stabilizer generators). It is therefore feasible to simulate individual realizations of up to 10^8 qubits within a day on standard single-core processors. Moreover, upon determining the distribution of sizes for a particular operator in a particular circuit, we can compute the teleportation fidelity for arbitrary values of g with no additional computational cost.

2. Extended data for 1D and 2D RUCs

Size distribution— The average size and size width for time-evolved operators in 1D and 2D are shown in Fig. 9. These results match the functional forms predicted by the KPZ universality class [Eq. (47) and (48)] and allows us to extract $\{\alpha_{\text{bulk}}, \alpha_{\text{boundary}}, \beta_{\text{bulk}}, \beta_{\text{boundary}}\} = \{0.47, 0.18, 1.2, 4.5\}$.

Multiple qubits— In Fig. 10, we show the many-body fidelity for teleporting multiple qubits that are evenly spaced in 1D. At early times ($t < 1300$), the light cones of the time-evolved operators do not overlap and the system factorizes into n independent channels, allowing for high fidelity multi-qubit teleportation. At later times, the sizes of the time-evolved operators begin to overlap and, as anticipated from our arguments on size addition, the teleportation fidelity becomes highly suppressed. We note, however, one exception: when only adjacent light cones have overlapped (i.e. $1300 < t < 2600$), we observe order-one fidelities for certain values of g. This occurs whenever the multi-qubit size is a multiple of $2\pi K/g$ off from the size addition value, e.g. $\mathcal{S}[Q_1(t)Q_2(t)] = \mathcal{S}[Q_1(t)] + \mathcal{S}[Q_1(t)] - 2\pi m(K/g)$, where m is an integer value. Therefore, strictly speaking, it is possible to satisfy the conditions for many-body teleportation without size addition; nevertheless, it is a non-generic effect that requires finely tuned values of g and evenly spaced input qubits.

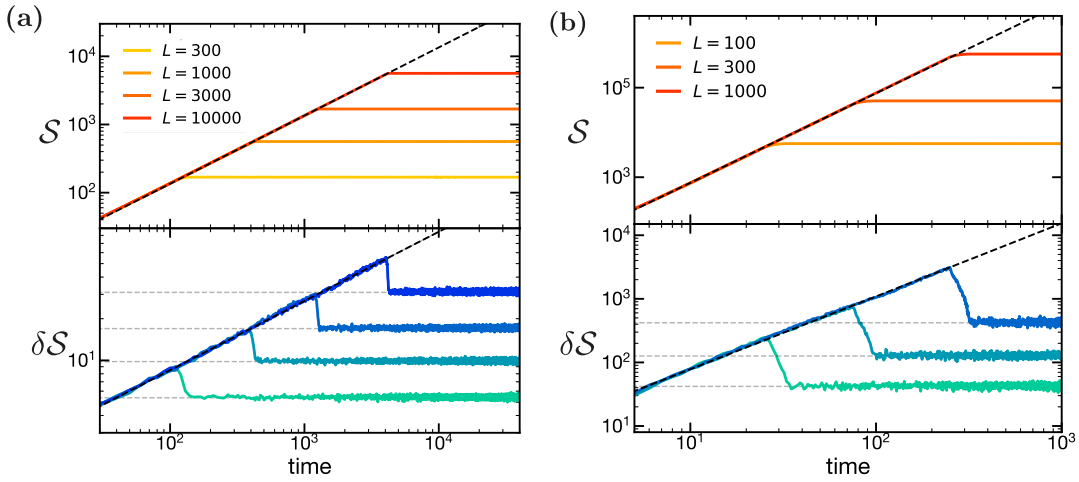

Figure 9. Extended data for average operator size and size width in 1D **(a)** and 2D **(b)** RUCs. The average size grows ballistically $\sim t^d$ (dashed line) and saturates at $t_{\rm scr} \sim L \sim N^{1/d}$. The size width matches the predictions from the KPZ universality class (dashed lines) and allows us to extract the prefactors in Eq. (47) and (48). In particular, we determine $\alpha_{\rm bulk}$ and $\beta_{\rm bulk}$ from the saturation values (light gray), and $\alpha_{\rm boundary}$ and $\beta_{\rm boundary}$ from the initial growth rate (dark gray).

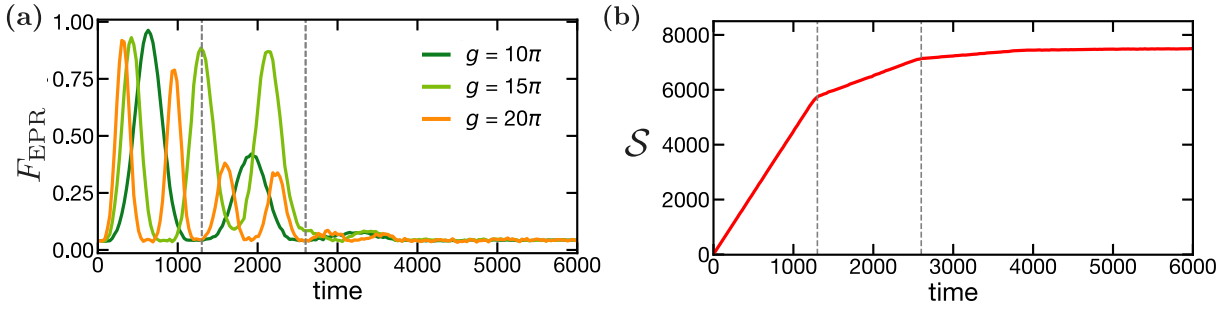

Figure 10. Teleporting multiple qubits ($n = 5$) in 1D. **(a)** Teleportation is achieved with high fidelity for $t \leq 1300$; this corresponds to the regime in which the light cones of the operators are non-overlapping, as indicated by the average operator size **(b)**. Surprisingly, order-one fidelity can also occur for $1300 < t < 2600$ (when adjacent light cones have overlapped) but only for certain values of g.

3. Channel capacity for 0D RUCs

The channel capacity corresponds to maximum number of qubits that can be teleported with a fixed *fidelity per qubit*. One way to estimate this would be to take the n-th root of the many-body EPR fidelity; however, in practice, this approach is numerically unstable for large n. Instead, we consider a modified protocol where one only measures the fidelity of one of the n teleported qubits, and neglects the state of the unmeasured qubits. At infinite temperature, this fidelity is computed by:

$$\begin{aligned} F^m_{\rm EPR} &= \frac{1}{d_A^4} \sum_{Q_1,Q_2} \langle {\rm TFD}|\, Q^\dagger_{2,l}(t)\, e^{-igV}\, \tilde{Q}^m_{2,r}(-t) \tilde{Q}^{m\dagger}_{1,r}(-t)\, e^{igV}\, Q_{1,l}(t)\, |{\rm TFD}\rangle \cdot {\rm tr}\Big(Q_1^{u\dagger} Q_2^u\Big) \\ &= \frac{1}{d_m^4 d_u^2} \sum_{Q_1,Q_2} e^{i(\theta_{Q_1}-\theta_{Q_2})} \delta_{Q_1^u,Q_2^u} \end{aligned} \tag{D4}$$

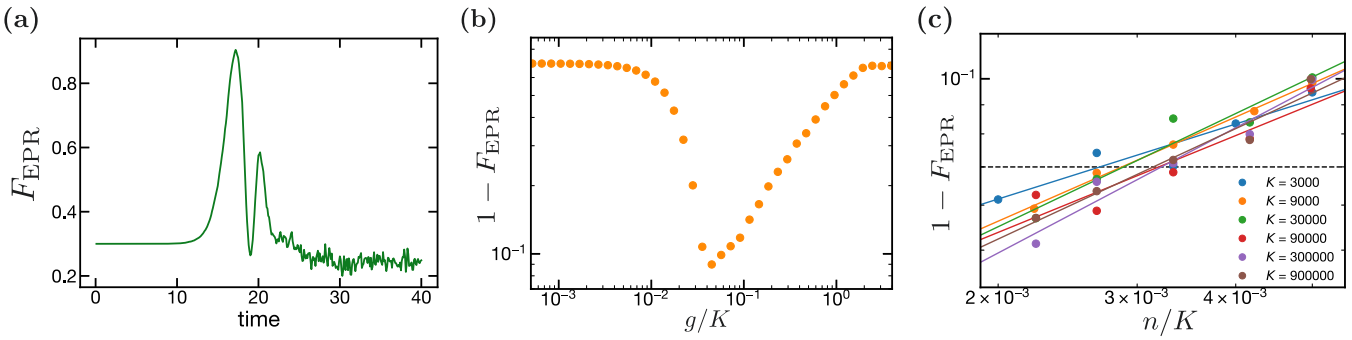

Figure 11. Procedure for determining the channel capacity in 0D RUCs. **(a-b)** For each n and K, we compute the optimal fidelity as a function of (a) the evolution time and (b) coupling strength g. Typical data are shown for $n = 38$ and $K = 9000$. **(c)** By fitting the optimal fidelity as function of n with a linear fit in log space, we determine the maximum number of qubits that can be teleported within a threshold fidelity, i.e. $1 - F \leq 0.07$ (dashed line). The intercepts approximately collapse with respect to n/K, indicating that the channel capacity is linear in K.

where $Q = Q^m \otimes Q^u$ and $d_A = d_m d_u$, such that Q^m acts on the measured qubit, and Q^u acts on the unmeasured qubits. This can be derived diagrammatically via

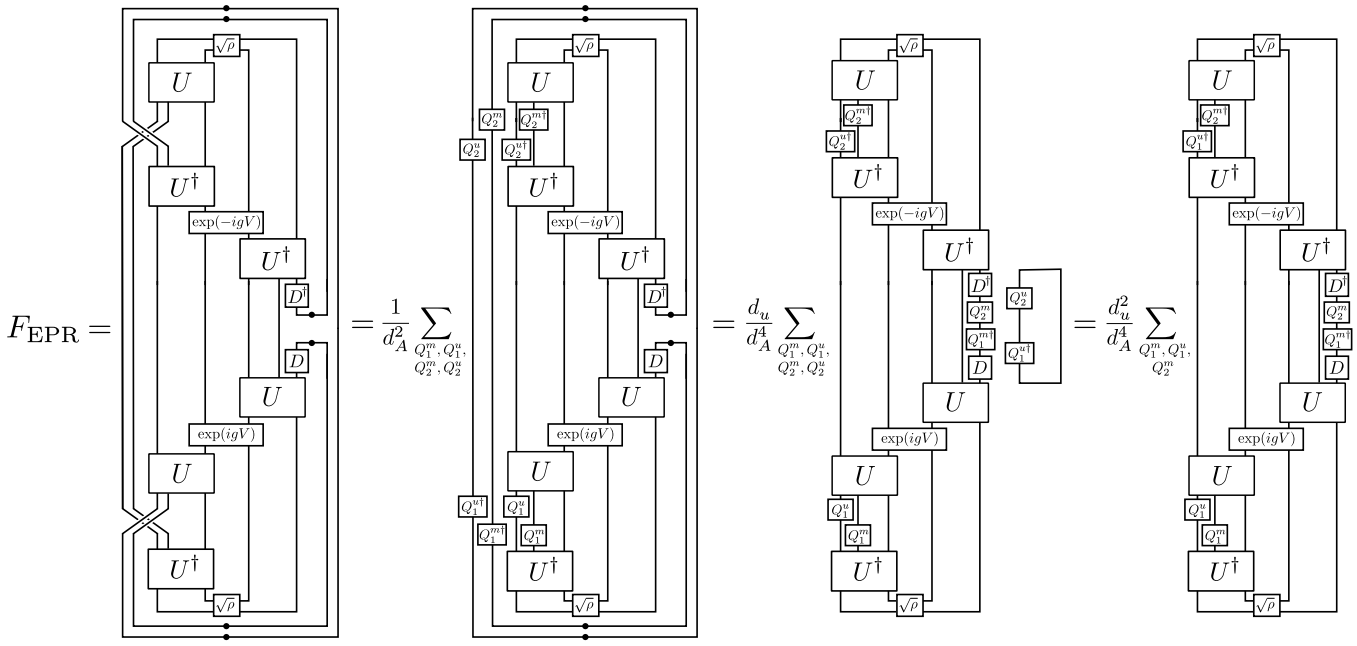

(D5)

We see that computing this fidelity is nearly identical to computing the full many-body fidelity, except we sample only over pairs of Pauli operators (Q_1, Q_2) which are identical on every qubit except for the first.

Our procedure for determining the channel capacity is shown in Fig. 11. First, we maximize the fidelity with respect to the evolution time t and the coupling strength g: the maximum fidelity occurs during the first peak of its time profile, and is non-monotonic with respect to g. Next, we vary the number of input qubits n (for fixed number of coupled qubits K) and calculate the point at which the fidelity exceeds a threshold value $1 - F \geq 0.07$. Our results from this procedure demonstrate that the channel capacity follows a linear trend in K across two orders of magnitude, in agreement with our analytical predictions.

Appendix E: Random circuit calculations

Here we provide more detailed calculations of the size overlap and K-size distribution of random Pauli operators of a fixed size. The former is relevant to 0D RUCs, as the vanishingly small overlap of random Pauli strings with size

much less than the system size underlies the circuit's ability to teleport multiple qubits at intermediate times. The latter is applicable to all systems when the K coupled qubits are chosen randomly, and quantifies the width introduced to the K-size by this random sampling. In the appropriate limits, these calculations reproduce the intuitive binomial scalings we argued for in the main text.

1. Distribution of the overlap of two random Pauli strings

Our primary result is a calculation of the probability distribution of the overlap p of two randomly sampled Pauli strings of fixed length R_1, R_2, in a system of N qubits. This probability is computed exactly from various factorials:

$$P[p] = \frac{C_p^N C_{R_1-p}^{N-p} C_{R_2-p}^{N-R_1}}{C_{R_1}^N C_{R_2}^N} = \frac{1}{p!}\frac{R_1!}{(R_1-p)!}\frac{R_2!}{(R_2-p)!}\frac{(N-R_1)!(N-R_2)!}{N!(N-R_1-R_2+p)!} \tag{E1}$$

The numerator computes the number of distinct configurations with Pauli strings of size R_1, R_2 and overlap p, while the denominator computes the number of distinct Pauli strings of size R_1, R_2 regardless of the overlap. We are interested in the case where all variables are extensive (scale with N), but $N \gg R_1, R_2 \gg p$. We will proceed by applying Stirling's approximation to each term above, which holds as long as all quantities are large compared to 1. For instance, for dummy variables n, k, we have:

$$\frac{n!}{(n-k)!} \approx \sqrt{\frac{n}{n-k}}\frac{n^n}{(n-k)^{n-k}}e^{-k} = n^k\left(1-\frac{k}{n}\right)^{-n+k-1/2}e^{-k} \tag{E2}$$

or, taking the logarithm,

$$\log\frac{n!}{(n-k)!} \approx k\log(n) - \left(n-k+\frac{1}{2}\right)\log\left(1-\frac{k}{n}\right) - k. \tag{E3}$$

We will apply this to a few pairs of factorials in our original expression for $P[p]$. For convenience, we only keep track of the p-dependence of the probability, and neglect overall constants which serve to normalize the distribution. Anticipating that the average p will be R_1R_2/N, we expand $p = R_1R_2/N + \delta$ and work to second order in δ. At the end we will show that this is justified. We have:

$$\log\frac{R_1!}{(R_1-p)!} \approx p\log(R_1) - \left(R_1 - \frac{R_1R_2}{N} + \frac{1}{2}\right)\log\left(1-\frac{R_2}{N}-\frac{\delta}{R_1}\right) - \frac{R_1R_2}{N} - \delta \tag{E4}$$

Expanding the logarithm using

$$\log(1-y-x) \approx \log(1-y) - \frac{x}{1-y} - \frac{1}{2}\frac{x^2}{(1-y)^2} + O(x^3) \tag{E5}$$

we have

$$\begin{aligned}\log\frac{R_1!}{(R_1-p)!} &\approx p\log(R_1) - \left(R_1 - \frac{R_1R_2}{N} - \delta + \frac{1}{2}\right)\left[\log\left(1-\frac{R_2}{N}\right) - \frac{\delta/R_1}{1-R_2/N} - \frac{(\delta/R_1)^2}{(1-R_2/N)^2}\right] - \delta + \dots \\ &\approx p\log(R_1) + \delta\log\left(1-\frac{R_2}{N}\right) - \frac{1}{2}\delta^2\left[\frac{1}{R_1}\frac{1}{1-R_2/N}\right] + O(\delta/R) + O(\delta^3/R^2) + \dots.\end{aligned} \tag{E6}$$

This gives

$$\begin{aligned}\log\frac{R_1!}{(R_1-p)!}\frac{R_2!}{(R_2-p)!} \approx p\log(R_1R_2) + \delta\log\left((1-\frac{R_2}{N})(1-\frac{R_1}{N})\right) - \frac{1}{2}\delta^2\left[\frac{1}{R_1}\frac{1}{1-R_2/N} + \frac{1}{R_2}\frac{1}{1-R_1/N}\right] \\ + O(\delta/R) + O(\delta^3/R^2) + \dots.\end{aligned} \tag{E7}$$

The last piece is

$$\begin{aligned}\log\frac{N!}{(N-R_1-R_2+p)!} &\approx -p\log(N) - \left(N-R_1-R_2+\frac{R_1R_2}{N}+\delta+\frac{1}{2}\right)\log\left(1-\frac{R_1}{N}-\frac{R_2}{N}+\frac{R_1R_2}{N^2}+\frac{\delta}{N}\right)+\delta+\dots \\ &\approx -p\log(N) - \left(N-R_1-R_2+\frac{R_1R_2}{N}+\delta+\frac{1}{2}\right)\times \\ &\quad\left[\log\left((1-\frac{R_1}{N})(1-\frac{R_2}{N})\right)+\frac{\delta/N}{(1-\frac{R_1}{N})(1-\frac{R_2}{N})}-\frac{\delta^2/N^2}{(1-\frac{R_1}{N})^2(1-\frac{R_2}{N})^2}\right]+\delta+\dots \\ &\approx -p\log(N)-\delta\left[\log\left((1-\frac{R_1}{N})(1-\frac{R_2}{N})\right)\right]-\frac{1}{2}\delta^2\left[\frac{1}{N}\frac{1}{(1-R_1/N)(1-R_2/N)}\right]+ \\ &\quad O(\delta/N)+O(\delta^3/N^2)\end{aligned} \tag{E8}$$

Combining these together, we have

$$\begin{aligned}\log P[p] \approx &-\log(p!)+p\log\left(\frac{R_1R_2}{N}\right)- \\ &\frac{1}{2}\delta^2\left[\frac{1}{R_1}\frac{1}{1-R_2/N}+\frac{1}{R_2}\frac{1}{1-R_1/N}+\frac{1}{N}\frac{1}{(1-R_1/N)(1-R_2/N)}\right]+O(\delta/R)+O(\delta^3/R^2).\end{aligned} \tag{E9}$$

Exponentiating,

$$P[p]\approx\frac{1}{p!}\left(\frac{R_1R_2}{N}\right)^p\exp\left(-\frac{1}{2}\left(p-\frac{R_1R_2}{N}\right)^2\left[\frac{R_1R_2}{R_1+R_2}+O(1/N)\right]^{-1}+O(\delta/R)+O(\delta^3/R^2)\right). \tag{E10}$$

The first two terms are precisely a Poisson distribution, which has mean R_1R_2/N and width $\sqrt{R_1R_2/N}$. The exponential is a Gaussian with the same mean R_1R_2/N, and a larger width $\sqrt{R_1R_2/(R_1+R_2)}$. The smaller width determines the width of the product of the two functions, so we conclude:

$$\langle p\rangle=\frac{R_1R_2}{N},\qquad \langle p^2\rangle-\langle p\rangle^2\approx\frac{R_1R_2}{N}. \tag{E11}$$

This is what we would expect for drawing p random sites out of N, where each site has independent probability R_i/N of being in either Pauli string. The width is subextensive, $\delta\sim\varepsilon\sqrt{N}$, justifying the higher order terms we neglected along the way.

2. Distribution of the K-size

Here we consider the distribution of the K-size for a random Pauli string of fixed total size $\mathcal{S}$. This is in fact an identical problem to calculating the overlap: the K-size is the overlap of the K coupled qubits with the $\mathcal{S}$ qubits acted on by the operator of interest. We should just replace $R_1\to K$, $R_2\to\mathcal{S}$, $p\to n$ above, where n is the K-size. This is confirmed by comparing the factorial expressions:

$$P[n]=\frac{C_n^{\mathcal{S}}C_{K-n}^{N-\mathcal{S}}}{C_K^N}=\frac{1}{n!}\frac{\mathcal{S}!}{(\mathcal{S}-n)!}\frac{K!}{(K-n)!}\frac{(N-\mathcal{S})!(N-K)!}{N!(N-\mathcal{S}-K+n)!} \tag{E12}$$

where the numerator computes the number of distinct configurations with n qubits overlapping the Pauli operator support of size $\mathcal{S}$ and $K-n$ qubits not overlapping, and the denominator computes the number of distinct configurations of the K coupled qubits. There are two regimes of interest: when K and $\mathcal{S}$ are both extensive, and when $\mathcal{S}$ is extensive but K is not. The former provides a more accurate measure of the full operator size ($K\to N$), while the latter is relevant for probing the channel capacity. Both regimes share the same mean K-size $\mathcal{S}_K$ and K-size width $\delta\mathcal{S}_K$:

$$\mathcal{S}_K\equiv\langle n\rangle=\frac{\mathcal{S}K}{N},\qquad \delta\mathcal{S}_K^2\equiv\langle n^2\rangle-\langle n\rangle^2\approx\frac{\mathcal{S}K}{N}=\mathcal{S}_K. \tag{E13}$$

This matches our prediction in the main text, which was based on a simple scenario of picking K sites, each with a $\mathcal{S}/N$ chance of being in the support of the Pauli operator.

Appendix F: Teleportation of fermions

Here we generalize the teleportation protocol to Majorana fermion systems, as discussed in the main text for the SYK model. This involves a few small modifications, stemming from (*i*) a different definition of fermionic EPR (FEPR) pairs, (*ii*) a different relation between FEPR projector and the SWAP gate, and (*iii*) modified expectations for operator spreading in Majorana systems such as SYK.

Consider two complex fermions χ_l and χ_r, decomposed into pairs of Majorana fermions via $\chi_l = \psi_l^1 + i\psi_l^2$, $\chi_r = \psi_r^1 + i\psi_r^2$. The number operators of the original fermions are Majorana bilinears, e.g. $i\psi_l^1\psi_l^2 = 2\hat{N}_l - 1 = (-1)^{\hat{N}_l}$. We define a single FEPR pair as the positive eigenstate of $i\psi_l^1\psi_r^1$ and $i\psi_l^2\psi_r^2$. In the number operator basis of the original complex fermions, this is the maximally entangled state $(|10\rangle - i\,|01\rangle)/\sqrt{2}$. Multiple fermion EPR pairs are formed as a tensor product of single FEPR pairs.

This definition leads to some simple relations when 'sliding' fermion operators around FEPR bras and kets in diagrammatic calculations. We have:

$$\begin{aligned} \psi_l^j\,|\mathrm{FEPR}\rangle &= i\psi_r^j\,|\mathrm{FEPR}\rangle \\ \langle\mathrm{FEPR}|\,\psi_l^j &= -i\,\langle\mathrm{FEPR}|\,\psi_r^j, \end{aligned} \tag{F1}$$

diagrammatically,

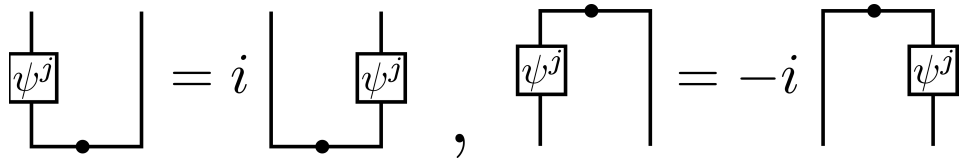

(F2)

As in bosonic systems, the thermofield double state is obtained by applying $\rho^{1/2}$ to one side, $|\mathrm{TFD}\rangle = \rho_l^{1/2}\,|\mathrm{FEPR}\rangle$. Since the SYK Hamiltonian is composed of 4-fermion terms, we have

$$H_l\,|\mathrm{TFD}\rangle = (i)^4 H_r\,|\mathrm{TFD}\rangle = H_r\,|\mathrm{TFD}\rangle\,. \tag{F3}$$

As in bosonic systems, the coupling for Majorana systems [Eq. (59)] measures the size of Majorana strings.

There are two options teleportation in fermionic system. First, we could teleport an ordinary bosonic qubit by encoding it into Majorana fermion operators, for instance:

$$\begin{aligned} X &\equiv i\psi_1\psi_2 \\ Y &\equiv i\psi_2\psi_3 \\ Z &\equiv i\psi_1\psi_3. \end{aligned} \tag{F4}$$

At infinite temperature before coupling, each of the above operators has a correlator equal to -1, which is exactly the result for bosonic systems, but without a need for the decoding operation Y. At late times, the coupling e^{igV} applies a relative phase between the identity and non-identity Paulis, giving correlator phases:

$\mathbb{1}$	$e^{ig\langle V\rangle}$
$i\psi_1\psi_2$	-1
$i\psi_2\psi_3$	-1
$i\psi_1\psi_3$	-1

When $g\,\langle V\rangle = \pi$ all correlators have the same phase, and peaked-size teleportation succeeds with perfect fidelity at infinite temperature. At intermediate times, peaked-size teleportation of multiple bosonic qubits will succeed just as in bosonic systems.

The second option is to send a fermionic qubit, for instance by inserting half of an ancillary FEPR pair. Here we begin with intermediate times, and discuss a modification necessary for late time teleportation afterwards. We represent a single complex fermion with two Majorana operators ψ_1, ψ_2, and suppose that the operators' size distributions are tightly peaked, and the size of $i\psi_1\psi_2$ is twice that of the individual Majorana sizes, denoted $\mathcal{S}$ (this assumption of size addition is appropriate in all-to-all coupled systems, e.g. SYK, but would not necessarily hold for e.g. a 1D Majorana chain). The relevant operator correlators after coupling are:

$\mathbb{1}$	1
ψ_1	$-i \cdot e^{ig\mathcal{S}}$
ψ_2	$-i \cdot e^{ig\mathcal{S}}$
$i\psi_1\psi_2$	$-1 \cdot e^{ig2\mathcal{S}}$

At $g\mathcal{S} = \pi/2$ we have perfect teleportation. This generalizes straightforwardly to multiple fermionic qubits: a p-fermion operator will gain a phase i^p from sliding across the FEPR pair, and a phase $e^{igp\mathcal{S}}$ from coupling.

At late times, the sizes of initial single-body and two-body Majorana operators are equal, since they have saturated the size of the system, and the above operator correlators do not have the same phase. We now show that an alteration of the encoding procedure can rectify this and lead to perfect late time teleportation. This alteration is explained by the HPR protocol, and we derive it by reexamining the equivalence between the HPR and TW protocols in the case of fermionic qubits. Here, the relevant difference between bosons and fermions is that the fermionic SWAP gate is *not* related to the Grover search operation $1 - 2P_{\text{FEPR}}$ by single-qubit rotations. Since fermions gain a minus sign upon exchange, the fermionic SWAP gate takes the form

$$\text{SWAP}_F = \begin{pmatrix} 1 & 0 & 0 & 0 \\ 0 & 0 & 1 & 0 \\ 0 & 1 & 0 & 0 \\ 0 & 0 & 0 & -1 \end{pmatrix} = \frac{i\psi_{1,l}\psi_{2,l} + i\psi_{1,r}\psi_{2,r} + i\psi_{1,l}\psi_{2,r} - i\psi_{2,l}\psi_{1,r}}{2}. \tag{F5}$$

This is a *two-qubit* controlled-phase (CZ) gate away from $1 - 2P_{\text{FEPR}}$:

$$1 - 2P_{\text{FEPR}} = \begin{pmatrix} 1 & 0 & 0 & 0 \\ 0 & 0 & i & 0 \\ 0 & -i & 0 & 0 \\ 0 & 0 & 0 & 1 \end{pmatrix} = \frac{1 - i\psi_{1,l}\psi_{1,r} - i\psi_{2,l}\psi_{2,r} - (i\psi_{1,l}\psi_{1,r})(i\psi_{2,l}\psi_{2,r})}{2} = \text{SWAP}_F \cdot \text{CZ}, \tag{F6}$$

where the CZ gate is defined as

$$\begin{aligned} \text{CZ} &= \begin{pmatrix} 1 & 0 & 0 & 0 \\ 0 & i & 0 & 0 \\ 0 & 0 & -i & 0 \\ 0 & 0 & 0 & -1 \end{pmatrix} = (1+i)\frac{\psi_{1,l}\psi_{2,l} + i\psi_{1,r}\psi_{2,r}}{2} \\ &= \exp\Big(i\frac{\pi}{4}\Big) \cdot \exp\Big(-i\frac{\pi}{2}[i\psi_{1,l}\psi_{2,l}]\Big) \cdot \exp\Big(i\frac{\pi}{4}[i\psi_{1,l}\psi_{2,l}][i\psi_{1,r}\psi_{2,r}]\Big). \end{aligned} \tag{F7}$$

The single-fermion $\exp\big(-i\frac{\pi}{2}[i\psi_{1,l}\psi_{2,l}]\big)$ gate occurs on the swapped-out fermion and may be neglected. Inserting this

in place of the second Grover search operation gives the appropriate teleportation protocol:

$F_{\mathrm{EPR}} =$ 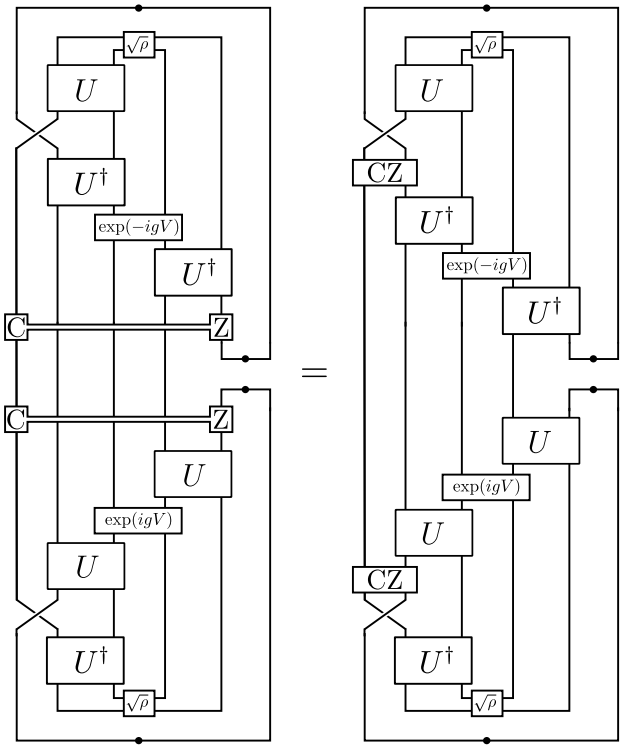 (F8)

In the second diagram we have slid the action of each side of the CZ gate such that the gate acts at the same time and on the same qubits as the initial SWAP gate.

We can relate the fidelity of teleportation to operator correlators by decomposing the encoding gate as

$$\mathrm{CZ}\cdot\mathrm{SWAP}_F = \frac{1}{2}\sum_{j=1}^{4} S_{j,l}^{L} S_{j,r}^{R} \tag{F9}$$

where we define the operators:

j	S_j^L	S_j^R	$S_j^R S_j^L$
1	$\mathbb{1}$	$\mathbb{1}$	$\mathbb{1}$
2	$i\psi_1\psi_2$	$i\psi_1\psi_2$	$\mathbb{1}$
3	$i\psi_1$	ψ_1	$i\mathbb{1}$
4	$i\psi_2$	ψ_2	$i\mathbb{1}$

according to Eq. (F6). The final column displays the product $S_j^L S_j^R$, where both act on the same qubit, which will

be useful shortly. We find a fidelity:

$F_{\text{EPR}} =$ 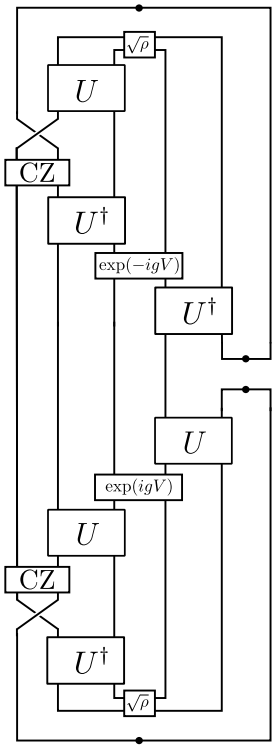 $= \frac{1}{2^2}\sum_{j,k}$ 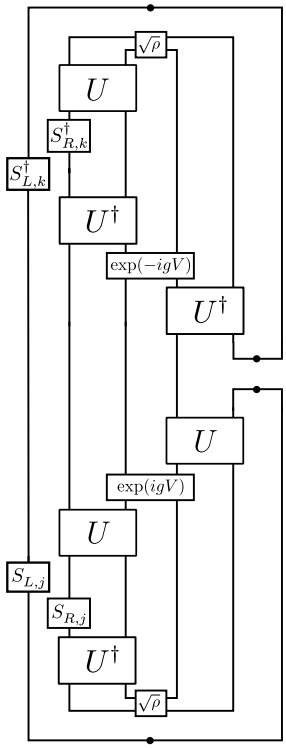 $= \frac{1}{2^4}\sum_{j,k}$ 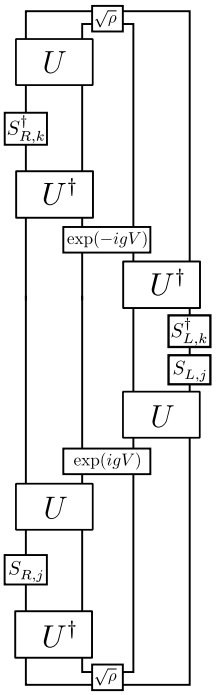 (F10)

In the peaked-size regime with correlator phases $\theta_{R,j}$, we have

$$\begin{aligned} F_{\text{EPR}} &= \frac{1}{2^4}\sum_{j,k} \langle \text{TFD}|\, S_{R,j,l}(t)\, e^{-igV}\, [S_{L,j,r} S^\dagger_{L,k,r}](-t')\, e^{igV}\, S^\dagger_{R,k,l}(t)\, |\text{TFD}\rangle \\ &= \frac{1}{2^4}\sum_{j,k} \exp(-i[\theta_{R,j}-\theta_{R,k}])\, \text{tr}\Big(S_{R,j}(t-t')\,\rho^{1/2}\, S_{L,j}(0)\, S^\dagger_{L,k}(0)\,\rho^{1/2}\, S^\dagger_{R,k}(t-t')\Big) \end{aligned} \tag{F11}$$

At infinite temperature, late times, and $g\langle V\rangle = \pi$, we have correlator phases $\theta_{R,j} = 0$ for the identity and two-bosonic operator and $\theta_{R,j} = \pi/2$ for single-body fermionic operators, and find perfect teleportation fidelity:

$$\begin{aligned} F_{\text{EPR}} &= \frac{1}{2^4}\sum_{j,k} \exp(-i[\theta_{R,j}-\theta_{R,k}])\, \text{tr}\Big(S_{R,j}\, S_{L,j}\, S^\dagger_{L,k}\, S^\dagger_{R,k}\Big) \\ &= \frac{1}{2^4}\sum_{j,k} \exp(-i[\theta_{R,j}-\theta_{R,k}]) \cdot i^{F_j} \cdot (-i)^{F_k} \cdot \text{tr}(i\psi_1\psi_2\, i\psi_1\psi_2) \\ &= \frac{1}{2^4}\sum_{j,k} \exp(-i[\theta_{R,j}-\theta_{R,k}]) \cdot i^{F_j} \cdot (-i)^{F_k} \\ &= \frac{1}{2^4}\sum_{j,k} (-i)^{F_j} \cdot i^{F_k} \cdot i^{F_j} \cdot (-i)^{F_k} \\ &= 1, \end{aligned} \tag{F12}$$

where we define $F_j = 1$ if $S_{L/R,j}$ is fermionic, and 0 if bosonic.

We note that for state, as opposed to EPR, teleportation, the above CZ gate turns out not to be necessary. Since coherent superpositions of different fermion parity cannot be created by physical Hamiltonians, which are bilinear in fermionic operators, we should only consider teleporting states of definite fermion parity. The CZ gate applies only an overall phase on these states, and so does not affect the success of teleportation.

We can also briefly analyze the low temperature results of Ref. [16] through the lens of operator correlator phases. Here, state teleportation is found to succeed perfectly at low temperatures only when the initial operators are encoded in p-body Majoranas, with $p = q/2+1$, despite the operator correlators having maximal magnitude for any value of p. At the semiclassical gravity teleportation time, the correlators have phases:

$\mathbb{1}$	1
ψ_1	$i^p(i)^{2p/q}$
ψ_2	$i^p(i)^{2p/q}$
$i\psi_1\psi_2$	$(-1)^p(i)^{4p/q}$

For single-body Majoranas, $p = 1$, the correlators clearly do not have the same phase—in fact, their phases are nearly identical to their phases at infinite temperature with no coupling—so state teleportation is not possible. When $p = q/2 + 1$, in the large-q limit, these phases are $1, \pm 1, \pm 1, 1$, respectively, where the sign is determined by whether $p = 1, 3 \bmod 4$. When the sign is odd, it can be corrected via the decoding operation $i\psi_1\psi_2 = (-1)^N$, which applies a minus sign when conjugating fermionic operators. Either case can therefore achieve perfect teleportation.

Appendix G: Teleportation and inelastic scattering at infinite temperature

In Section VII D, we found that strong stringy corrections to a bulk theory of gravity led to peaked-size teleportation as well as a deeply inelastic scattering amplitude. We will now demonstrate that these two phenomena—peaked-size teleportation and inelastic scattering—also coincide at infinite temperature, for arbitrary functional forms of the wavefunctions and scattering amplitudes. As we argued before, for a UV complete theory of quantum gravity, strong stringy (and in general deep inelastic) effects are expected to dominate only at high temperatures, $\beta \to 0$.

At infinite temperature, the form of the correlator is constrained by the equality

$$C_\psi(t; g)^* = -C_\psi(t; -g). \tag{G1}$$

This implies that $C_\psi(t)$ can be written as a real function of ig multiplied by the two-point function:

$$C_\psi(t) = \langle \psi_l \psi_r \rangle e^{-F(ig,t)}. \tag{G2}$$

When $g = 0$, $C_\psi(t)$ is equal to $\langle \psi_l \psi_r \rangle$, implying

$$F(ig) = igf_1(t) + O(g^2), \tag{G3}$$

where $f_1(t)$ is a real function. Therefore, at this order in g, the infinite temperature correlator is simply the two-point function multiplied by a pure phase, matching peaked-size teleportation [Eq. (29)].

To justify that higher order terms in g are subleading, we need an additional assumption: that the wavefunction of $\psi(t)$ has a saddle point at some momentum k. This is analogous to the boundary assumption that operator sizes are tightly peaked. At early times, this saddle will not be significantly changed by the coupling, since the derivative of the scattering matrix with respect to k will be suppressed by G_N, and at early times the time-dependence of the wavefunction will not be strong enough to compensate for this suppression (for example, in semiclassical AdS_2, we observed competition between $e^{2\pi t/\beta}$ and $1/G_N$). In such cases, it is easy to see that Eq. (84) becomes $\langle \psi_l \psi_r \rangle$ times a pure phase linear in g, with higher powers of g suppressed by G_N.

Infinite temperature also implies purely inelastic scattering, i.e. the scattering amplitude, $e^{i\delta} = 1 - S(k, s)$, is automatically real. To see this, we first rewrite the correlator in terms of the in-falling momentum operators, $\hat{P}$ and $\hat{K}$, for ψ_1 and $\psi(t)$ respectively. For instance, for the former we have:

$$\begin{aligned} \Psi_{1,r}(s, 0)\Psi^*_{1,l}(s, 0) &= \langle \psi_{1,l}(0)|s\rangle\langle s|\psi_{1,r}(0)\rangle \\ &= \int \frac{da}{2\pi} \langle \psi_{1,l}(0) e^{-ia\hat{P}} \psi_{1,r}(0)\rangle e^{ias}. \end{aligned} \tag{G4}$$

As $\psi(t)$ and ψ_1 are in principle independent operators, we have $[\hat{K}, \hat{P}] = 0$. Using this, we can rewrite Eq. (84) as

$$C_\psi(t) = \langle \psi_r(-t) \exp\left(-igS(\hat{K}, \hat{P}) i\psi_{1,l}\psi_{1,r}\right) \psi_l(t)\rangle. \tag{G5}$$

Taking the complex conjugate gives

$$\begin{aligned} C_\psi(t)^* &= \langle \psi_l(t) \exp\left(igS(\hat{K}, \hat{P})^*(-i)\psi_{1,r}\psi_{1,l}\right) \psi_r(-t)\rangle \\ &= -\langle \psi_r(-t) \exp\left(igS(\hat{K}, \hat{P})^* i\psi_{1,l}\psi_{1,r}\right) \psi_l(t)\rangle \end{aligned} \tag{G6}$$

where we used the fact that $\hat{K}$, $\hat{P}$ are Hermitian and that at infinite temperature $\psi_l(t)\,|\mathrm{TFD}\rangle = \psi_r(-t)\,|\mathrm{TFD}\rangle$. Combining this with Eq. (G1) then enforces $S(\hat{K}, \hat{P})^* = S(\hat{K}, \hat{P})$, i.e. purely inelastic scattering.